Single-ion addressing for the high-fidelity implementation of quantum network protocols

A master's thesis submitted to the
FACULTY OF
MATHEMATICS, COMPUTER SCIENCE AND PHYSICS,
OF THE LEOPOLD-FRANZENS UNIVERSITY OF INNSBRUCK,

in partial fulfillment
of the requirements for the degree of

MASTER OF SCIENCE
(MSC.)

carried out at the Institute of Experimental Physics
under the guidance of Rainer Blatt

presented by
MARKUS TELLER, BSC.

APRIL 2017

Kurzfassung

Um eine langreichweitige Kommunikation in einem zukünftigen Quantennetzwerk zu gewährleisten werden Netzwerkprotokolle benötigt, welche mit einer hohen Güte implementiert werden können. Ein Grundbaustein eines solchen Quantennetzwerkprotokolls ist ein sogenanntes Quantengatter. Diese werden im vorliegenden Experiment mittels Zustandsmanipulation von gefangenen Ionen realisiert. In dieser Masterarbeit wird ein Laserstrahl zur Einzeladressierung gefangener Ionen aufgebaut und charakterisiert. Ein besonderes Merkmal der neuen Einzeladdressierung ist ein elektro-optischer Deflektor. Dieser ermöglicht die Ablenkung des Laserstrahls abhängig von der am Deflektor anliegenden Spannung. Vor der Integration des elektro-optische Deflektors in den optischen Aufbau der neuen Einzeladdressierung, ist die Abhängigkeit des Austrittswinkels des Laserstrahls von der anliegenden Spannung und der Polarisation des einfallenden Lichtes zu untersuchen.

Nach Implementierung der neuen Einzeladdressierung im experimentellen Aufbau, wird mithilfe einer Methode zur Rekonstruktion der effektiven Phononenzahl und der Rabifrequenz der Radius des Strahls am Ion zu $w = 3.526(5)\,\mu\mathrm{m}$ bestimmt. Der nächste Schritt der Charakterisierung der Einzeladdressierung ist die Messung des Adressierungsfehlers in einem Ionenkristall. Aus dem Addressierungsfehler $\epsilon_{\mathrm{res}} = 6.80(6)\%$ in resonanter Konfiguration wird auf den Adressierungsfehler $\epsilon_{\mathrm{off}} = 0.462(3)\%$ in nicht-resonanter Konfiguration geschlossen. Ein Vergleich des Addressierungsfehlers in resonanter und nicht-resonanter Konfiguration, zeigt einen signifikant geringeren Fehler für den nicht-resonanten Fall. Daher ist es vorteilhaft den Laserstrahl in dieser Konfiguration zu verwenden.

Für ein zukünftiges Netzwerkprotokoll wird ein Quantengatter benötigt, welches uns ermöglicht gezielt den Zustand eines Ions in einem Ionenkristall zu invertieren. Dieses Quantengatter setzt sich aus Lichtpulsen eines globalen Laserstrahls, welcher alle Ionen simultan manipuliert, und Lichtpulsen der Einzeladdressierung zusammen. Die Erfolgswahrscheinlichkeit von $93(3)\%$ des Gatters durch Nutzen der neuen Einzeladressierungs, ist im Rahmen des Fehlers identisch mit der Erfolgswahrscheinlichkeit von $91(4)\%$ vorhergegangener Messungen. Die Implementierung eines neuen globalen Strahles erhöht schlussendlich die Erfolgswahrscheinlichkeit des Quantengatters auf $99(1)\%$.

Abstract

For future long-distance communication in a quantum network, a high-fidelity implementation of quantum network protocols will be necessary. The building blocks for all quantum network protocols are gate operations, which are realized in our experiments by coherent manipulation of the trapped ions' electronic states by laser pulses. For individual manipulation of the state of a single ion in a string, a single-ion addressing beam has been set up and characterized in the framework of this master's thesis. The beam is shifted from one ion to another ion by means of an electro-optical deflector, and the dependence of the deflector on the applied voltage and polarization of the incident light is investigated. In order to characterize the beam profile of the addressing beam at the ions' position, a method is developed which enables the reconstruction of the effective phonon number and the Rabi frequency from a measurement of Rabi oscillations. Implementing this method, we measure the waist of the addressing beam and find it to be $w = 3.526(5)\,\mu\mathrm{m}$. In addition, the addressing error for a neighboring ion in a two-ion crystal is measured in resonant configuration and found to be $\epsilon_{\mathrm{res}} = 6.80(6)\%$, corresponding to the off-resonant addressing error $\epsilon_{\mathrm{off}} = 0.462(3)\%$. A composite qubit flip is implemented with this addressing beam, and the success probability of $93(3)\%$ is within the error bar identical with the previous value of $91(4)\%$. In order to improve the performance of the composite qubit flip, a new global beam has been implemented which simultaneously manipulates all ions in the string, and the success probability of the composite qubit flip is found to be $99(1)\%$. To conclude this thesis, an outlook is presented which addresses the next steps involving this addressing beam towards quantum network protocols.

Contents

1 Introduction **1**

2 Theoretical framework **4**
2.1 Atom light interaction 4
2.1.1 Light-matter interaction of a trapped ion 4
2.1.2 Doppler cooling 9
2.1.3 Sideband cooling 10
2.2 Optical repumping, Doppler cooling, and sideband cooling of the $^{40}Ca^{+}$ ion . . 12

3 Experimental setup **16**
3.1 Characteristics of the ion trap 16
3.2 Laser systems 20
3.2.1 Photo-ionization laser 20
3.2.2 Laser for fluorescence detection and Doppler cooling 21
3.2.3 The 854 nm and 866 nm laser systems 21
3.2.4 The 729 nm laser for qubit manipulation 21
3.3 Optical path of the 729 nm light 22
3.3.1 Setup of the intensity stabilization 22
3.3.2 Setup of the north-east and north-west global beams 23
3.3.3 Optical path of the addressing beam and the detection system 25
3.4 Detection systems 27
3.4.1 PMT Detection 28
3.4.2 CCD camera detection 30
3.5 Magnetic field stabilization 31
3.5.1 Principle of the magnetic field stabilization 32
3.5.2 Measurement of the coherence time 32
3.6 Conclusion 36

4 Characterization of the electro-optical deflector **37**
4.1 Principle of the electro-optical deflector 37
4.2 Setup for characterizing the electro-optical deflector 38
4.3 Results 39
4.3.1 Dependence on the polarization of the incident light 39
4.3.2 Dependence of the deflection angle on the applied voltage 41

4.3.3 Conclusion 42

5 Preparation of the ion **43**
5.1 Procedure for quantifying the ion temperature 44
5.2 Application of the effective phonon number reconstruction 45
5.3 Conclusion 48

6 Characterization of the single-ion addressing beam **49**
6.1 Beam profile of the addressing beam 49
6.2 Characterization of the cross-talk 53
6.3 Comparison between the results of the PMT and CCD camera detection 56
6.4 Comparison of the new and the old addressing beams 58
6.5 Conclusion 60

7 Implementation of the z gate **61**
7.1 Principle of the z gate 61
7.2 Performance with the symmetric circular global beam 64
7.3 Performance with the new global beam 65
7.4 Comparison with previous results 68
7.5 Conclusion 70

8 Summary and outlook **71**

A Python codes for the characterization of the EOD **73**
A.1 Python code for the analysis of the polarization dependency 73
A.2 Python code for the analysis of the deflection angle vs. voltage 74

B State preparation of the ion **77**
B.1 Python code for the analysis of the effective phonon number 77

C Characterization of the single ion addressing beam **78**
C.1 Python code for the calibration of the camera 78
C.2 Python code for the cross-talk measurement and the PMT-Camera comparison . 79

Bibliography **81**

Chapter 1

Introduction

Over the past years, quantum technology based on the manipulation of quantum states of single particles has been emerging from fundamental science in research institutions into a state of the art commercial technology. A prime example of the progress of quantum technology was seen in 2007 in a regional election in Switzerland, in which quantum cryptography was used for the first time to securely encode and transmit information about the outcome of the election [1]. Another highlight of quantum technology is the ongoing development of a fault-tolerant quantum computer, a device that promises to outperform a classical computer for certain tasks, such as factorization of large numbers [2]. A requirement for a physical implementation of a quantum computer is the ability to encode information, for example, in physical quantum bits (qubits) [3]. Such a physical quantum bit (qubit) can be formed, for example, by a long lived atomic state of a trapped ion [4] or the polarization of a photon [5]. Besides trapped ions and photonic systems, there are many more promising candidates for the physical realization of a quantum computer, such as superconducting circuits [6], in which the qubit is encoded in an artificial atom.

It is usual in our daily life not only to process information but also to send and receive information, and so the step from quantum computers to networks based on quantum technology is natural. In a future quantum network, quantum information will be exchanged as "flying qubits" over a large distance between network nodes. The network nodes will be realized by quantum memories, which will receive and encode the quantum information into a stationary qubit [3, 7]. However, the distribution of quantum information still represents a major challenge because it is necessary to preserve the quantum properties of the flying qubit while it travels from one node to another. For example, when photons are used as flying qubits and the nodes are connected with optical fibers, the losses of these fibers destroy the quantum information and consequently limit the communication length. One can overcome this limitation by using additional stationary qubits as quantum repeaters between the network nodes for purifying or correcting the received quantum information [8, 9]. Besides their function as quantum memories, the nodes can also be used as distant cores for distributed quantum computation.

One possible physical implementation of network nodes is trapped ions coupled to optical cavities [10]. In such a node, the stationary qubit is formed by ground or metastable atomic states of a trapped ion, and the quantum information is transported via optical photons between the nodes. These trapped ions are placed in the anti-node of a standing wave, which is provided by the two opposing, highly reflective mirrors of the optical cavity. The coupling between the ions and the cavity field enables not only a conversion between stationary and flying qubits but

also an efficient means of collection for the converted photons, as all photons will be emitted into the same cavity mode. After a certain time determined by the cavity properties, the photons will leak out of the optical cavity and can be sent via optical fibers to other network nodes.

In recent years, our research group has been able to implement the first steps towards such a quantum network, based on trapped ions coupled to cavities. In the first network node at the University of Innsbruck, ^{40}Ca ions are trapped inside a linear Paul trap and coupled to a high finesse Fabry-Pérot cavity. This ion-cavity interface was used to demonstrate a mapping of the ion's state onto the emitted photon [11]. Moreover, the ion's state was entangled with the polarization of a photon, which was emitted into the optical cavity [12]. As the next demonstrated quantum network protocol, two ions were coupled to the optical resonator and simultaneously entangled with photons. A measurement of the polarization of the two emitted photons resulted in the ions being entangled with one another for a certain combination of polarizations [13]. Since it is only necessary to examine the polarization of the photons in order to confirm entanglement between the ions, this probabilistic entangling operation was heralded by the detection of the photons. (In contrast, a non-heralded probabilistic entangling protocol would require us to measure the state of the ions in order to probe for entanglement between them, in which case the entanglement would not be available as a resource afterwards.) The presented approach does not require that the ions are in the same cavity. Thus, this probabilistic protocol is suitable for entangling two distant ions in different traps, which will be investigated in the future, as there are already two more quantum network nodes in development at the University of Innsbruck.

Currently, further improvements of quantum network nodes are the focus of ongoing research. One significant improvement would be to decrease losses of photons due to the losses in the optical fibers between the network nodes. A reduction of the fiber losses can be accomplished by converting the wavelength of the emitted photons to a telecommunication wavelength, at which these losses are minimal [14]. Such a conversion would use doped waveguides and is in development at one of the two additional network nodes. Another important improvement for a quantum network node is elongation of the time frame in which it is possible to successfully store and read out the quantum information. In the case of trapped ^{40}Ca ions, this memory time is limited by fluctuations of the magnetic field, which destroy the coherence of the stored quantum state. It is possible to avoid the influence of magnetic field fluctuations on the ion's state by encoding the logical qubit state onto two physical qubits [9, 15]. In this so-called decoherence-free subspace, the magnetic field fluctuations change the overall phase of the quantum state but preserve the coherence of the quantum information.

The next step at the first Innsbruck network node, at which this master's thesis research was carried out, is the implementation of a network protocol that allows temporal routing of photons which are entangled with individual ions of an ion string. In this protocol, two ions are coupled to the high-finesse cavity and are each sequentially entangled with a photon. In contrast to the previously implemented heralded entanglement, it should be possible to choose which ion is entangled first and which one is entangled afterwards. Thus, to prevent simultaneous entanglement of both ions with photons, it is necessary to transfer one ion into a state in which it cannot be entangled with a photon. In order to achieve this composite qubit flip, it is essential to manipulate only one ion in the ion crystal. (After loading several ions into the trap and cooling them, the ions are arranging in crystalline structure due to the competing effects of the trap potential and the coloumb force between them). This individual ion manipulation requires a laser beam with a beam size smaller than the distance between the two trapped ions. Such

an "addressing" beam was already implemented by Diana Habicher during her diploma thesis research [16] and is a standard tool for quantum computation with trapped ions [17]. However, the previous addressing beam was, due to the large beam size, limiting the success probability for a composite qubit flip because it not only affected the addressed ion but also manipulated the unaddressed one. The goal of this master's thesis research was therefore to set up a tightly focused addressing beam and to test its performance by implementing the composite qubit flip.

So far this chapter has been focused on motivating the work presented in this master's thesis. The next paragraphs highlight the main concepts and results I am going to present in the different chapters. First of all, the second chapter summarizes the fundamental atom-light interaction of a trapped ion. Furthermore, details on the implementation of optical repumping, Doppler cooling and sideband cooling of the ^{40}Ca ions used in our experiments are given. The third chapter discusses the experimental setup that is used for trapping ions as well as the laser systems used to manipulate the state of the ion. The next section describes the detection methods used to identify the ions' state. The working principle of the magnetic field stabilization is explained, and a measurement of the coherence time is presented.

One major upgrade to the experimental setup during my master's thesis work has been an electro-optical deflector that allows fast switching of the addressing beam between different ions. Therefore, Chapter 4 covers a characterization of the deflector. The dependence of the deflection angle on both the input polarization and the applied voltage is characterized.

Proper cooling of the ion is important, as different motional states of the ion are coupled differently to a laser beam. Imperfect cooling leads to a large thermal distribution of the phonon number, and consequently, it is impossible to transfer the ion from one state to another with a high success probability, since the Rabi frequency is different for each phonon number. To address this, a method based on Ref. [18] has been implemented which allows us to extract the effective phonon number and the Rabi frequency. A description of this method as well as an implementation with Doppler and sideband cooled ions can be found in Chapter 5.

Chapter 6 contains the key results of this master's thesis, namely, the characterization of the addressing beam. The beam profile is analyzed by using the tool developed in Chapter 5 to extract the Rabi frequency for different ion positions with respect to the beam. Furthermore, the cross-talk of the addressing beam is measured by loading two ions in the trap and measuring the individual excitation of each ion while only one is addressed. This chapter concludes with a comparison with previous results obtained with an earlier version of the addressing setup. In Chapter 7, the addressing beam is used to implement the composite qubit flip, which transfers the state of only one ion in a two-ion crystal from the ground to the excited state. At the end of this thesis, a new "global beam" for addressing all ions simultaneously was set up with elliptical beam shape, which improves the coupling of the global beam to the ions. Consequently, the composite qubit flip was remeasured and the results are compared to previous results from Ref. [19]. Chapter 8 summarizes this master's thesis and provides an outlook for the next steps towards the entanglement routing protocol.

Chapter 2

Theoretical framework

This chapter summarizes the theoretical concepts of the atom-light interaction which are necessary for understanding trapped ion experiments and, in particular, the measurements performed in this thesis research. Moreover, the techniques of Doppler cooling and sideband cooling are explained. The chapter concludes with a summary of the important properties of the ^{40}Ca ion and the implementation of cooling techniques with this particular ion. Further details additional to the summaries provided in this chapter can be found in Refs. [18, 20].

2.1 Atom light interaction

2.1.1 Light-matter interaction of a trapped ion

Before we proceed to the description of cooling of trapped ions, it is necessary to understand the interaction between light and matter. A simple model system to start with is an ion placed in free space which interacts with a light field. More specifically, the level structure of this particular ion is simply formed by two electronic levels, depicted in Fig. 2.1a. The energy difference between the ground state $|S\rangle$ and the excited state $|D\rangle$ of such a two-level system is $E = \hbar\omega$, where $\hbar$ denotes the reduced Planck constant. The labeling of the states is chosen to preserve consistency with the level structure of the ^{40}Ca ion, which will be explained in Sec. 2.2. A laser beam with frequency ω_{L} is detuned by $\Delta = \omega - \omega_{\mathrm{L}}$ from the transition and couples the ground state with the excited state [20]. The interaction can be described by the optical Bloch equations, and the probability to find the ion in the state $|D\rangle$ varies sinusoidally between zero and one, corresponding to the so-called Rabi oscillations [20].

However, this model system is not sufficient to understand the measurements carried out during this master's thesis research. In order to describe the light-matter interaction of a trapped ion, one needs to extend this model system by placing the particle in a harmonic trap, shown in Fig. 2.1b. The energy of the trapped particle due to the trapping potential and the kinetic energy is given by

$$\hat{H}_{\mathrm{tr}} = \frac{\hat{p}^2}{2m} + V(\hat{x}) \tag{2.1}$$

with the harmonic trapping potential described by

$$V(\hat{x}) = \frac{1}{2} m \omega_{\mathrm{t}}^2 \hat{x}^2. \tag{2.2}$$

Here m denotes the mass of the particle, $\hat{x}$ the particle position, $\hat{p}$ the momentum of the particle and ω_{t} the trap frequency. By using the relations

$$\hat{x} = \sqrt{\frac{\hbar}{2m\omega_m}}(\hat{a} + \hat{a}^\dagger) \tag{2.3}$$

$$\hat{p} = i\sqrt{\frac{m\omega_m\hbar}{2}}(\hat{a}^\dagger - \hat{a}) \tag{2.4}$$

between the position and momentum operators and the creation and annihilation operators of phononic excitation $\hat{a}^\dagger$ and $\hat{a}$, one can express Eq. 2.1 as

$$\hat{H}_{\mathrm{tr}} = \hbar\omega_m\left(n + \frac{1}{2}\right). \tag{2.5}$$

The energy of the motion is now quantized and the quanta of excitation are called phonons. The phonon number $n = \hat{a}^\dagger\hat{a}$ can be any non-negative integer number, and at the motional ground state of zero phonons there is a residual ground state energy of $E = \hbar\omega_m/2$.

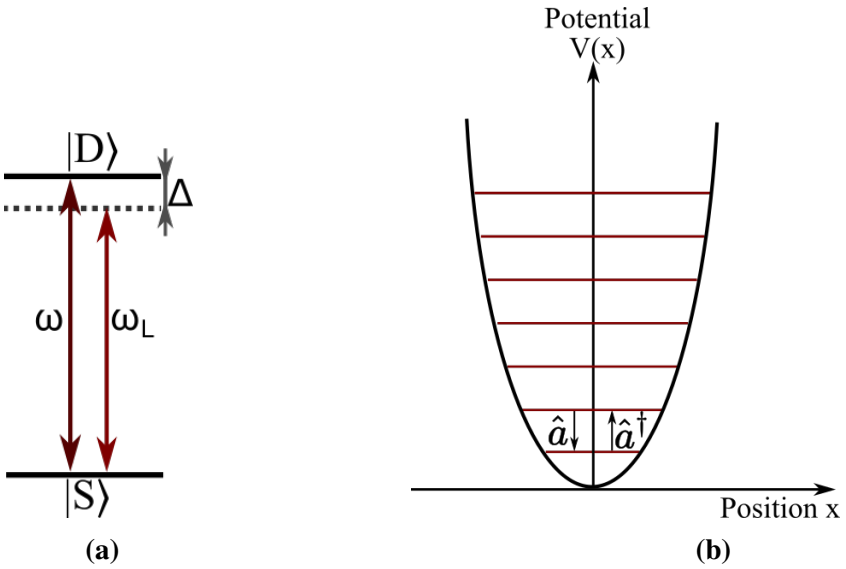

Figure 2.1: a) Two-level system. The energy difference between the ground state and the excited state is $E = \hbar\omega$. The frequency ω_L of a driving laser is detuned by Δ from the transition frequency. b) Potential of a harmonic trap. The horizontal lines indicate different phonon numbers. The the creation and annihilation operators $\hat{a}^\dagger$ and $\hat{a}$ enable transitions between different phononic states.

The total energy of the trapped two-level system consists now of two parts. The first part is the energy of the electronic states which are interacting with the light-field, and the second part is the energy of the harmonic oscillator described by Eq. 2.5 [18]. By introducing the Lamb-Dicke parameter

$$\eta = k\sqrt{\frac{\hbar}{2m\omega_{\mathrm{t}}}} := kx_0, \tag{2.6}$$

it is possible to compare the length scales of these two parts, since the Lamb-Dicke parameter connects x_0, the extent of the motional ground state wavepacket, with the wave number k of

the light field. In the so-called Lamb-Dicke regime in which the atomic wave-packet is much smaller than the wavelength of the laser light, the full system is described in the interaction picture by [18]

$$H_{\mathrm{I}} = \frac{\hbar\Omega}{2}\left((1 + i\eta(\hat{a} + \hat{a}^{\dagger}))\hat{\sigma}^{+}\mathrm{e}^{-i\Delta t} + (1 - i\eta(\hat{a} + \hat{a}^{\dagger}))\hat{\sigma}^{-}\mathrm{e}^{i\Delta t}\right). \tag{2.7}$$

In order to derive this time-dependent Hamiltonian, which holds as long as $\eta^2(2n+1) \ll 1$ is fulfilled, the rotating wave approximation and the Taylor expansion

$$\mathrm{e}^{i\eta(\hat{a}+\hat{a}^{\dagger})} \approx 1 + i\eta(\hat{a} + \hat{a}^{\dagger}) + \mathcal{O}(\eta^2) \tag{2.8}$$

have been used. A detailed derivation of Eq 2.7 can be found in Chapter 3.1 of Ref. [18]. Here the Pauli spin matrices $\hat{\sigma}^{+}$ and $\hat{\sigma}^{-}$ raise and lower the atomic state, and the coupling strength between the ion and the laser field is determined by Ω, the coupling constant.

It is important to emphasize that the products occurring in Eq. 2.7 of the creation and annihilation operators and the Pauli spin matrices couple the atomic and phononic state. Therefore, the Hamiltonian acts on a Hilbert space which is spanned by the electronic and the motional states, and thus, a state vector of the system is a product state $|i, n\rangle = |i\rangle \otimes |n\rangle$, where $|i\rangle$ denotes the atomic and $|n\rangle$ the phononic state.

By applying the time-dependent Schrödinger equation

$$i\hbar\frac{\partial}{\partial t}\psi = H_{\mathrm{I}}\psi, \tag{2.9}$$

one can derive the evolution of the different states of this system. The time evolution of a state $|\psi(t)\rangle = c_n(t)|S, n\rangle + d_n(t)|D, n\rangle$ for resonant driving of the carrier transition, which requires a detuning of $\Delta = 0$, leads to a set of coupled equations [20]

$$\dot{c}_n = -i\frac{\Omega_{n,n}}{2}d_n \tag{2.10}$$

$$\dot{d}_n = -i\frac{\Omega_{n,n}}{2}c_n \tag{2.11}$$

with the characteristic frequency [18]

$$\Omega_{n,n} = \Omega(1 - \eta^2 n), \tag{2.12}$$

called the Rabi frequency. In contrast to Eq. 2.7, which is based on a Taylor expansion on the first order around the Lamb-Dicke parameter, Eq. 2.12 takes also the second order of the expansion into account [18]. Therefore, the solution to Eq. 2.11 is

$$\begin{pmatrix} c_n(t) \\ d_n(t) \end{pmatrix} = \begin{pmatrix} \cos(\Omega_{n,n}t/2) & -i\sin(\Omega_{n,n}t/2) \\ -i\sin(\Omega_{n,n}t/2) & \cos(\Omega_{n,n}t/2) \end{pmatrix} \begin{pmatrix} c_n(0) \\ d_n(0) \end{pmatrix}, \tag{2.13}$$

which leads to the the time evolution

$$\begin{aligned} |\psi(t)\rangle = &\cos(\Omega_{n,n}t/2) - i\sin(\Omega_{n,n}t/2))c_n(0)|S, n\rangle \\ &+ \cos(\Omega_{n,n}t/2) - i\sin(\Omega_{n,n}t/2))c_n(0)|D, n\rangle \end{aligned} \tag{2.14}$$

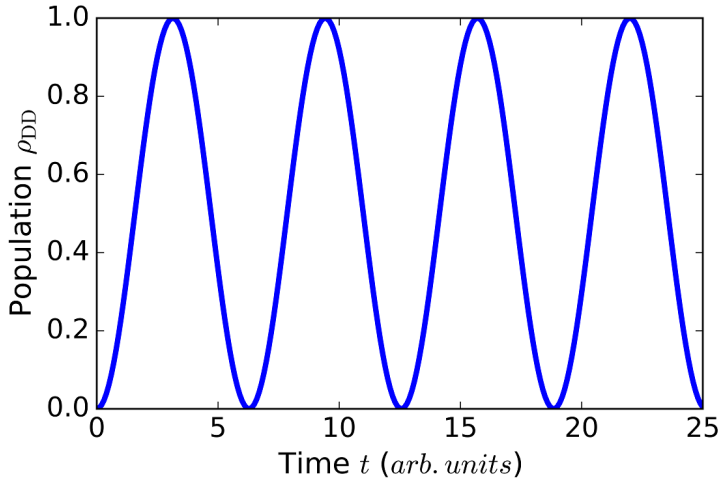

Figure 2.2: Evolution of the population of the excited state over time of a single driven two-level ion according to Eq. 2.15. After a time $t_{\pi/2} = \pi/2\Omega_{n,n}$, the ion is in the superposition state $\frac{1}{\sqrt{2}}(|S\rangle + |D\rangle)$, and after a time $t_\pi = \pi/\Omega_{n,n}$, the ion is fully excited.

of the state $|\psi(t)\rangle$. Consequently, if the ion starts in $|S\rangle$, the probability of measuring the state $|D\rangle$ is given by

$$\rho_{\mathrm{DD}} = |\langle D|\psi\rangle|^2 = \frac{1}{2}(1 - \cos(\Omega_{n,n}t)). \tag{2.15}$$

An illustration of the probability of measuring the excited state as a function of time is shown in Fig. 2.2. After an excitation time $t_{\pi/2} = \pi/2\Omega_{n,n}$, the ion is in the superposition state $\frac{1}{\sqrt{2}}(|S,n\rangle + |D,n\rangle)$. A laser pulse with length $t_{\pi/2}$ is called a $\pi/2$ pulse. The population of $|D,n\rangle$ reaches its maximum after a π pulse with length $t_\pi = \pi/\Omega_{n,n}$. It is important to emphasize that the oscillation in Fig. 2.2 corresponds to the situation in which only one phonon number is occupied. In a general experimental situation, the phonon numbers are distributed according to a thermal distribution, which will cause damping of the Rabi oscillations.

As a consequence of the coupling in Eq. 2.7 between the motional and the electronic states of the ion, transitions $|i,n\rangle \rightarrow |f,n+m\rangle$ from the initial atomic state $|i\rangle$ to the final state $|f\rangle$ in which the phonon number is changed by m are also possible [18]. To first order in the Lamb-Dicke regime, as in Eq. 2.7, we can restrict ourselves to transitions $m = \pm 1, 0$, and a schematic of these transitions is shown in Fig. 2.3. The laser frequency for resonant driving of these sideband transitions is given by

$$\omega_{\mathrm{L}} = \omega \pm \omega_{\mathrm{t}}. \tag{2.16}$$

The frequency $\omega + \omega_{\mathrm{t}}$ corresponds to the so-called blue sideband transitions, in which the motional state is increased by 1 phonon. In contrast, the frequency $\omega - \omega_{\mathrm{t}}$ corresponds to the so-called red sideband transitions, in which the phonon number decreases by 1. The Rabi frequencies for the red and blue sidebands

$$\Omega_{n-1,n} = \eta\sqrt{n}\Omega \tag{2.17}$$

$$\Omega_{n+1,n} = \eta\sqrt{n+1}\Omega \tag{2.18}$$

are weaker than the Rabi frequency of the carrier transition [18]. One important application of these sideband transitions is sub-Doppler cooling via sideband cooling [21]. Moreover, the shared motional degree of freedom of an ion string is widely used to carry out interactions between the ions and enables, for example, entanglement of the atomic states with one another [22, 23].

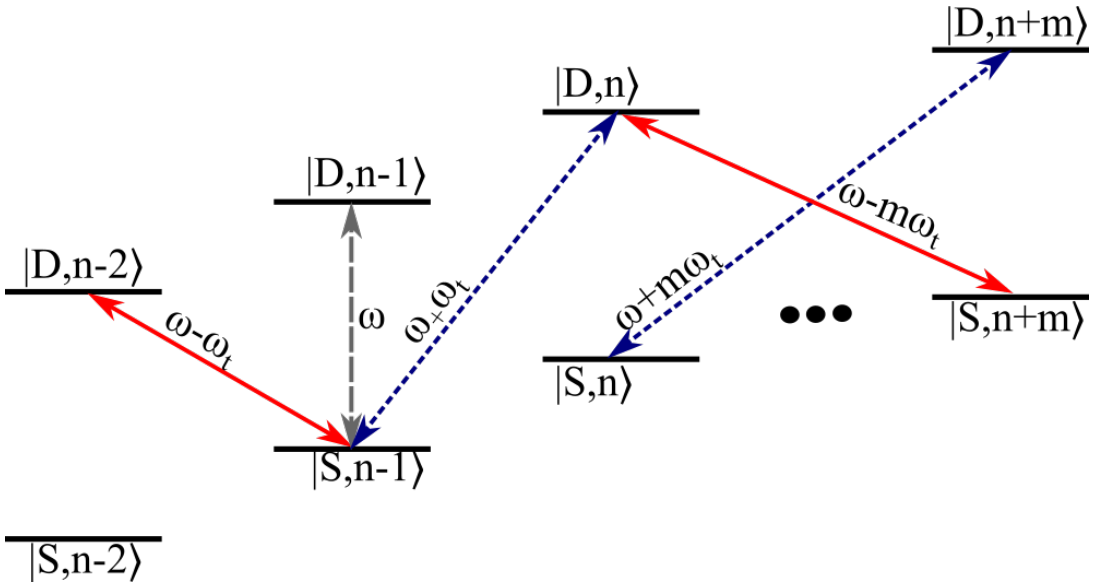

Figure 2.3: Schematic of the possible transitions. Here n corresponds to the motional state of the trapped ion, and $|S\rangle$ and $|D\rangle$ are the ground and excited state of the two-level system. In the Lamb-Dicke regime, only transitions for which $m = \pm 1, 0$ are possible.

2.1.2 Doppler cooling

Before we are able to address sideband transitions as in Fig. 2.3, we must first fulfill the condition $\eta^2(2n+1) \ll 1$. Thus, the phonon number needs to be reduced, which we achieve by performing Doppler cooling. An atom with velocity v and mass m is moving along the x-direction and can be cooled by using the momentum of photons with frequency ω_L impinging in $-x$-direction. In the one-dimensional case, the motion of the atom shifts the laser frequency seen by the atom by an amount kv due to the Doppler effect. Note that the laser frequency ω_L is chosen to be detuned by $\Delta = \omega_\mathrm{L} - \omega$ from the atomic transition frequency ω. Here, k denotes the wave number of the driving field. A positive velocity v indicates a motion of the atom towards the laser beam, whereas a negative velocity describes a motion away from the laser beam. In the case of a two-level system, the total amount of light scattered by the atom is given by [20]

$$R_\mathrm{scatt} = \Gamma \frac{\Omega^2}{\Gamma^2 + 4(\Delta - kv)^2}. \tag{2.19}$$

The scattering rate combined with the photon momentum $p = \hbar k$ leads to the scattering force

$$F = \hbar k \Gamma R_\mathrm{scatt}, \tag{2.20}$$

which is illustrated as a function of the detuning in Fig. 2.4a. Each absorption event induces a momentum transfer from the photon to the atom, and if the initial momentum of the atom is higher than the momentum of a single photon, the momentum kick cools the motion along the x-direction. On the contrary, if the atom is moving in $-x$-direction away from the laser, the motion in this direction is enhanced by the absorption event.

As shown in Sec. 2.1.1, a trapped ion exhibits a periodic motion inside the ion trap. For a negative detuning, the ion more likely absorbs a photon while moving towards the laser beam than while moving away from the laser, and therefore, the absorption events are cooling on average the motion of the ion. In contrast to the cooling provided by negative detuning, a positive detuning leads to heating, and as a consequence of the Doppler shift, hot ions are shifted out of resonance with the laser transitions and are not be able to absorb light efficiently. After a certain lifetime $\tau = 1/\Gamma$ of the excited state, the ion emits a photon in an arbitrary direction. This emission process also induces a momentum kick on the ion. Since the absorption and emission processes are repeated for many times, the mean velocity induced by the momentum kicks of the spontaneous emission events is on average zero.

Nevertheless, the spontaneous emission induces heating due to the non-zero mean squared velocity [20]. The cooling rate due to the momentum exchange has to be compared to the heating rate induced by spontaneous emission, and in the steady state condition, the temperature can be expressed for a negative detuning Δ as [18]

$$T = -\frac{\hbar\Gamma}{4k_\mathrm{B}}\left(\frac{\Gamma}{2\Delta} + \frac{2\Delta}{\Gamma}\right), \tag{2.21}$$

shown in Fig. 2.4b, with the minimum achievable temperature

$$T_\mathrm{D} = \frac{\hbar\Gamma}{2k_\mathrm{B}} \tag{2.22}$$

at a detuning $\Delta = -\Gamma/2$. By using the relation $k_\mathrm{B}T/2 = \hbar\omega_\mathrm{t}(n + 1/2)$, one can express the Doppler limit in terms of the minimum achievable phonon number

$$n_\mathrm{D} = \frac{k_\mathrm{B}T_\mathrm{D}}{2\hbar\omega_\mathrm{t}} - \frac{1}{2} = \frac{\Gamma}{4\omega_\mathrm{t}} - \frac{1}{2}. \tag{2.23}$$

For a detailed derivation of the Doppler limit, see Chapter 3.2 of Ref. [18] and Chapter 9 of Ref. [20].

In contrast to the optical molasses technique used to cool neutral atoms, where two counter propagating laser beams are used to cool the motion along one dimension and are compensating the radiation pressure induced by the light fields, only one cooling beam is needed for cooling a trapped ion as the trap confining force balances the radiation pressure induced by the light. It is necessary that this cooling beam have a wave vector with an overlap with all three trapping axes [20]. However, since the condition $\Gamma \gg \omega_\mathrm{t}$ holds in the measurements described in this master's thesis, it is impossible to cool the ion directly into its ground state with Doppler cooling.

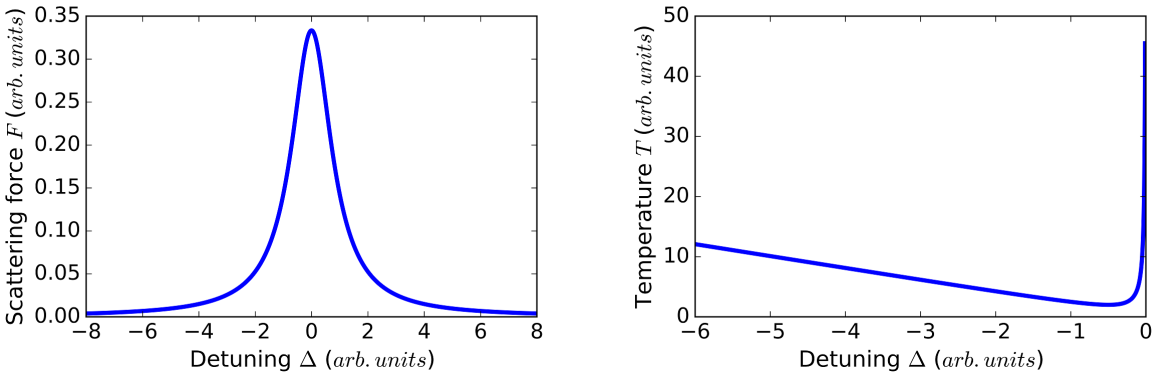

(a) **(b)**

Figure 2.4: a) Scattering force F according to Eq. 2.20 as a function of the detuning Δ. All parameters are set to 1. b) Temperature T after Doppler cooling according to Eq. 2.21 as a function of the detuning Δ. The natural linewidth is chosen to be $\Gamma = 1$. The lowest temperature T_D is achieved at a detuning of $\Delta = -\Gamma/2$.

2.1.3 Sideband cooling

For reaching temperatures below the Doppler limit, an effective cooling technique is sideband cooling. As already described in Sec. 2.1.1, it is possible to address individual transitions between electronic states that change the phononic state. As long as the condition

$$\delta\omega_\mathrm{L} \ll \Gamma \ll \omega_\mathrm{t}, \tag{2.24}$$

is fulfilled, one operates in the so-called resolved sideband regime [24]. Here $\delta\omega_\mathrm{L}$ denotes the laser linewidth, Γ the natural linewidth of the carrier transition and ω_t the trapping frequency. Once the ion has been cooled by Doppler cooling into the Lamb-Dicke regime, one can perform

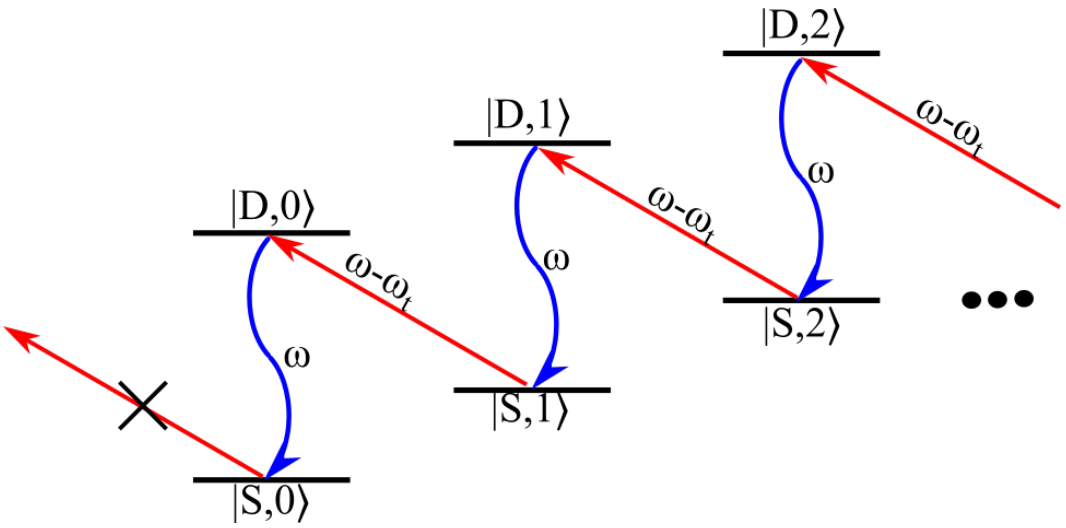

Figure 2.5: Schematic of the sideband cooling procedure. Here ω_t is the trapping frequency. The states $|S\rangle$ and $|D\rangle$ are the ground and excited state of the two-level system and ω is the transition frequency between them. By applying a π pulse on the red sideband, we excite the ion, and thus, one phonon is annihilated. Afterwards, the ion decays back into the atomic ground state by emitting a photon at the carrier transition frequency. Once the ion reaches the motional ground state, it can no longer absorb light on the red sideband.

sideband cooling (Fig. 2.5) by applying a sequence of π pulses with frequency $\omega - \omega_\mathrm{t}$ on the red sideband transition. After each π pulse, the ion decays back to the atomic ground state by emitting a photon with frequency ω into carrier transition. Once it reaches the motional ground state, the ion can no longer absorb light on the red sideband. A detailed description and a rigorous mathematical derivation can be found in Ref. [25]. Finally, one can extract the temperature of a motional mode by performing spectroscopy of the sideband. Based on measurements of the excitation probabilities ρ_R and ρ_B of the red and blue sidebands, one can calculate the population of the motional ground state [18]

$$p_0 = 1 - \frac{p_\mathrm{R}}{p_\mathrm{B}}. \tag{2.25}$$

In the case of a three-dimensional trap, one usually has to cool all three sidebands sequencially to reach a high occupation probability close to one of the motional ground state of all modes, because of coupling between the motional modes [18]. The procedure gets more and more complicated and time-consuming for longer ion strings, as longer ion strings have more different vibrational modes. For example, for a two-ion crystal, cooling of six different modes is necessary. For even longer ion crystals other cooling techniques are preferable, for example, cooling using electro-magnetic induced transparency, which enables cooling of all motional modes at the same time [26].

2.2 Optical repumping, Doppler cooling, and sideband cooling of the $^{40}Ca^{+}$ ion

The physical quantum bit used in our experiments is formed by the $|4S_{1/2}\rangle \leftrightarrow |3D_{5/2}\rangle$ quadrupole transition of the $^{40}Ca^{+}$ ion. The meta-stable state $|3D_{5/2}\rangle$ is an optimal candidate for a qubit state, because of the long lifetime of $\tau \approx 1.17\,\mathrm{s}$. The $|4S_{1/2}\rangle \leftrightarrow |3D_{5/2}\rangle$ qubit transition can be driven by laser light at $729\,\mathrm{nm}$, a wavelength at which high laser powers can be obtained by a titanium sapphire laser. An advantage of the $^{40}Ca^{+}$ ion for quantum network experiments is that most of the atomic transitions are in the red- and near-infrared regime, for which it is easier to produce highly reflective mirror coatings and high-coupling efficiency fibers with which light can be transmitted over long distances. The level scheme of the ion without an external magnetic field is drawn in Fig. 2.6.

After coherent manipulation of the qubit in an experiment, state detection is performed via the $|4S_{1/2}\rangle \leftrightarrow |4P_{1/2}\rangle$ transition in order to measure the population of $|4S_{1/2}\rangle$ and the population of $|3D_{5/2}\rangle$. By addressing the ion with $397\,\mathrm{nm}$ light, it is possible to measure fluorescence of the ion, which can be detected either with a camera or a photo-multiplier tube, whenever the ion is in $|4S_{1/2}\rangle$. In contrast, if the ion is in the excited state $|3D_{5/2}\rangle$, it cannot be excited on the $|4S_{1/2}\rangle \leftrightarrow |4P_{1/2}\rangle$ transition, and therefore, the ion is not fluorescing. More information on state detection can be found in Sec. 3.4.

Not only state detection is performed via the $|4S_{1/2}\rangle \leftrightarrow |4P_{1/2}\rangle$ transition, but also Doppler cooling is achieved via this dipole transition. The population of $|4P_{1/2}\rangle$ decays with a rate of $\Gamma_{\mathrm{P1/2-S1/2}} = 2\pi \cdot 20\,\mathrm{MHz}$ into the ground state and with a rate of $\Gamma_{\mathrm{P1/2-D3/2}} = 2\pi \cdot 1.67\,\mathrm{MHz}$ into $|3D_{3/2}\rangle$ [27]. For a trapping frequency of $\omega_z = 1\,\mathrm{MHz}$, the Doppler limit for this transition according to Eq. 2.23, expressed as a phonon number, is $n_D = 10$. Because of the probability of $p_{\mathrm{D3/2}} = 6\%$ that the ion decays during state detection or Doppler cooling from $|4P_{1/2}\rangle$ to $|3D_{3/2}\rangle$, it is necessary to illuminate the ion with $866\,\mathrm{nm}$ light while exciting the $|4S_{1/2}\rangle \leftrightarrow |4P_{1/2}\rangle$ transition [28]. This repumping process brings the population from $|3D_{3/2}\rangle$ to $|4P_{1/2}\rangle$, where it can be accessed via the $397\,\mathrm{nm}$ light.

After performing state detection, we want to reinitialize the ion back in the ground state before starting any experiment. Since the lifetime of $|3D_{5/2}\rangle$ is $\tau \approx 1.17\,\mathrm{s}$, waiting for the occurrence of spontaneous decay, which would bring the ion back into the ground state, would be cumbersome. Therefore, $854\,\mathrm{nm}$ light excites the $|3D_{5/2}\rangle \leftrightarrow |4P_{3/2}\rangle$ transition, and the population of $|4P_{3/2}\rangle$ decays with a probability of $p_{\mathrm{P3/2}} = 94\%$ into $|4S_{1/2}\rangle$ via emission of a $393\,\mathrm{nm}$ photon.

The situation becomes more complex as soon as one includes a static magnetic field. Due to the Zeeman effect, the degeneracy of the sub-levels is lifted, and we can drive frequency-selective transitions between the sub-levels of $|4S_{1/2}\rangle$ and the sub-levels of $|3D_{5/2}\rangle$. A requirement on the laser used to drive these transitions is a narrow linewidth which is smaller than the frequency splitting between the sub-levels of $|3D_{5/2}\rangle$.

The qubit transition used in the framework of this thesis is the $|4S_{1/2}, m_J = -1/2\rangle \leftrightarrow |3D_{5/2}, m_J = -1/2\rangle$ transition. In principle, we could have also chosen the sub-level $|3D_{5/2}, m_J = +1/2\rangle$ as a qubit state, because this state has the same coupling strength to the magnetic field. The disadvantage of higher angular momentum states, for example, $|3D_{5/2}, m_J = \pm 3/2\rangle$ or $|3D_{5/2}, m_J = \pm 5/2\rangle$ as a qubit state is that the stronger coupling to the magnetic field

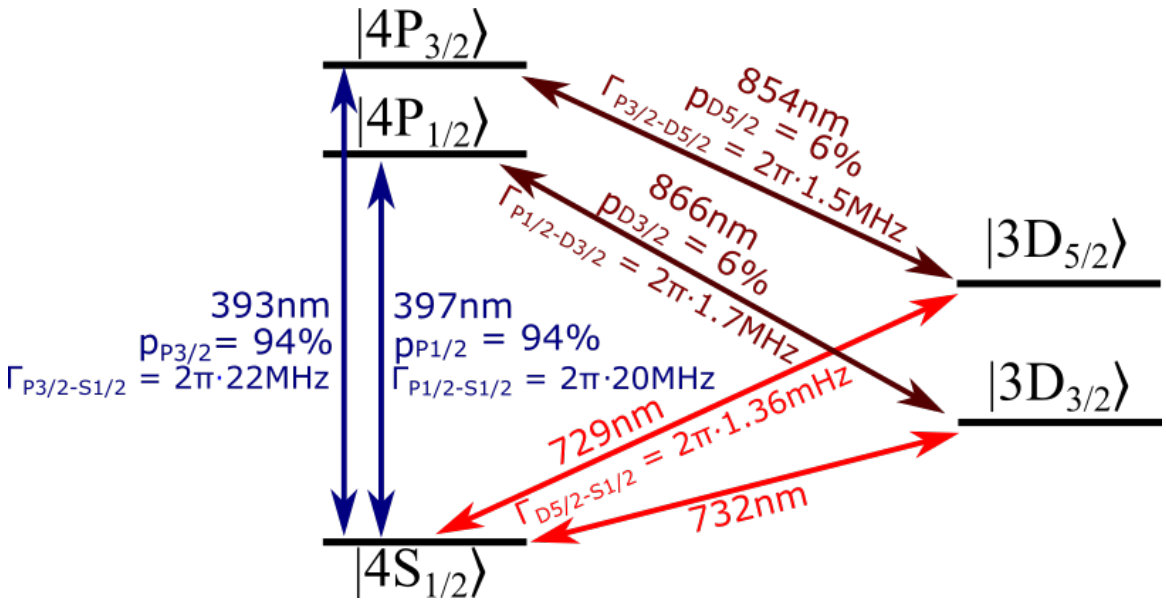

Figure 2.6: Transitions and decay probabilities of the relevant electronic states of the $^{40}Ca^{+}$ ion. The qubit transition is formed by the quadrupole transition from $|4S_{1/2}\rangle$ to $|3D_{5/2}\rangle$. Repumping from $|3D_{5/2}\rangle$ is implemented with $854\,\mathrm{nm}$ light. Doppler cooling and state detection of the $^{40}Ca^{+}$ ion is implemented via $|4P_{1/2}\rangle$. The excited state $|4P_{1/2}\rangle$ decays with probability of $p_{D3/2} = 6\%$ into $|3D_{3/2}\rangle$, therefore the population of $|3D_{3/2}\rangle$ is repumped with $866\,\mathrm{nm}$ light into $|4P_{1/2}\rangle$ during state detection or Doppler cooling. The decay rates and decay probabilities are taken from Refs. [27, 29, 30].

leads to a higher sensitivity on magnetic field fluctuations which limit the coherence time of the qubit state.

However, after Doppler cooling or state detection, the ion population is spread over the two angular momentum states of the manifold of $|4S_{1/2}\rangle$. Because the result of any qubit operation is depending of the initial qubit state, it is important to initialize the qubit always in the same ground state before starting any operation. Thus, the population of the sub-level $|4S_{1/2}, m_J = 1/2\rangle$ needs to be repumped into $|4S_{1/2}, m_J = -1/2\rangle$. This optical repumping procedure is illustrated in Fig. 2.7. By applying a π pulse on the $|4S_{1/2}, m_J = 1/2\rangle \leftrightarrow |3D_{5/2}, m_J = -3/2\rangle$ transition, the population is transferred into $|3D_{5/2}, m_J = -3/2\rangle$. Next, by illuminating the ion with $854\,\mathrm{nm}$ light, the population is transferred into $|4P_{3/2}, m_J = -3/2\rangle$ and $|4P_{3/2}, m_J = -1/2\rangle$. As a consequence of the selection rules for dipole transitions, $|4P_{3/2}, m_J = -3/2\rangle$ only decays to $|4S_{1/2}, m_J = -1/2\rangle$ [20]. On the contrary, the sub-level $|4P_{3/2}, m_J = -1/2\rangle$ decays according to the Clebsch-Gordan coefficients with a probability of approximately 66% into $|4S_{1/2}, m_J = -1/2\rangle$ and with a 33% chance into $|4S_{1/2}, m_J = 1/2\rangle$ [31]. Therefore, this repumping procedure is usually repeated for 20 cycles to ensure the ion is prepared in $|4S_{1/2}, m_J = -1/2\rangle$ with a probability close to one.

As mentioned in Sec. 2.1.1, a thermal distribution of phonon numbers leads to damping of Rabi oscillations and therefore limits the quality of the qubit operations. Thus, it is desirable to perform sideband cooling in addition to Doppler cooling. As explained in Sec. 2.1.3, sideband cooling requires a narrow-linewidth transition so that the sidebands can be resolved. Thus, the $|4S_{1/2}, m_J = -1/2\rangle \leftrightarrow |3D_{5/2}, m_J = -5/2\rangle$ transition is optimal for sideband cooling as its linewidth is $\Gamma_{D5/2} = 2\pi \cdot 1.36\,\mathrm{mHz}$. However, the drawback for sideband cooling with the

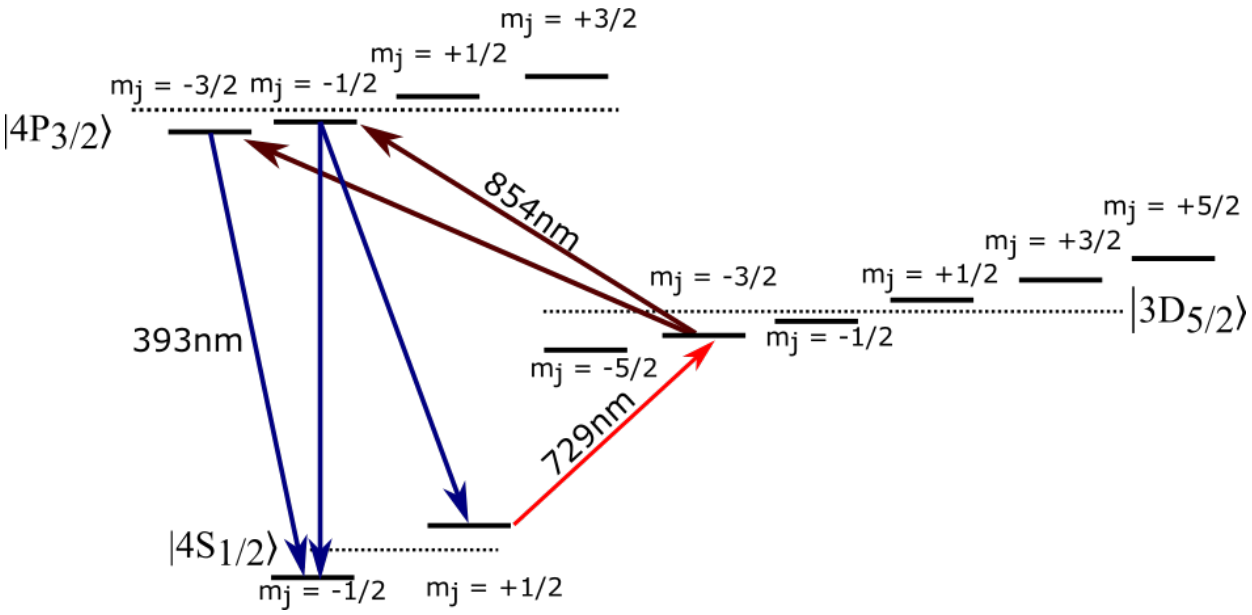

Figure 2.7: Transitions used for optical pumping. Due to the presence of a static magnetic field, the Zeeman effect lifts the degeneracy of the sub-levels. The dotted lines indicate the energy levels of the degenerate electronic states. Repumping of the population of $|4\mathrm{S}_{1/2}, m_J = 1/2\rangle$ is achieved by applying a π pulse on the $|4\mathrm{S}_{1/2}, m_J = 1/2\rangle \leftrightarrow |3\mathrm{D}_{5/2}, m_J = -3/2\rangle$ transition. Afterwards, $854\,\mathrm{nm}$ light excites the ion into $|4\mathrm{P}_{3/2}, m_J = -3/2\rangle$ and $|4\mathrm{P}_{3/2}, m_J = -1/2\rangle$. According to the selection rules for dipole transitions, the ion can only decay from $|4\mathrm{P}_{3/2}, m_J = -3/2\rangle$ into $|4\mathrm{S}_{1/2}, m_J = -1/2\rangle$. Nevertheless, the sub-level $|4\mathrm{P}_{3/2}, m_J = -1/2\rangle$ can decay with a 33% probability into $|4\mathrm{S}_{1/2}, m_J = 1/2\rangle$. Consequently, the repumping procedure has to be repeated multiple times.

meta-stable state is again the long lifetime because after a π pulse on the red sideband, one has to wait for spontaneous decay on the carrier transition. In order to accelerate the cooling process, an alternative scheme similar to the reinitialization of the qubit state after the state detection can be used, which is drawn in Fig. 2.8. By continuously repumping the population of $|3\mathrm{D}_{5/2}, m_J = -5/2\rangle$ into $|4\mathrm{P}_{3/2}\rangle$ with $854\,\mathrm{nm}$ light, the spontaneous decay of the manifold of $|4\mathrm{P}_{3/2}\rangle$ accelerates the sideband cooling procedure [18].

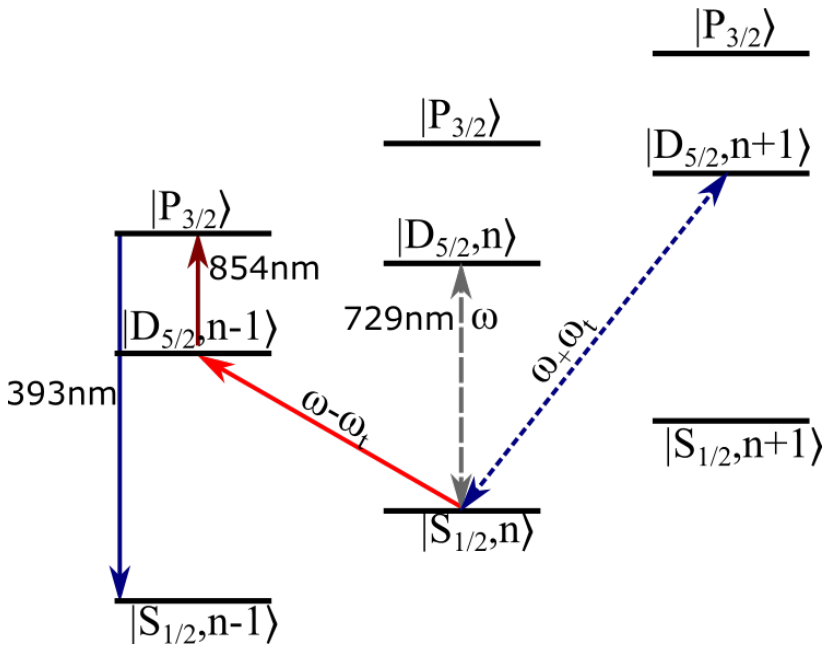

Figure 2.8: Schematic of sideband cooling of the $^{40}Ca^{+}$ ion. The sideband cooling procedure can be accelerated by taking advantage of the spontaneous decay of $|4P_{3/2}\rangle$ into the ground state. Therefore, one repumps after the π pulse on the red sideband with $854\,\mathrm{nm}$ light.

Chapter 3

Experimental setup

This chapter describes different parts of the experimental setup used in the framework of this master's thesis. First of all, the characteristics of the ion trap used to trap $^{40}\mathrm{Ca}$ ions are explained, based on the work reported in Refs. [27, 32], and the laser systems used to manipulate the ion are summarized. The next section describes the methods for detection of the ion's state using a photomultiplier and a CCD camera, based on Ref. [19]. Subsequently, the optical paths of the global $729\,\mathrm{nm}$ beams are summarized, and the performance of the intensity stabilization is characterized. Finally, this chapter concludes with a description of the magnetic field stabilization, which ensures stable transitions from the ground state to the higher-lying angular momentum states.

3.1 Characteristics of the ion trap

The basis of an ion trap is the Coloumb force, which acts as the restoring force on a charged particle and pushes an ion towards the center of the trap. However, due to Earnshaw's theorem, it is not possible to trap a particle stably solely with a static electric field. One can use a time-varying electrical quadrupole field to build a Paul trap [33], or a static electric and a static magnetic field to build a Penning trap [34]. In a linear Paul trap the position-dependent potential [32]

$$\phi(x,y,z,t) = \underbrace{\frac{V\cos(\Omega t)+U_\mathrm{r}}{2}\left(1+\frac{x^2-y^2}{r_0^2}\right)}_{:=\phi_\mathrm{r}} + \underbrace{\kappa U_0\left(z^2-\frac{1}{2}(x^2+y^2)\right)}_{:=\phi_\mathrm{s}} \tag{3.1}$$

for a particle with mass m and charge e varies at the trap frequency Ω over the time t. Here x,y and z denote the position of the charged particle, r_0 is the characteristic radial length and κ is a geometrical factor. The time-varying radial potential ϕ_r is created by a radio-frequency field with an amplitude V and a DC component U_r, and it traps the particle in the radial direction. The confinement along the axial direction is provided by a static potential ϕ_0 with an amplitude

U_0. Hence, close to the center of the trap, the force F acting on the particle is described by

$$F_x(x,t) = -\frac{xe}{r_0^2}(V\cos(\Omega t) + U_\mathrm{r}) + \kappa e U_0 x \tag{3.2}$$

$$F_y(y,t) = +\frac{ye}{r_0^2}(V\cos(\Omega t) + U_\mathrm{r}) + \kappa e U_0 y \tag{3.3}$$

$$F_z(z,t) = -2\kappa e U_0 z. \tag{3.4}$$

One can simplify the equations of motion for the x direction and y direction by substituting t with $t = \tau/2\Omega$, and thus the equations of motion are

$$\frac{d^2x}{d\tau^2} = -\frac{4xe}{m\Omega^2 r_0^2}(V\cos(2\tau) + U_\mathrm{r}) + \frac{4\kappa e U_0 x}{m\Omega^2} \tag{3.5}$$

$$\frac{d^2y}{d\tau^2} = +\frac{4ye}{m\Omega^2 r_0^2}(V\cos(2\tau) + U_\mathrm{r}) + \frac{4\kappa e U_0 y}{m\Omega^2} \tag{3.6}$$

$$. \tag{3.7}$$

One can see that these equations have the form of the so-called Mathieu equations, and one can express them as [33]

$$\frac{d^2x}{d\tau^2} = (a_x + 2q_x\cos(2\tau))x \tag{3.8}$$

$$\frac{d^2y}{d\tau^2} = (a_y + 2q_y\cos(2\tau))y. \tag{3.9}$$

The parameters

$$a_x = \frac{4e}{m\Omega^2}\left(-\frac{U_\mathrm{r}}{r_0^2} + \kappa U_0\right)$$

$$a_y = \frac{4e}{m\Omega^2}\left(\frac{U_\mathrm{r}}{r_0^2} + \kappa U_0\right)$$

and

$$q_x = -\frac{2eV}{mr_0^2\Omega^2}$$

$$q_y = -q_x$$

are known as the a and the q parameters [33]. For $a_i, q_i \ll 1$, where $i = x, y$, the approximate solution of the Mathieu equations (Eq. 3.8 and Eq. 3.9) takes the form of [18]

$$i(t) = (i_0 + i_\mathrm{A}\cdot\cos(\omega_i t))(1 + \frac{q_i}{2}\sin(\Omega t)). \tag{3.10}$$

The motion of the trapped particle is described by two parts: a slow motion at a the frequency ω_i and a fast motion, called micromotion, which oscillates with the driving frequency Ω. Here i_A is the amplitude of the slow motion and i_0 corresponds to a displacement from the potential minimum at $x = y = z = 0$. The trapping frequency along the axis i is calculated to be [18]

$$\omega_i = \sqrt{a_i + \frac{q_i^2}{2}}\frac{\Omega}{2}. \quad (i = x, y) \tag{3.11}$$

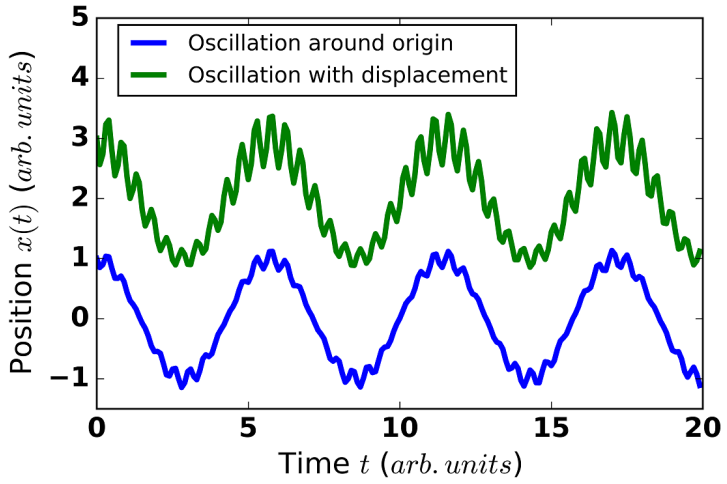

Figure 3.1: Illustration of the movement of a trapped particle according to Eq. 3.10 for arbitrarily chosen parameters. The blue curve is the movement of the particle around the potential minimum, and the green curve represents the same movement around a position $x_0 = 2$ displaced from the potential minimum. The micromotion of the particle is visible as the fast oscillations which are imprinted on the slow motion. One can see that the micromotion grows for larger displacements from the origin. The trapping frequency is chosen to be $\omega_x = 1.1$, the driving frequency is set to be $\Omega = 50$ and the amplitude is $x_\mathrm{A} = 1$.

As one can see in Fig. 3.1, the micromotion grows for larger displacements from the trap center. The blue curve illustrates the optimal situation, where the particle oscillates around the potential minimum. The green curve shows a common experimental situation, in which stray fields cause a displacement x_0 of the average position from the potential minimum. In this situation, the micromotion is larger than in the ideal situation of the blue curve.

The force along the axial direction according to Eq. 3.4 is similiar to the classical harmonic oscillator, and the solution of the equation of motion is a harmonic motion described by [32]

$$z(t) = z_\mathrm{A} \cos(\omega_\mathrm{z} t). \tag{3.12}$$

where z_A denotes the amplitude of the motion, and the axial trapping frequency is calculated to be

$$\omega_\mathrm{z} = \sqrt{\frac{2\kappa e U_0}{m}}. \tag{3.13}$$

The linear ion trap used in our experimental setup is pictured in Figs. 3.2a and 3.2b. The radially symmetric quadrupole field (Eq. 3.1) is generated by four electrodes. A radio-frequency voltage with a driving frequency $\Omega \approx 2\pi \cdot 23\,\mathrm{MHz}$ is applied on two opposing electrodes, while the other two electrodes are grounded. The axial confinement is achieved by applying a DC voltage $V = 770\,\mathrm{V}$ on the two endcap electrodes. The micromotion of the ion can be compensated by applying DC voltages on the four compensation electrodes depicted in Fig. 3.2a. The axial frequency is in our case $\omega_z \approx 1\,\mathrm{MHz}$, and the radial frequencies are $\omega_r \approx 1.7\,\mathrm{MHz}$. Further details on this ion trap can be found in Ref. [35].

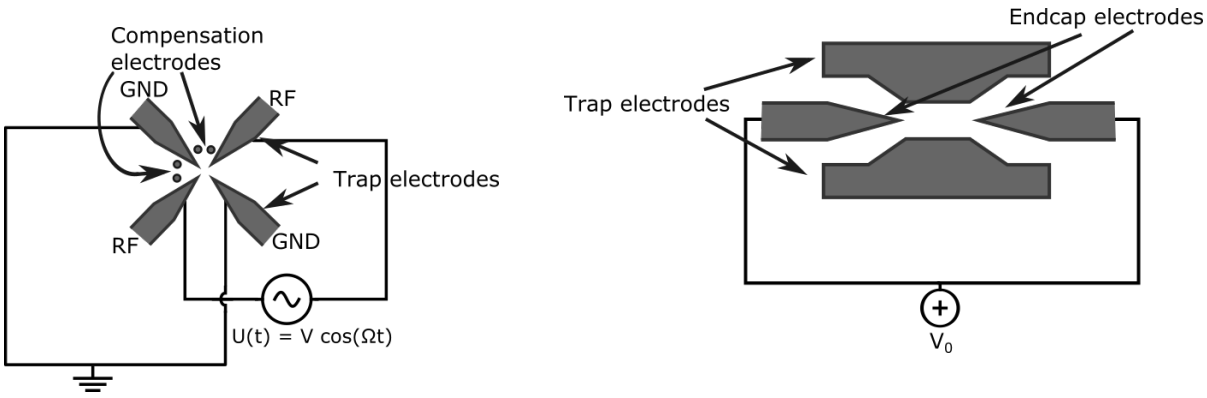

(a) **(b)**

Figure 3.2: a) Front view of the linear ion trap. One can see the compensation electrodes that are used for compensating the micromotion of the ion. The confinement along the radial direction is achieved by applying RF voltage to two opposing trap electrodes, while the other two electrodes are grounded. b) Side view of the linear ion trap. One can see the RF blades on the top and bottom. The endcap electrodes which confine the ions in the axial trap direction are placed on the side.

As shown in Fig. 3.3a, the trap is placed in the center of a high finesse optical cavity, which has a length of $2\,\mathrm{cm}$. The cavity is formed by two highly reflective mirrors and has been used for coherent state transfer from the ion to a photon [12]. The optical cavity is one of the key features of our experimental setup. However, since the resonator is not used in the framework of this master's thesis, a detailed description of the cavity is omitted in this work. More information about the cavity and the previous work carried out with the ion-cavity system can be found in Refs. [19, 35–37]. Fig. 3.3b shows the front view of the vacuum chamber, in which we reach ultra-high vacuum at a pressure around $10^{-11}\ \mathrm{mbar}$. Furthermore, a compass illustrates the notation originally defined in Ref. [35] and is used in this thesis to specify the directions of the laser beams. For example, the direction of the beam path indicated as an arrow in Fig. 3.3b is called north-east, because it originates from the north-east direction. Consequently, this beam is called the north-east beam. More details on the beam path are given in Sec. 3.3.2.

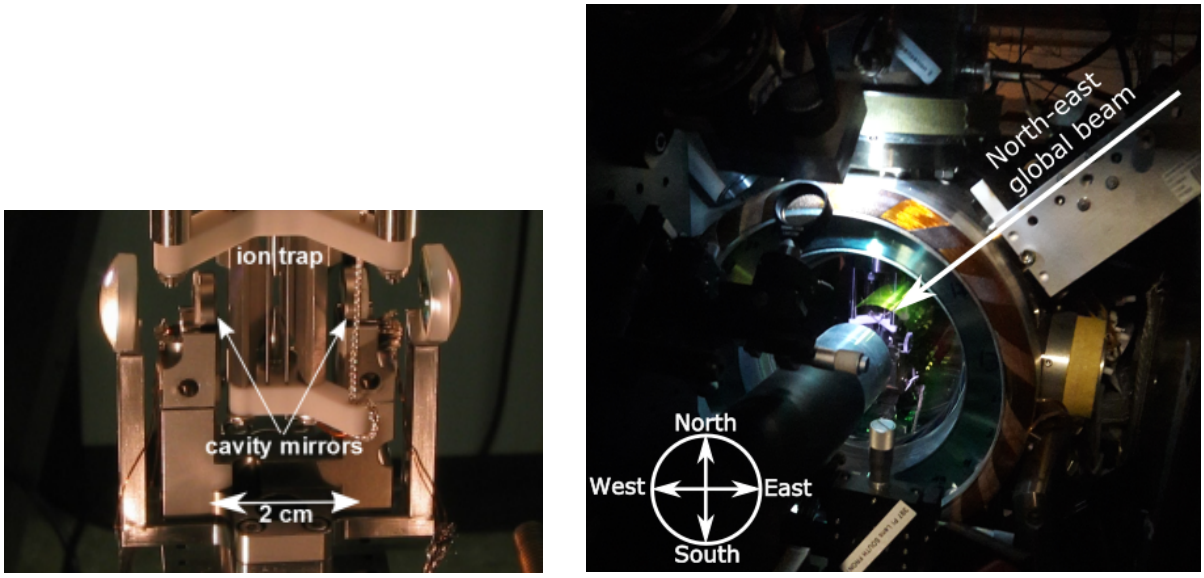

(a) **(b)**

Figure 3.3: a) Photograph of the linear ion trap placed inside the $2\,\mathrm{cm}$ long high finesse cavity. b) Photograph of the vacuum chamber in which the ion trap and the high finesse cavity are placed. The compass indicates the notation used to define the directions of the laser beams. The north-east global beam is indicated as an example of this notation as an arrow.

3.2 Laser systems

This section summarizes the laser systems used in the framework of this master's thesis to manipulate $^{40}Ca^{+}$ ions. Two additional lasers at wavelengths of $393\,\mathrm{nm}$ and $786\,\mathrm{nm}$ are used for experimental procedures which involve the experimental cavity. Since these lasers are not relevant for the measurements carried out in this thesis, an explanation here is omitted and can be found in Refs. [19, 36].

3.2.1 Photo-ionization laser

In order to load $^{40}Ca^{+}$ ions into the ion trap, an oven is heated by a current source, and neutral calcium atoms are emitted from the oven into the ion trap region. The calcium atoms are ionized via photo-ionization in a two-step process involving $422\,\mathrm{nm}$ and $375\,\mathrm{nm}$ laser light [38]. The light is provided by two DL-100 diode lasers from Toptica that are grating-stabilized in the Littrow configuration. While ions are loaded into the trap, the wavelength of the $422\,\mathrm{nm}$ laser is scanned on the order of $1\,\mathrm{pm}$ by applying a voltage to the piezo element that adjusts the position of the grating. A scan of the laser frequency ensures resonance of the laser with the atomic transition even if the Doppler effect due to the movement of the atoms induces a frequency shift. More details about the photo-ionization process and the laser sources can be found in Ref.[38].

3.2.2 Laser for fluorescence detection and Doppler cooling

The $397\,\mathrm{nm}$ laser light used for fluorescence detection (Sec. 3.4) and Doppler cooling (Sec. 2.1.2), is provided by a $532\,\mathrm{nm}$ diode-laser-pumped titanium-sapphire laser[1] [39]. The frequency of this laser is stabilized to a medium-finesse reference cavity via the Pound-Drever-Hall method [40]. The $600\,\mathrm{mW}$ output power of $794\,\mathrm{nm}$ light is converted by a lithium triborate crystal (LBO) to $397\,\mathrm{nm}$ with an output power of $100\,\mathrm{mW}$ [39]. Afterwards, the light is split equally among four different experimental setups in the laboratory and passes through an acousto-optical modulator (AOM) in a double pass configuration. This double pass configuration allows us to control the frequency and the power of the light sent to the experiment table. Further details on the setup can be found in Refs. [37, 39].

The optical path of the $397\,\mathrm{nm}$ light on the experiment table is illustrated in Fig. 3.4. After the light exits a fiber collimator, the polarization of the light is cleaned with a half-wave plate ($\lambda/2$-plate) and a polarizing beam splitter (PBS). The reflected light is detected with a photodiode and monitored on an oscilloscope. The transmitted light is split again by half-wave plate and a PBS. The transmitted part is shifted by $+80\,\mathrm{MHz}$ by an AOM that is driven by a stable $80\,\mathrm{MHz}$ reference. Before the beam enters the vacuum chamber, its polarization is adjusted by a half-wave plate, and it is focused by a lens. The reflected light of the second polarizing beam splitter is also shifted by $+80\,\mathrm{MHz}$ by an AOM. Afterwards, a telescope expands the beam, which is then focused by a lens into the trap. This additional telescope was inserted to cool the ions' radial motion more efficiently by providing more power at the ions' location. We use a $\lambda/2$-plate to adjust the polarization of the light between the last lens and the vacuum chamber. While cooling with both beams enables us to reach lower phonon numbers than cooling with one beam, state detection is performed only with the southern beam, in order to avoid interference between the two beams [19].

3.2.3 The 854 nm and 866 nm laser systems

The $854\,\mathrm{nm}$ and $866\,\mathrm{nm}$ laser systems are used for repumping from the $\mathrm{D}_{5/2}$ and $\mathrm{D}_{3/2}$ manifolds. Both lasers are diode lasers[2] which are stabilized to reference cavities via the Pound-Drever-Hall method [40]. Again, AOMs are used for varying the frequencies and the intensity of the light. Details about the laser system and the optical setup can be found in Ref. [41]. Both wavelengths are transferred via the same optical fiber to the experiment table. After the light exits the fiber collimator, it is focused by a lens into the trap onto the ions.

3.2.4 The 729 nm laser for qubit manipulation

The latest version of the $729\,\mathrm{nm}$ laser was just recently set up by another master's student, and hence this summary is based on Ref. [42]. The laser system[3] consists of a titanium sapphire crystal that is pumped by $15\,\mathrm{W}$ of $532\,\mathrm{nm}$ light of a diode-pumped solid-state laser[4]. The solid-state laser consists of a Nd:YAG crystal, which is pumped by $808\,\mathrm{nm}$ laser light from a diode

[1] Coherent 899 ring laser

[2] $854\,\mathrm{nm}$ laser is a DL-100 diode laser from Toptica, and the $866\,\mathrm{nm}$ is a DL-Pro diode laser with tapered amplifier also from Toptica.

[3] Msquared SolsTiS

[4] Sprout-G Lighthouse Photonics

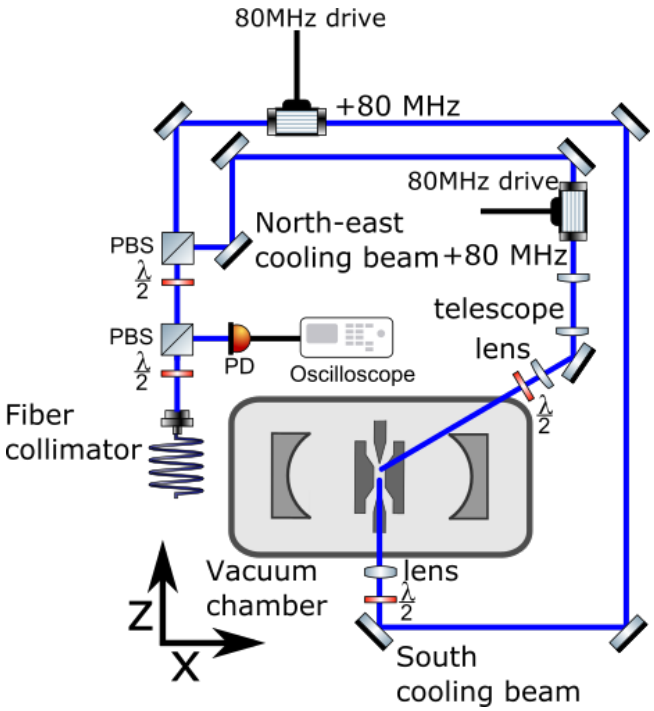

Figure 3.4: Simplified path of the 397 nm-light on the experiment table. Here PD abbrevates photodiode and PBS denotes a polarizing beam splitter. Details on the setup are explained in the text in Sec. 3.2.2.

laser. The 1064 nm light that is emitted by the solid-state laser is frequency-doubled via a LBO crystal to 532 nm [42]. The 729 nm laser is stabilized via the Pound-Drever-Hall method to an ultra-high finesse cavity [39]. The spectral linewidth of the laser is below 10 Hz, even on time scales up to 2000 s [42]. The whole laser system is enclosed in a wooden box with damping material on the walls, which provides acoustic shielding. The light is brought via an optical fiber with active length stabilization to the experiment table. This length stabilization limits the effects of frequency noise due to fluctuations of the fiber length [43]. Finally, 5 W of 729 nm light exits the optical fiber on the experiment table. This light is shared between the Linear Trap experiment[5] and our experimental setup. We use the light to seed a Tapered Amplifier[6](TA). From 20 mW of seed light, we typically have 200 mW available at the amplifier output.

3.3 Optical path of the 729 nm light

3.3.1 Setup of the intensity stabilization

During my master's thesis research, major upgrades of the optical path of the 729 nm light were performed. Thus, a detailed schematic of the new setup is given in Fig. 3.5.

[5] An experiment in Rainer Blatt's group that focuses on quantum computation with trapped ions.
[6] TA Boosta Pro from Toptica

The $729\,\mathrm{nm}$ light is sent from the Linear Trap experiment to a fiber collimator and is amplified by the TA up to $200\,\mathrm{mW}$. The light has a frequency shift of $80\,\mathrm{MHz}$ with respect to the frequency at the laser output. The polarization of the light is determined after the TA by a PBS and a half-wave plate.

The major upgrade performed is the new intensity stabilization after the amplifier. A voltage-controlled oscillator (VCO) provides an $80\,\mathrm{MHz}$ radio-frequency signal which is then amplified. An AOM modulates the light, and the zeroth diffraction order is used afterwards. The usage of the zeroth order ensures the frequency is not changed, and the AOM stabilizes the intensity by putting more or less power into the first order. A pick-off sends around $300\,\mu\mathrm{W}$ of light onto a photo-diode (PD), and the signal of the PD is sent into the input of an analog PID controller from Stanford Research Systems. The output of this module controls the amount of amplification of the high voltage amplifier.

Next, the intensity-stabilized light passes twice through an AOM, which shifts the light's frequency by $540\,\mathrm{MHz}$. This so called double-pass configuration allows the light to be switched on and off and enables frequency shifts without spatial deflection. The light then travels through another AOM, and the negative first order output of this AOM is coupled into an optical fiber, which is sent to the addressing beam path. Alternatively, a flip mirror allows us to sent this light instead to the north-east global beam path. An explanation for the labeling used to name the beam paths is given in Sec. 3.1. Moreover, the light of the zeroth order is sent into another AOM, and the minus first order output of this AOM is coupled into a fiber, which transports the light to the north-west global beam path.

Although the light that seeds the TA is already intensity-stabilized, the relative intensity fluctuation ΔI_{us} of the light after the TA without active stabilization is $\Delta I_{\mathrm{us}} = 3\%$. After active stabilization of the intensity, the intensity fluctuation is reduced to $\Delta I_{\mathrm{s}} = 1\%$. Active stabilization of the intensity is important because the maximum number of measurable Rabi osclliations N can be limited by intensity fluctuations. At this stability level assuming no other limitations, the number of oscillations is [18]

$$N < \frac{1}{\Delta I} = 100. \tag{3.14}$$

On the one hand, one has to keep in mind that the fluctuations of the intensity introduced after the stabilization are not included. On the other hand, it is shown in Ch. 5 that the damping of Rabi oscillations due to the ion motion is much stronger than intensity fluctuations, and consequently, motion is more of a limiting factor than intensity fluctuations.

3.3.2 Setup of the north-east and north-west global beams

A global beam allows us to manipulate the states of many ions a string simultaneously and equally. Two global $729\,\mathrm{nm}$ beams have been used for the master's thesis research: the old north-east global beam and the new north-west global beam. The setup of these two global $729\,\mathrm{nm}$ beams is illustrated in Fig. 3.6. Although we call one global beam old and the other global beam new, both are available for us at the same time, and we can choose which beam is used for manipulating the states of the ions.

First of all, after the light is brought to the north-east global beam path via an optical fiber, a fiber collimator sends the light with a Gaussian beam profile to a dichroic beam-splitter (BS)

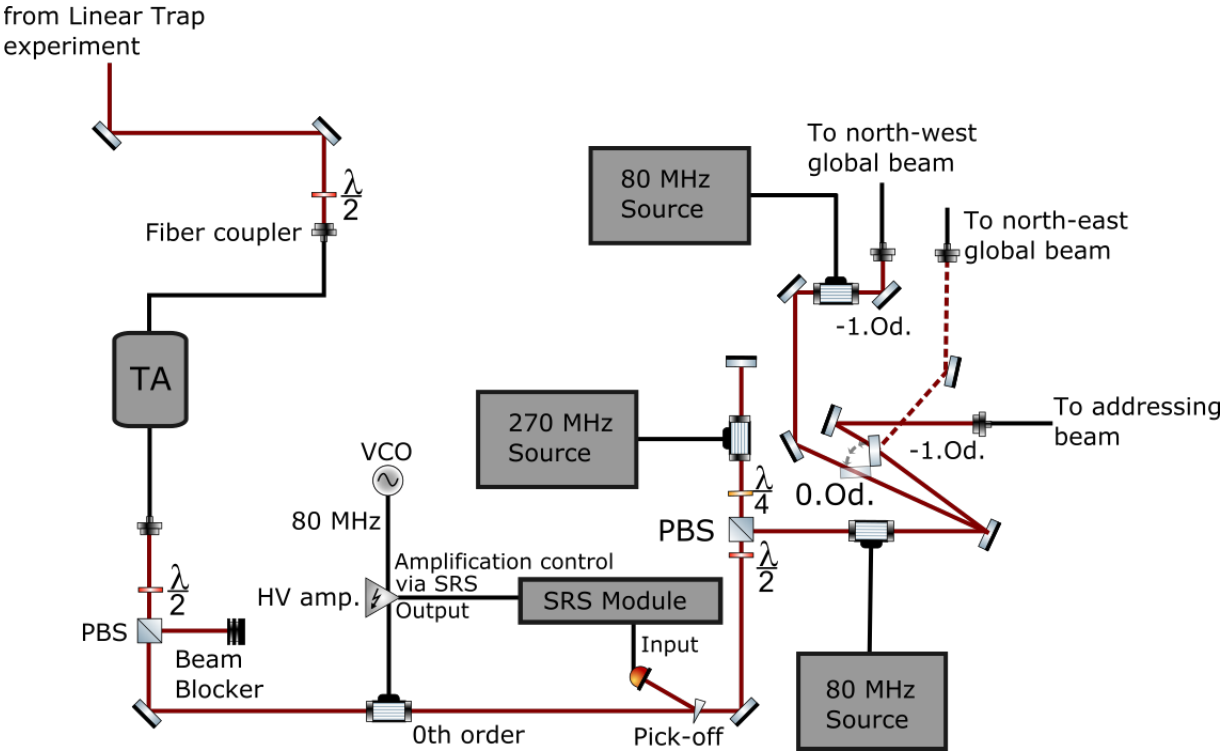

Figure 3.5: Optical path of the $729\,\mathrm{nm}$ light. Here VCO denotes voltage controlled oscillator, a PBS is a polarizing beam splitter and HV amp. abbrevates high-voltage amplifier. Details on the setup are explained in the text in Sec. 3.3.

which transmits $729\,\mathrm{nm}$ light and reflects $397\,\mathrm{nm}$ light. Afterwards, light of both wavelengths is focused by a lens onto the ion. The disadvantage of this global beam is the circular beam shape, which prohibits coupling more than two ions equally to the beam. Therefore, a new global beam has been set up, and a more detailed discussion about the motivation for implementing a new global beam can be found in Ch. 7.

The new north-west global beam replaces the previous addressing beam that was set up in a diploma project by Diana Habicher [16]. The north-west beam has been arranged by exchanging the fiber collimator. The new collimator contains a cylindrical lens that produces an elliptical beam profile with a waist-diameter of $1\,\mathrm{cm}$ along the z-axis and $0.33\,\mathrm{cm}$ along the y-axis. Here and in the following, waist-radius and waist-diameter are referring to the radius and diameter at which the intensity of the Gaussian beam is $1/e^2$ of the intensity located at the beam center [44]. Moreover, the ratio between the diameters of the two axes is approximately 3:1. The advantage of this beam shape is the equal distribution of the power along the axial direction over a wider range.

Afterwards, the light is focused by an objective with a numerical aperture of $NA \approx 0.11$ onto the ion. The whole system is placed on a motorized stage, which can be controlled with a precision of $0.0305\,\mu\mathrm{m}$ via a LabVIEW program. More details about the LabVIEW program and the motorized stage can be found in Ref. [16].

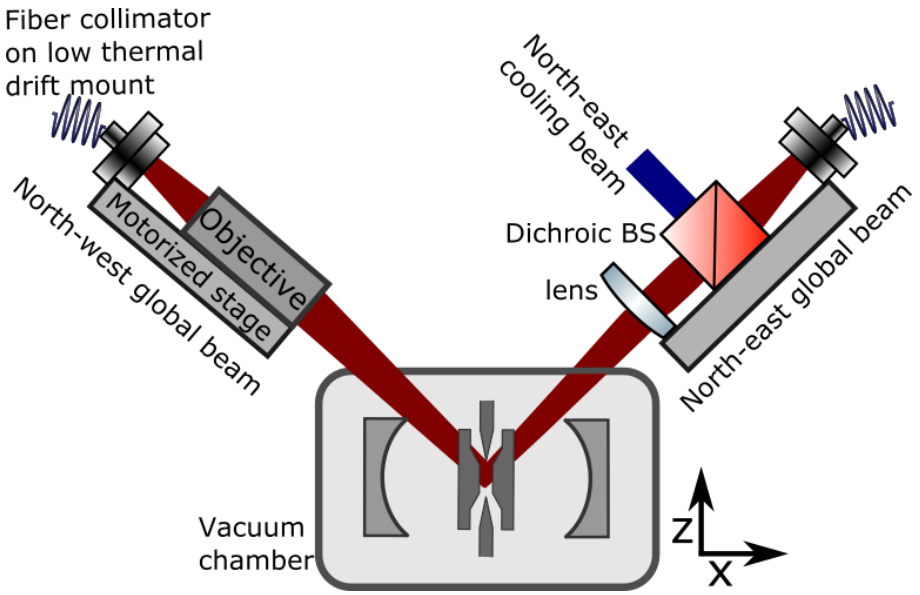

Figure 3.6: Schematic of the setup of the global 729 nm beams. The setup of the north-east global beam consists of a fiber collimator and a dichroic beam-splitter that reflects 397 nm light and transmits 729 nm light. The 397 nm cooling light and the 729 nm light are simultaneously focused by an lens onto the ion. The light of the north-west global beam is brought via an optical fiber to an collimator which is placed on a low-thermal-drift mount. A cylindrical lens in front of the collimator, which is not shown in the figure, produces an elliptical beam shape. Afterwards, the light is focused by an objective onto the ion string. The collimator and the objective are placed on a motorized stage that allows movement in three directions.

3.3.3 Optical path of the addressing beam and the detection system

Setting up the new addressing beam was the main goal of this master thesis. First of all, the new addressing beam replaces the old addressing system which was previously set up by Diana Habicher during her diploma thesis research. The main reason for a new addressing setup was the large beam size of the old addressing beam which restricted the application of the old addressing beam to experiments with two ions and limited the success probability of the composite qubit flip, a composite pulse sequence that is necessary for future quantum network protocols. Therefore, one goal for the new addressing beam was to achieve a beam size which is small enough to enable single-ion addressing of more than two ions. Another feature we wanted to implement, was an electro-optical deflector (EOD) which would enable us to shift the addressing beam from one ion to another.

A schematic of the new addressing setup and the optical path of the detection systems are given in Fig. 3.8. The ion is trapped in the linear Paul trap that is placed between the high finesse optical resonator, and its fluorescence light is detected by two different techniques. The first method is using a photo-multiplier tube (PMT) for detecting fluorescence which is focused onto the PMT by an objective with a magnification of 7. This objective is placed on a mono-dimensional stage, which enables translation in the y-direction. More details about the PMT detection path can be found in Ref. [36].

On the back side of the vacuum chamber, flourescence is collected by an objective with a

numerical aperture of $NA = 0.3$ and focused onto the chip of a CCD camera[7], which is placed approximately $1.5\,\mathrm{m}$ away from the vacuum chamber. This objective was designed by Jan Benhelm for the Quantum Simulation experiment[8] and installed by Diana Habicher during her diploma thesis [16]. The objective was designed for a distance of $58\,\mathrm{cm}$ between objective and ions [45]. All the optics drawn in Fig. 3.7 were chosen to work at two wavelengths: $397\,\mathrm{nm}$ and $729\,\mathrm{nm}$. The last lens of the objective corrects for aberrations introduced by a $6\,\mathrm{mm}$ thick viewport of the vacuum chamber. The design thickness differs from the $10\,\mathrm{mm}$ window thickness of our vacuum chamber, but we could not observe during the characterization of the addressing beam (Chapter 6) that the difference in the window thickness has any effect on the beam profile. The key idea of this objective is, on the one hand, to gather the fluorescence of the ion and, on the other hand, to focus down the $729\,\mathrm{nm}$ light for single-ion addressing. A three dimensional stage offers the possibility to adjust the position of the objective on a micrometer level.

The biggest constraint for the setup of the addressing beam was the path length from the vacuum window to the CCD camera, because it is simply too short. Since the breadboard, on which the CCD camera is placed, cannot be easily exchanged to a larger one, it was not only impossible for Diana, but it was also impossible for us to place the CCD camera further away from the vacuum window. In order to focus the fluorescence on the CCD camera with this limited path length, the distance between the objective and the vacuum window was set to $15\,\mathrm{mm}$, resulting in a magnification of $m = 22.6$ [16]. In order to achieve the maximal magnification of the ion image and the strongest focusing of the addressing beam, the objective has to be placed in a distance of $15.5\,\mathrm{mm}$ from the vacuum window.

Since other experiments have been in progress at our network node in parallel to the master's thesis research, another goal for setting up the addressing beam was to preserve the position and the alignment of the CCD detection system while achieving the smallest possible beam size of the addressing beam, in order to keep the CCD camera available for other measurements.

Our first attempts at addressing ions were performed by sending collimated light with a waist-diameter of roughly $3\,\mathrm{cm}$ into the objective. The problem we encountered was that, due to the imperfect positioning of the objective, the focus position of the beam inside the vacuum chamber was far away from the ion position.

The solution to this problem was found by using Zemax to simulate both the objective and the telescope that is used to expand the beam before it enters the objective. The conclusion of this simulation was that one can move the focus position of the beam inside the trap by adjusting the divergence of the beam. Therefore, instead of using the telescope in a configuration in which the beam is collimated when it exits the telescope, one can simply shorten the telescope length and add divergence to the beam. As a consequence, the focus of the beam moves into the direction of the objective, and one can find a configuration where the beam is focused on the ion.

In the final setup, depicted in Fig. 3.8, the light exits the fiber collimator with a waist-radius around $0.5\,\mathrm{mm}$ to fully enter the EOD[9] with an aperture size of $2\,\mathrm{mm}$. The first $\lambda/2$-plate fixes the polarization of the incident beam along the x-direction, and the second plate after the EOD optimizes the coupling to the ion [18]. The lenses of the telescope have focal lengths $f_1 = -15\,\mathrm{mm}$ and $f_2 = 250\,\mathrm{mm}$ and are placed $132.5\,\mathrm{cm}$ apart from each other.

[7] Charge-coupled Device camera Andor Solis

[8] An experiment focusing on quantum simulations with trapped ions at the Institute of Quantum Optics and Quantum Information (IQOQI).

[9] Leysop Ltd. ED2-25-AR729

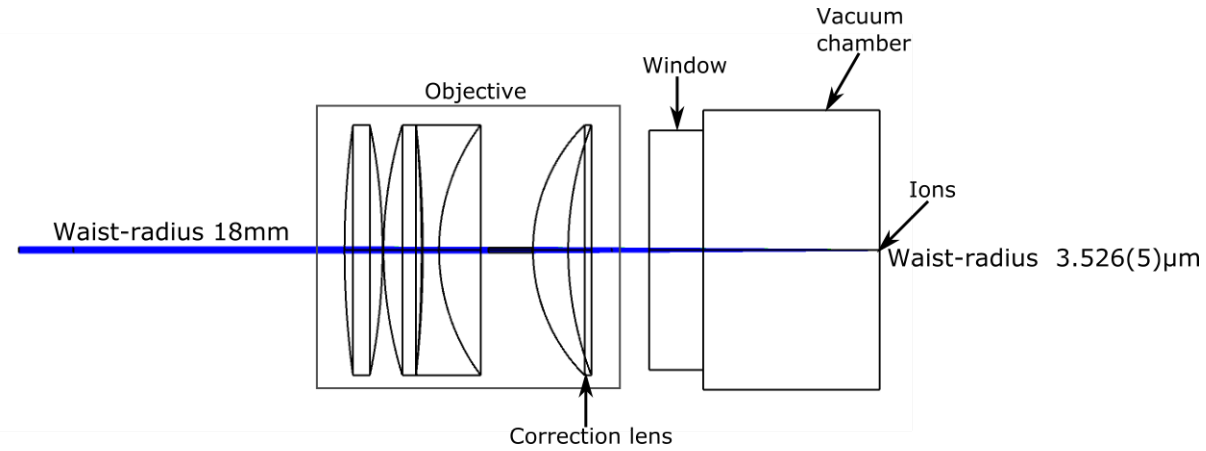

Figure 3.7: Design of the addressing objective illustrated with Zemax. A beam with waist-radius $18\,\mathrm{mm}$ is focused down to $3.526(5)\,\mu\mathrm{m}$. The objective includes a correction lens that corrects for the aberrations introduced by the window of the vacuum chamber but that has been designed for a window with a different thickness than the one we are using.

Afterwards, the beam is sent into the objective by a dichroic mirror that reflects $729\,\mathrm{nm}$ and transmits $397\,\mathrm{nm}$. The waist-radius of the addressing beam before entering the objective is around $18\,\mathrm{mm}$. The characterization of the addressing beam (Chapter 6) yields a waist-radius of $3.526(5)\,\mu\mathrm{m}$ inside the vacuum chamber. All the mirrors which are used in the optical path of the addressing beam are placed on low-thermal-drift mirror mounts[10] with a high sensitivity of 3.8 arcsec.

3.4 Detection systems

As already mentioned in the previous section, there are two different methods for detecting the state of the ion. Both methods are based on detection of the ion's fluorescence. The summary of these detection methods given in this section is based on Ref. [19], and more details can be found there. In both methods, for detecting the state of the ion, one uses the electron shelving technique [4], which is sketched in Fig. 3.9. The ion state is measured by detecting the fluorescence obtained when an ion is excited with $397\,\mathrm{nm}$ to $|4\mathrm{P}_{1/2}\rangle$. Additional $866\,\mathrm{nm}$ light repumps to $|4\mathrm{P}_{1/2}\rangle$, in order to prevent that population of the ion from getting stuck in $|3\mathrm{D}_{3/2}\rangle$. Since the two qubit states are $|4\mathrm{S}_{1/2}\rangle$ and $|3\mathrm{D}_{5/2}\rangle$, the ion is either in $|4\mathrm{S}_{1/2}\rangle$, in which case it is excited repeatedly and fluoresces, or it is in $|3\mathrm{D}_{5/2}\rangle$, in which case it cannot fluoresce. Therefore, whenever there is no measurable fluorescence, we infer that the ion is in the excited state $|3\mathrm{D}_{5/2}\rangle$, as shown in Fig. 3.10. In the context of quantum information processing, the electron shelving technique corresponds to a projective measurement in the σ_z-basis on the Bloch sphere [46].

In the case where the fluorescence detection and the $729\,\mathrm{nm}$ light are simultaneously on, the ion absorbs the $729\,\mathrm{nm}$ light and jumps into the dark state $|3\mathrm{D}_{5/2}\rangle$ which leads to a drop of the fluorescence. This jump into the dark state is called a quantum jump and offers a practical approach for aligning $729\,\mathrm{nm}$ beams to the ion because as soon as a beam is hitting the ion, the fluorescence drops are visible. Due to the immediate stimulated emission induced by the

[10] Newport SURPREMA Low-Drift Mirror Mounts

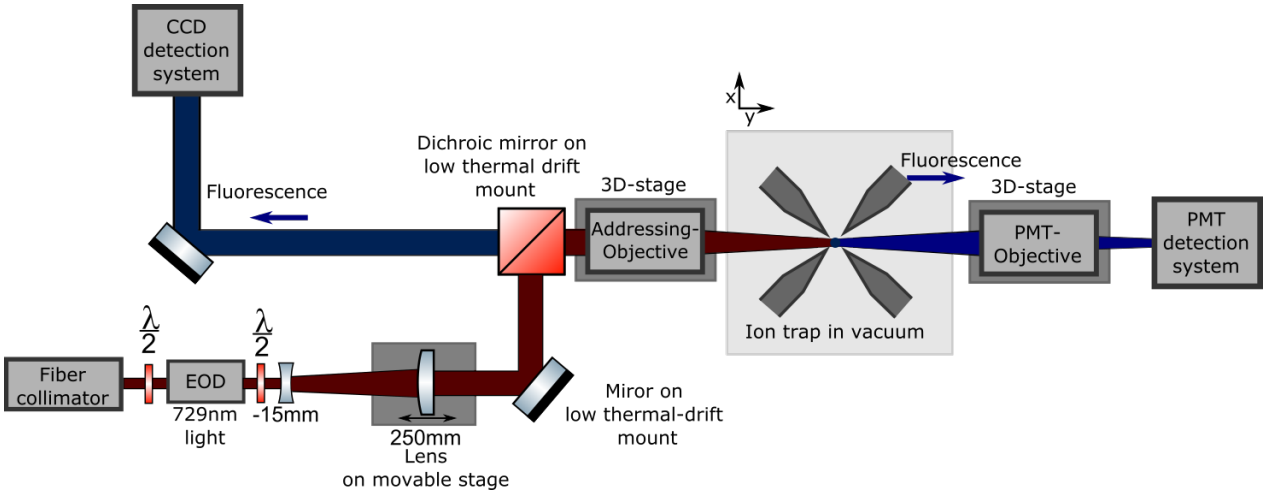

Figure 3.8: Setup of the single ion addressing beam and the detection systems. The light of the addressing beam exits a fiber collimator at the lower left of the figure and passes the electro-optical deflector (EOD). Afterwards, the beam is expanded by a telescope with two lenses of focal lengths $-15\,\mathrm{mm}$ and $250\,\mathrm{mm}$. Next, the light is sent via a dichroic mirror which transmits $397\,\mathrm{nm}$ light and reflects $729\,\mathrm{nm}$ light into the objective. The mirrors in the addressing path are mounted on low-thermal-drift mirror mounts. The same objective is used to gather ion fluorescence and to focus it on the CCD detection system. On the other side of the vacuum chamber, another objective also collects fluorescence light and focuses it onto a photo-multiplier tube (PMT).

$729\,\mathrm{nm}$ light after the ion absorbed a $729\,\mathrm{nm}$ photon, the fluorescence is halved with respect to the maximum fluorescence detected without $729\,\mathrm{nm}$ light once the alignment to the ion is optimized. Therefore, the qualitative fluorescence goes from a discrete set of jumps as in Fig. 3.10 to a smooth average.

3.4.1 PMT Detection

The PMT detects photons during electron shelving and sends the number of detected photons to the experimental control program[11]. Afterwards, the experimental control program generates a histogram of the rate of detected photons s, and due to photon statistics, the histogram follows a sum of Poissonian distributions [48]

$$g(s) = \sum_{i=0}^{n} \frac{(id)^s}{s!} \mathrm{e}^{-id}, \tag{3.15}$$

where d is the mean rate of detected photons. One expects to resolve $n+1$ peaks, where n corresponds to the number of ions, and the ith peak is equivalent i ions being bright. In order to distinguish the maxima corresponding to i and $i+1$ ions being bright, thresholds which identify the peaks in the histogram are chosen in the experimental control program. An example of such a histogram for two ions is shown in Fig. 3.11. The probability or population p_i of i ions being in the state $|S\rangle$ is calculated by [19]

$$p_i = \frac{\eta_i}{N}, \tag{3.16}$$

[11] The LabVIEW-based program is called QFP. More information can be found in Ref. [36, 19, 47].

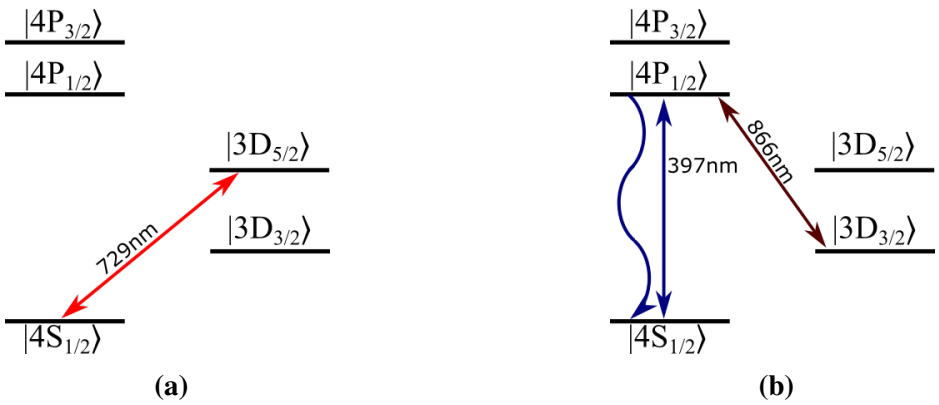

Figure 3.9: a) First before applying the electron shelving technique, the qubit state is manipulated by illuminating the ion with $729\,\mathrm{nm}$ light. b) The state detection is performed by measuring fluorescence on the $|4S_{1/2}\rangle \leftrightarrow |4P_{1/2}\rangle$ transition while the population of $|3D_{3/2}\rangle$ is actively repumped with $866\,\mathrm{nm}$ light.

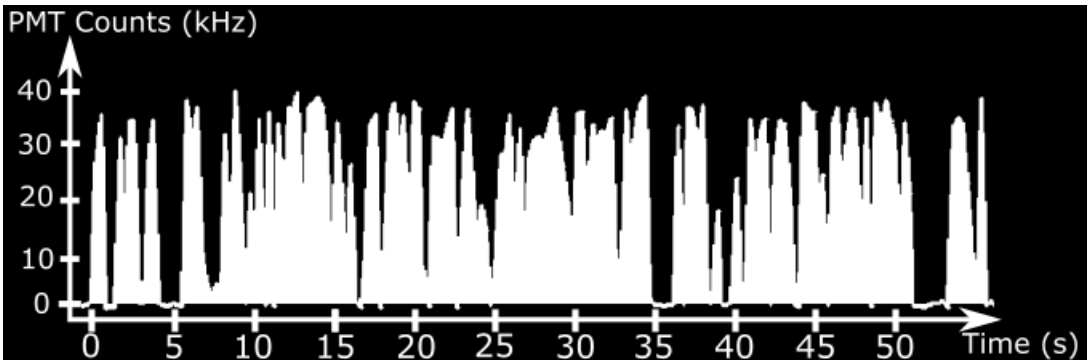

Figure 3.10: Typical screen shot of the fluorescence detection from the data acquisition software. Quantum jumps are visible, because whenever the ion is excited into $|3D_{5/2}\rangle$ state the fluorescence drops.

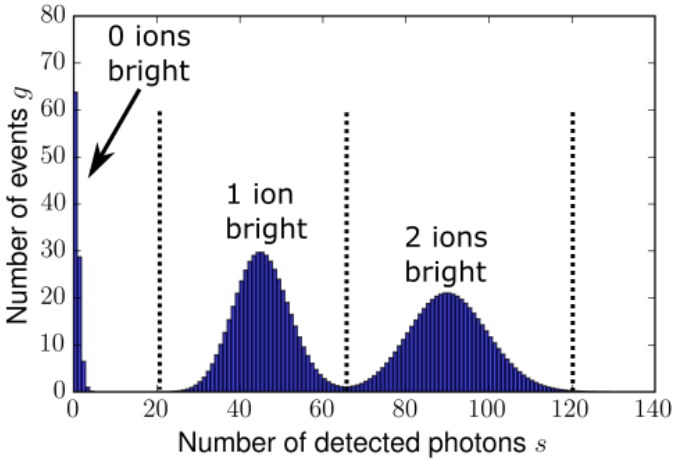

Figure 3.11: Simulation of a histogram which is used to determine the state of the ions. In an experiment, the PMT detects photon during the electron shelving, and afterwards, the experimental control program generates such a histogram. The bars indicate the thresholds in which the events are attributed to zero, one or two ions being bright. These tresholds are defined manually in the experimental control program.

where η_i denotes the number of events inside the thresholds that correspond to i ions being bright, and N is the total number of measurement cycles. For example, in the situation of two ions, p_0 corresponds the probability that the ions are in the $|DD\rangle$, p_1 corresponds to the probability that the ions are in $|SD\rangle$ or in $|DS\rangle$, and p_2 corresponds to the probability of both ions being bright. The error of these probabilities is given by the quantum projection noise [46]

$$\Delta p_i = \sqrt{\frac{(1-p_i)p_i}{N}}. \tag{3.17}$$

In the case for a probability of 0 or 1, Eq. 3.17 would lead to an error of 0 which is clearly unphysical. According to Laplace's law of succession, the minimum error of a measurement outcome is given by

$$\Delta p_{i,\min} = \frac{1}{N+d}, \tag{3.18}$$

where d denotes the number of different possible measurement outcomes [46].

3.4.2 CCD camera detection

The PMT detection does not provide fluorescence detection of individual ions since it has no spatial resolution. Individual fluorescence detection, which is necessary to distinguish, for example, between $|SD\rangle$ or $|DS\rangle$, can be achieved by using the CCD camera pictured in Fig. 3.8, which has a maximum read-out rate of $10\,\mathrm{MHz}$ [16]. During state detection, the CCD camera takes a picture (Fig. 3.12) with an exposure time that equals the detection time. This picture is analyzed afterwards, and a program determines the state of the ions. After choosing a region of interest with the size of $2\ \mathrm{pixel} \times 3\ \mathrm{pixel}$ for each ion j, the program extracts the brightness B_i for each pixel i and calculates the sum

$$S_j = \sum_i B_i \tag{3.19}$$

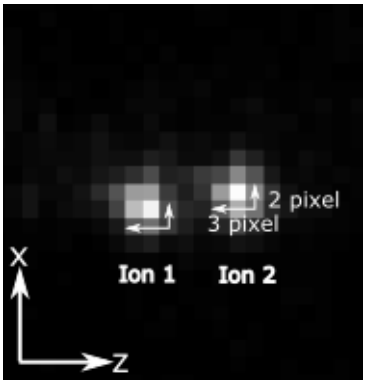

Figure 3.12: Picture of two ions taken with the CCD camera. The region of interest is indicated for each ion.

of all pixels in the region [19]. If the sum S_j is below a threshold T_j, the program notes that the ion j was in the state $|D\rangle$. On the contrary, if S_j is higher than T_j, the program assigns the ion to the bright state $|S\rangle$. The threshold

$$T_j = \frac{S_j^{\mathrm{B}} - S_j^{\mathrm{D}}}{2} \tag{3.20}$$

is extracted out of two reference pictures that are taken before starting the measurement [19]. The first reference picture yields the brightness S_j^{B}, when all ions are bright, and the second picture yields the background S_j^{D}, since all ions are dark. The excitation probability p_j is calculated by

$$p_j = \frac{\eta_j}{N}, \tag{3.21}$$

where η_j is the number of events in which the ion j was dark and N is the total number of detected events [19]. The error of the population is again given by the quantum projection noise, described by Eq. 3.17 [46].

The disadvantage of the camera detection is that the minimum detection time was in our case $3\,\mathrm{ms}$. For detection times that are too short, the measured brightness S_j is too low compared to the background S_j^{D}, and thus, there are a significant number of events where the ion is wrongly assigned to being dark. In contrast, a typical detection time of $2\,\mathrm{ms}$ for the state detection with the PMT is shorter than the minimum detection time of the camera detection.

3.5 Magnetic field stabilization

The magnetic field in the experimental setup lifts the degeneracy of the sub-states of the manifolds due to the Zeeman effect. As a consequence, the magnetic field opens up the opportunity to address individual sub-levels of $|3\mathrm{D}_{5/2}\rangle$. Moreover, we can choose the axis of the magnetic field, and we decided to set it to be perpendicular to the optical axis of the experimental cavity in order to enhance the strength of the cavity-mediated Raman transitions [36]. These Raman transitions are necessary for network protocols such as ion-photon entanglement, through which the ion's state is entangled with the polarization of a photon [12].

3.5.1 Principle of the magnetic field stabilization

The magnetic field is generated by three pairs of coils in Helmholtz configuration along the x, y and z axes. One coil along the y axis is shown in Fig. 3.13. Together, the pair of coils whose Helmholtz axes are parallel to the y and z axes produce a magnetic field of $3.26(1)\,\mathrm{G}$ orthogonal to the cavity axis. Additionally, the magnetic field along the z axis compensates for the earth's magnetic field and background magnetic field, which is generated, for example, by electric equipment.

However, the stability of the magnetic field is limiting the time after which we can retrieve quantum information stored in our network node. But before proceeding to a discussion of the influence of magnetic field fluctuations on stored quantum information, I want to introduce the concept of coherence time of an electronic state.

In a quantum network protocol in which our network node receives a photon, the quantum information is imprinted from the photon onto the state of an ion [49]. Immediately after this state transfer, the phase relation between $|S\rangle$ and $|D\rangle$ of the state $|\psi\rangle = \alpha|S\rangle + \beta|D\rangle$ with $|\alpha|^2 + |\beta|^2 = 1$ is well-defined [50]. Over time, the state decays into an incoherent mixture and after a particular time, called the coherence time, the information on the phase α and β of $|S\rangle$ and $|D\rangle$ is lost and the state $|\psi\rangle$ cannot be retrieved.

Currently, fluctuations of the magnetic field are the main source of decoherence in our experimental setup. Since the energy levels of the ion are depending on the magnetic field due to the Zeeman effect (see Sec. 2.2), fluctuations of the magnetic field lead to a modulation of the energy levels of the ion. Because the light-matter interaction (see Sec. 2.1.1) is taking place in a reference frame which rotates at a frequency set by the energy difference between $|S\rangle$ and $|D\rangle$, magnetic field fluctuations shift this reference frequency, and consequently, the two components $|S\rangle$ and $|D\rangle$ acquire a relative phase ϕ. Because the magnetic field fluctuations are unpredictable and irreproducible, we cannot compensate for the acquired relative phase ϕ. Therefore, the information on the phase α and β decays over time until the quantum information is irretrievable.

In order to elongate the storage time of our network node, it is necessary to decrease the fluctuations of the magnetic field. Therefore, an active stabilization from Spicer Consulting was installed [36]. It consists of two AC sensors, each of which measures the time-varying component of the magnetic field along three axes, and a DC-Sensor that measures the constant magnetic field. The signals of the two AC-sensors are sent into a mixer. In order to change the position at which the magnetic field is stabilized, we can adjust for each of the three axes, if either the signal of the first AC sensor or the signal of the second AC sensor contributes more to the output signal of the mixer. Afterwards, the output signal is sent into a stabilization module which drives three compensation loops that are placed, as shown in Fig. 3.13, perpendicular to the x, y and z axes. The current which is sent through the compensation loops induces a magnetic field that stabilizes the magnetic field provided by the Helmholtz coils.

3.5.2 Measurement of the coherence time

For optimizing the coherence time of the ion, it is necessary to stabilize the magnetic field at the ion position, which is achieved by changing the weighting between the input signals sent into the mixer for each axis. After the weighting of the signal of a sensor was increased or

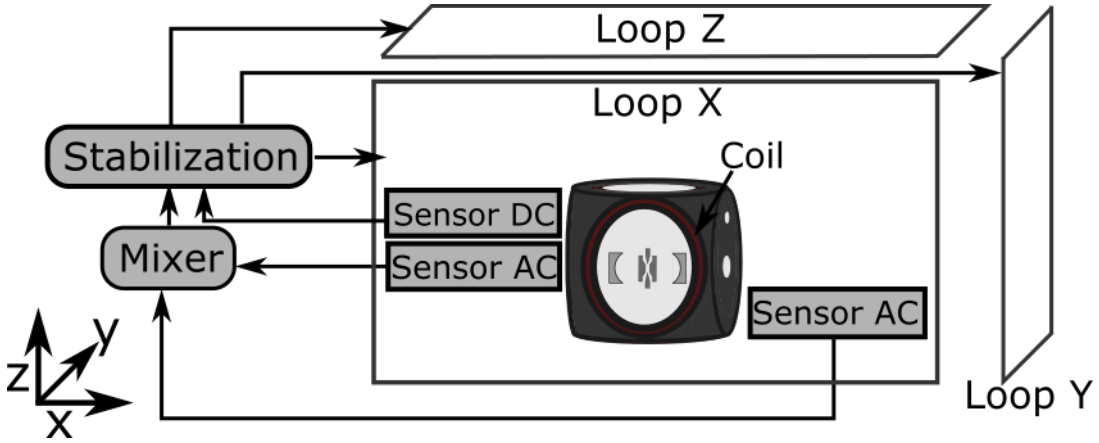

Figure 3.13: Schematic of the magnetic field stabilization. The magnetic field is produced by coils in the x-,y- and z-directions; to simplify the figure, only one coil for the field in y-direction is shown. The signals of two AC magnetic field sensors are sent into a mixer, where the signals are combined. The output of the mixer is sent into the stabilization module, along with the signal from a DC sensor. The stabilization module drives three different compensation loops which stabilize the magnetic field at the ion position.

decreased, the coherence time is measured, and if the coherence time increased, the weighting of this sensor is further increased or decreased. This optimization process is iterated until the optimal weighting between the two AC sensors is found for each axis.

In order to measure the coherence time, we perform a Ramsey measurement [51], the concept of which is shown in Fig. 3.14a. The ion is first prepared in $|S\rangle$ and then excited by a $\pi/2$ pulse to the superposition $1/\sqrt{2}(|S\rangle + |D\rangle)$. After a waiting time t, a second $\pi/2$ rotation, with a phase Φ with respect to the first pulse, is applied to the ion. As a result, the final state depends on both the acquired phase ϕ and the relative phase Φ between the two pulses.

A measurement of the probability of the ion being in $|D\rangle$ is performed as a function of the relative phase Φ according to the experimental sequence shown in Fig. 3.15. We expect that the population of $|D\rangle$ as a function of the pulse phase Φ should have the form of a the Ramsey fringe [36]

$$\rho_{\mathrm{DD}} = C\cos(\frac{\pi}{2}\Phi + \phi_0)^2 + \rho_0, \tag{3.22}$$

where the contrast C should be one, and the offset ρ_0 should be zero. A contrast less than one and a non-zero offset indicate that it is impossible to transfer the ion with the second $\pi/2$ pulse with a relative phase $\Phi = 0$ from the superposition $1/\sqrt{2}(|S\rangle + |D\rangle)$ fully to $|D\rangle$ or with a relative phase $\Phi = \pi/2$ from the superposition fully to $|S\rangle$. Here ϕ_0 denotes an arbitrary phase offset. An experimental result for such a Ramsey fringe is shown for a waiting time of $t = 300\,\mu\mathrm{s}$ in Fig. 3.16. Due to the influence of the magnetic field flcutuations during the waiting time, the fit of Eq. 3.22 yields a contrast of $C = 0.93(2)$ which is lower than one.

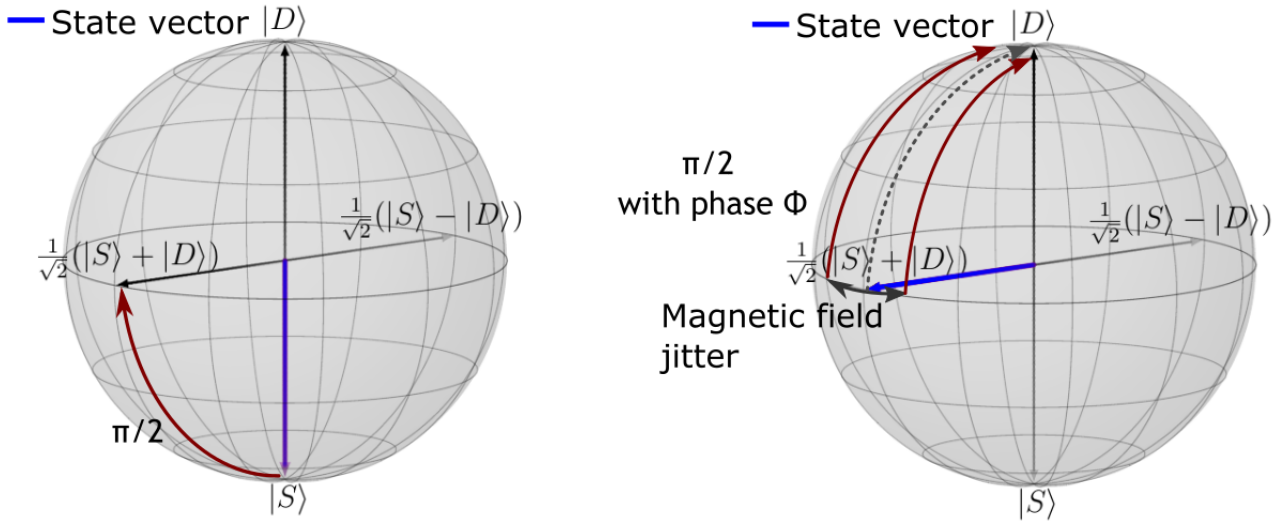

(a) **(b)**

Figure 3.14: a) First part of a Ramsey measurement, the ion is prepared in the state $|S\rangle$ and is excited into the superposition state $\frac{1}{\sqrt{2}}(|S\rangle + |D\rangle)$ by a $\pi/2$ rotation. b) Second part of a Ramsey measurement. The qubit is prepared in the superposition state $\frac{1}{\sqrt{2}}(|S\rangle + |D\rangle)$, and the states $|S\rangle$ and $|D\rangle$ acquire a relative phase ϕ due to magnetic field fluctuations. After a waiting time t, a second $\pi/2$ rotation with a relative phase Φ with respect to the first $\pi/2$ pulse is applied to the qubit. The three arrows indicate $\pi/2$ rotations with $\Phi = 0$, of which each rotates the qubit state to a different point on the bloch sphere depending on the acquired relative phase ϕ. The grey arrow corresponds to a situation in which the superposition state is not affected by magnetic field fluctuations, and the result of the $\pi/2$ pulse in this situation is $|D\rangle$. The red arrows indicate a situation in which magnetic field fluctuations add a relative phase to the superposition state. The states are close to $|D\rangle$ after the $\pi/2$ pulse but not exactly at the north pole of the Bloch sphere. Consequently, the probabilities to measure $|D\rangle$ are less than 1.

Figure 3.15: Experimental sequence of the Ramsey measurement. The sequence starts with 3 ms of state preparation. Afterwards, the first $\pi/2$ pulse is applied. After a waiting time t, the second $\pi/2$ pulse with a phase Φ is applied to the ion. The sequence ends with a 5 ms of state detection, following the methods described in the previous section.

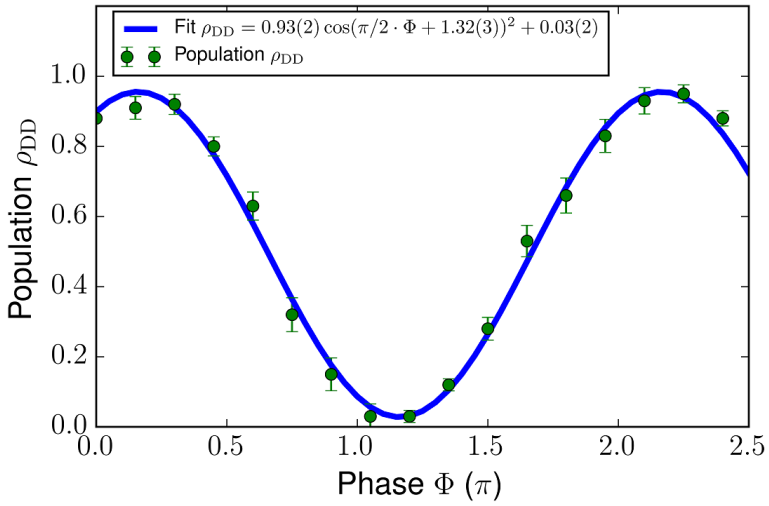

Figure 3.16: Measurement of the population of $|3D_{5/2}\rangle$ as a function of the phase Φ of the second $\pi/2$ pulse. The waiting time after the first $\pi/2$ pulse is set to 300 µs. A fit according to Eq. 3.22 yields the contrast $C = 0.93(2)$.

However, the contrast is reduced with increasing waiting times t due to the magnetic field fluctuations [18], and one can extract the coherence time τ_{coh} from a fit of [36]

$$C(t) = C_0 \exp\left(-\frac{t^2}{2\tau_{\text{coh}}^2}\right) \tag{3.23}$$

to the values of C extracted from a series of measurements such as Fig. 3.16 for varies waiting times t. The coherence time is varying for different transition from the sub-levels of $|S\rangle$ to the sub-levels of $|D\rangle$ due to the different coupling of these states to the magnetic field [20]. Therefore, as already mention in Sec. 2.2, transitions from $|4S_{1/2}, m_J = \pm 1/2\rangle$ to states with higher angular momentum than $m_J = \pm 1/2$, such as $|3D_{5/2}, m_J = \pm 3/2\rangle$, have a lower coherence time due to the stronger coupling to the magnetic field. An example measurement of the contrast as a function of the waiting time is performed for the qubit transition $|4S_{1/2}, m_J = -1/2\rangle \leftrightarrow |3D_{5/2}, m_J = -1/2\rangle$. The result is pictured in 3.17, and the coherence time of this transition is determined to be $1193(30)$ µs.

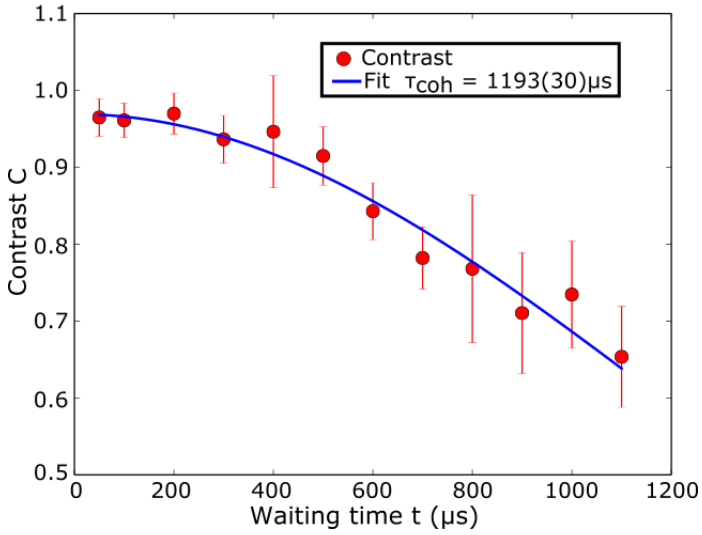

Figure 3.17: Measurement of the contrast for different waiting times between the first and the second global $\pi/2$ pulses. A fit of Eq. 3.23 yields the coherence time $\tau_{\text{coh}} = 1193\,\mu\text{s}$ for the $|4\text{S}_{1/2}, m_J = -1/2\rangle \leftrightarrow |3\text{D}_{5/2}, m_J = -1/2\rangle$ transition.

3.6 Conclusion

In this chapter, the experimental techniques and the necessary concepts for the work presented in this master's thesis were depicted. First, the working principle of the linear trap was explained, and the implementation of the trap in our experimental setup was shown. Subsequently, all the necessary laser systems were summarized. The next section described the optical paths of the $729\,\text{nm}$ light on the experiment table. An intensity stabilization was implemented to reduce the intensity fluctuations after the TA from $\Delta I_{\text{us}} = 3\%$ to $\Delta I = 1\%$. The $729\,\text{nm}$ global beams, including the new north-west global beam, which replaces the old addressing beam, were presented. These global beams will be used for the implementation of the composite qubit flip in Ch. 7. The next section focused on the technical details of the new addressing beam which will be characterized in Ch. 6 and the setup of the detection systems. The optical path of the new addressing system includes an EOD, which allows us to move the addressing beam depending on the voltage applied on the EOD. Before placing the EOD in the setup, its properties have been examined, and the results are presented in Ch. 4.

In addition to the description of the detection systems, the electron shelving technique and its implementation with the PMT and the CCD camera were explained. The presented detection methods will be used in Ch. 5 for the reconstruction of the effective phonon number of a trapped ion, for the characterization of the new addressing beam in Ch. 6 and for the implementation of the composite qubit flip in Ch. 7. This chapter concluded with a description of the magnetic field stabilization and a measurement of the coherence time of $\tau_{\text{coh}} = 1193(30)\,\mu\text{s}$ of the $|4\text{S}_{1/2}, m_J = -1/2\rangle \leftrightarrow |3\text{D}_{5/2}, m_J = -1/2\rangle$ transition.

Chapter 4

Characterization of the electro-optical deflector

An electro-optical deflector (EOD) allows us to move the addressing beam from one ion to another. Before the EOD was placed in the addressing setup, it was necessary to characterize its properties carefully. First, this chapter summarizes the working principle of an EOD. This summary is based on Refs. [44, 52], and a more detailed description can be found there. The following section describes the setup used for characterizing the EOD, and to conclude this chapter, the results of this characterization are presented.

4.1 Principle of the electro-optical deflector

An EOD consists of a hyperbolic-shaped crystal with refractive index n with electrodes placed on the sides of the crystal. A schematic of an EOD is shown in Fig. 4.1. In order to modify the deflection angle, one can change the refractive index by applying an electric field on the crystal. This effect is called the Pockels effect [44]. The electric field E is generated by applying a voltage V on the electrodes, which generates an electric quadrupole field due to the shape of the crystal [52]. As a result, the Pockels effect changes the refractive index along the optical axis of the crystal, and the gradient is given by [52]

$$\Delta n = n^3 r \frac{V}{R}, \tag{4.1}$$

depending on the applied voltage and the Pockels coefficient r of the crystal. Here R denotes the radius of curvature of the hyperbolic-shaped electrodes. Since the deflection angle depends linearly on the refractive index, a change of the refractive index leads to a change of the deflection angle by [44]

$$\Delta\theta = \Delta n \frac{L}{D} = n^3 r \frac{V}{R} \frac{L}{D} = K \cdot V, \tag{4.2}$$

where L is the length of the crystal and D the diameter of the laser beam. The deflection angle depends now on the applied voltage V and the material-dependent constant

$$K = \frac{L n^3}{RD} r. \tag{4.3}$$

This material-dependent constant determines the deflection angle as a function of the applied voltage and will be quantified in Sec. 4.3.

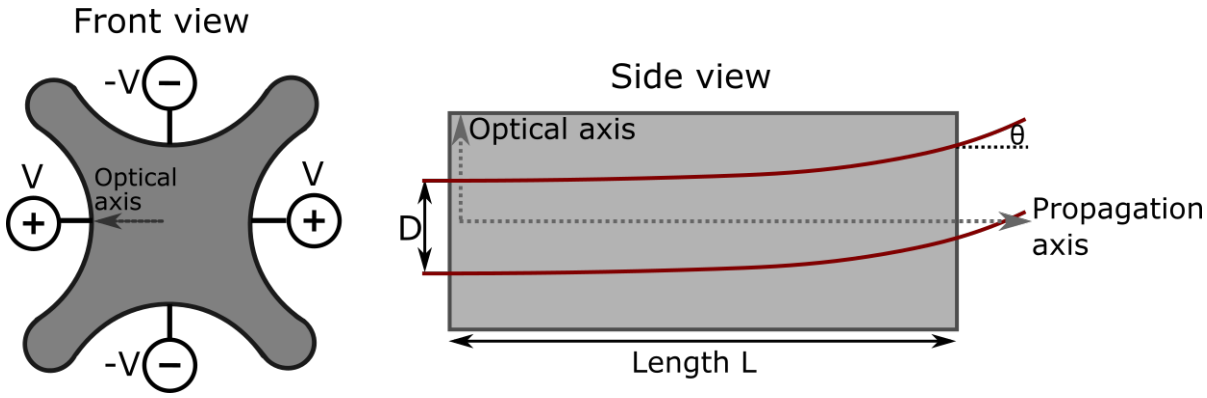

Figure 4.1: Schematic of an electro-optical deflector. The deflector consists of a hyperbolic-shaped crystal with length L. The refractive index n of the crystal can be changed by applying an voltage V on the electrodes. An incoming laser beam indicated in red will leave the EOD in an angle θ. A similiar picture can be found in Ref. [52].

4.2 Setup for characterizing the electro-optical deflector

in the previous section, we have seen how the deflection angle is connected with the applied voltage. This section focuses on the setup which has been used for the characterization of the properties of the EOD.

An overview of the setup is given in Fig. 4.2. Laser light at a wavelength of $729\,\mathrm{nm}$ is brought via a polarization-maintaining fiber from the laser to the setup. The light was produced by the old Coherent Ti:Sapph laser, which has since been replaced by the laser system described in Sec. 3.2.4. Details about the old laser system can be found in Ref. [39]. The light exits a fiber collimator, passes through a half-wave plate and enters the EOD. The deflector is a lithium niobate based crystal from Leysop Ltd.[1] with an aperture size of $2\,\mathrm{mm}$.

The deflector requires high driving voltage because typical values for the Pockels coefficient r are around $10^{-10} - 10^{-12}\,\mathrm{m\,V^{-1}}$ [44]. The deflector is driven by an amplified step function signal with a frequency about $1\,\mathrm{Hz}$ in order to resolve a clear separation between the position of a deflected beam and an undeflected beam. The driving signal is generated by a function generator and then sent into an amplifier[2]. The input signal can be amplified up to an output voltage between $-200\,\mathrm{V}$ and $200\,\mathrm{V}$, and the maximum voltage that can be applied to the deflector is $2\,\mathrm{kV}$. At the time, at which the characterization has been performed, there was not an alternative high voltage amplifier available that supports a higher output voltage than the amplifier we used. Therefore, the driving voltage of the EOD has been limited for the measurements we have performed by the maximum output voltage of the amplifier, and I would recommend to buy a new high voltage amplifier for further usage of the EOD.

[1] ED2-25-AR729

[2] Amplifier built by the electronic workshop at the University of Innsbruck

A CCD Beam Profiler[3] takes pictures of the beam profile for different deflection angles at a distance of $56(1)\,\mathrm{cm}$ from the deflector. The position of the beam profiler is chosen such that the undeflected beam hits the center of the CCD chip. Its large sensor area of $8.77\,\mathrm{mm} \times 6.6\,\mathrm{mm}$ with $0.0044\,\mathrm{px\,mm^{-1}}$ spatially resolves even beams with a higher deflection angle than the home-build amplifier can provide.

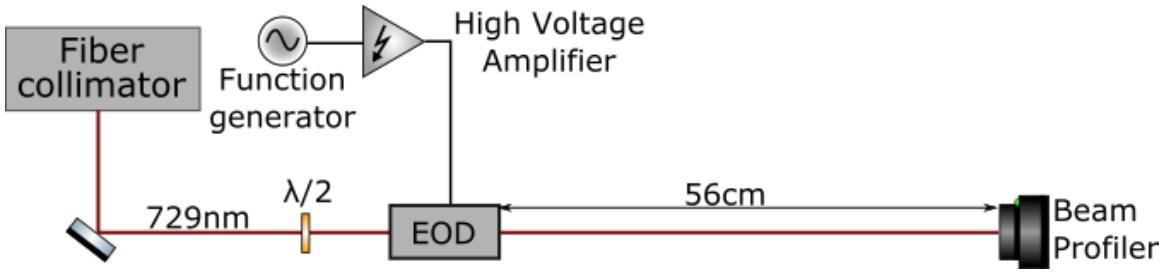

Figure 4.2: Setup for characterizing the EOD. Laser light at a wavelength of $729\,\mathrm{nm}$ is collimated by a fiber collimator and passes through a half-wave plate. The EOD is driven by a high voltage amplifier and deflects the incident light. Afterwards, a beam profiler, which is placed $56(1)\,\mathrm{cm}$ away from the deflector, images the deflected beam.

4.3 Results

4.3.1 Dependence on the polarization of the incident light

Before proceeding to the measurement of the proportionality constant, which connects the deflection angle with the applied voltage, we first investigate the dependence of the deflection angle on the polarization of the input beam due to the birefringence of the EOD crystal. First, the amplitude of the driving signal of the deflector is set to $80\,\mathrm{V}$. The polarization of the beam is changed by rotating the half-wave plate, and pictures of the deflected and undeflected beams are taken for different wave-plate settings. An example of such a picture is shown in Fig. 4.3a. We assume the beam which exits the fiber has a Gaussian beam profile. Therefore, a program (App. A.1) finds the center of the beam along the x axis by summing up the intensity over the y-axis and fitting a gaussian

$$I(x) = I_0 + A\mathrm{e}^{\frac{(x-x_0)^2}{2\sigma^2}} \tag{4.4}$$

to the data. Here I_0 corresponds to an offset, A to the amplitude, x to the pixel number and σ to the standard deviation. An example for a profile after one axis has been integrated is shown with the corresponding fit in Fig. 4.3b. Afterwards, the program calculates the spatial deflection

$$d = |x_{0,\mathrm{d}} - x_{0,\mathrm{u}}| \tag{4.5}$$

as the absolute difference between the center $x_{0,\mathrm{d}}$ of the deflected beam and the center $x_{0,\mathrm{u}}$ of the undeflected beam. The same procedure is repeated to find the deflection along the y-direction. In the ideal case, the deflection should be perpendicular to the electric field, enabling optimal switching along only one axis.

[3] BC106N-VIS(/M) from Thorlabs

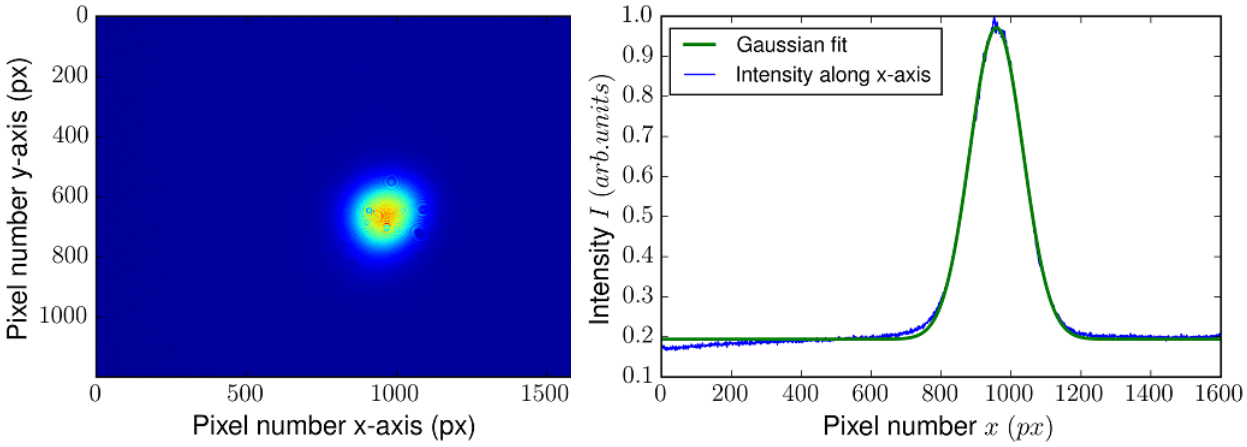

(a) **(b)**

Figure 4.3: a) Example of a beam profile of an undeflected beam taken with the CCD Beam Profiler. b) Intensity vs. pixel number along the x-direction. A fit according to Eq. (4.4) finds the center of the beam.

The deflection along the x- and y-axes is shown for different settings of the half-wave plate in Fig. 4.4. A systematic error of the angle of the half-wave plate is introduced by the read-out error of the scale on the plate and is assumed to be $2°$. The statistical error for the deflection is given by the errors of the fits and Gaussian error propagation. One can clearly see the strong dependence of the deflection on the polarization due to the birefringence of the deflector crystal. Hence, it is necessary to choose a setting of the half-wave plate that is around $50°$ to minimize the contribution of the deflection parallel to the electric field. Otherwise, it could happen in future experiments that, when switching with the deflector from one addressed ion to another, the beam position would not only change as desired along the trap axis, but would also change along the radial axis. This radial displacement would lead to a different coupling of the laser beam to the addressed ion as compared to the previous ion. Since one fixes the polarization of the light before the EOD, one needs an additional $\lambda/2$-plate after the deflector for optimizing the coupling strength to the ion [18].

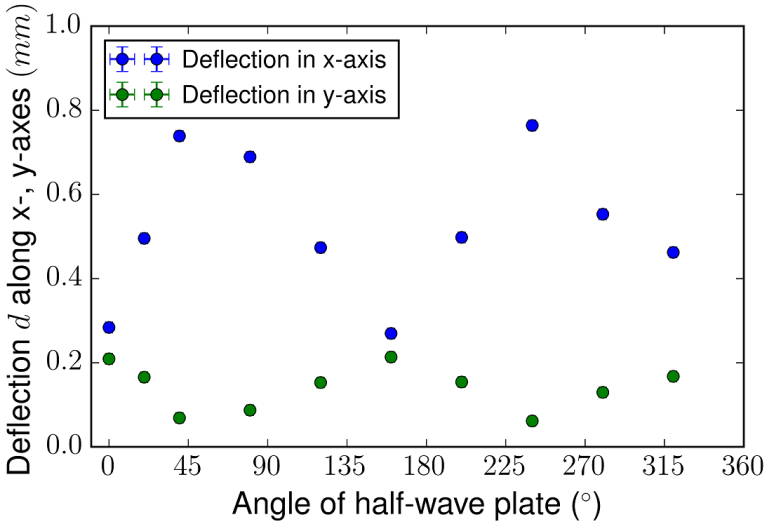

Figure 4.4: Deflection for the x- and y-direction for various angles of the half-wave plate. The error bars are obscured by the data points.

4.3.2 Dependence of the deflection angle on the applied voltage

As explained in Sec. 4.1, the deflection angle depends linearly on the applied voltage of the electro-optical deflector. Therefore, it is necessary to quantify the deflection constant K from Eq. 4.2 in order to know how much voltage one needs to apply for a specific deflection angle. The wave-plate setting is fixed to $50°$ for achieving the highest deflection perpendicular to the electric field. Similarly to the polarization calculation in the previous section, the spatial deflection d is calculated by a program (App. A.2) via the pictures and the fitting procedure. The deflection angle is calculated as

$$\theta = \arctan\left(\frac{d}{l}\right), \tag{4.6}$$

where $l = 56(1)\,\mathrm{cm}$ is the distance between the deflector and the CCD Beam Profiler. The output voltage of the amplifier is directly monitored via a display on the front of the amplifier.

The deflection angle for different deflector voltages is shown in Fig. 4.5. A linear fit determines the constant $K = 0.0025(1)\,\mathrm{mrad\,V^{-1}}$, and therefore, the maximal deflection angle is $5.0(2)\,\mathrm{mrad}$ at a driving voltage of $2\,\mathrm{kV}$. The signal was observed to oscillate by around 5%, and the read-out error of the deflector voltage is estimated to be around 5%. The error of the deflection angle arises from the uncertainties of the fits and the measurement precision of the length l. The deviations of the data points from the linear fit are introduced by polarization drifts of the incident beam due to inaccurate alignment to the polarization axis of the fiber. Unfortunately, there is no data sheet for this deflector available, and thus, it is not possible to compare the results with specifications from the manufacturer.

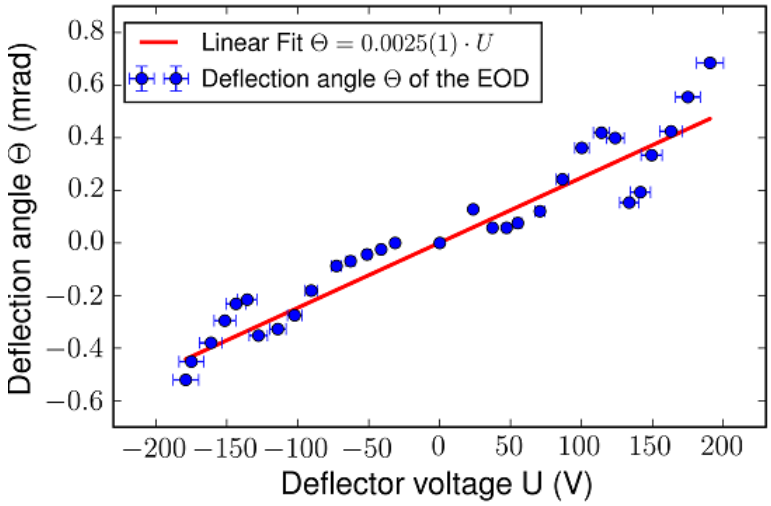

Figure 4.5: Plot of the deflection angle against the applied voltage. Based on Eq. 4.2 a linear fit with an offset is applied. The error bars of the deflection angle are hidden by the symbols of the data points

4.3.3 Conclusion

The key results obtained from the characterization of the electro-optical deflector are the observation of the dependence of the deflection angle on the polarization of the input beam and the measurement of the deflection constant $K = 0.0025(1)\,\mathrm{mrad\,V^{-1}}$. For proper deflection in the horizontal direction, the incident beam should have a linear polarization perpendicular to the applied electric field. Additionally, it is necessary to keep the polarization of the incident beam as stable as possible, otherwise deviations from the expected deflection angle will occur. The measurement shown in Fig. 4.5 could be improved by installing a half-wave plate and a polarizing beam-splitter (PBS) in front of the deflector. In this way, the light transmitted by the PBS into the deflector would have a fixed polarization. Nevertheless, this approach of cleaning the polarization would not be suitable for the addressing path, described in Sec. 3.3.3, because polarization drifts before the beam-splitter would lead to intensity fluctuations of the transmitted light. These intensity fluctuations would be more critical than small drifts of the deflection angle because, as described in Sec. 3.3.1, they damp Rabi oscillations of the ion and are consequently impractical for the measurements which will be presented in Chs. 5, 6 and 7.

Chapter 5

Preparation of the ion

State preparation is one of the most important steps in an experimental sequence for trapped ion experiments. Many quantum computation and quantum network protocol rely on the fact that the state of the ion can be prepared in a target electronic and motional quantum state before a quantum gate operation is applied [3]. The target electronic state for the state preparation is the electronic ground state of our qubit transition. In order to initialize the ion in the ground state, the population in excited states is transferred via the repumping procedures described in Sec 2.2 using $854\,\mathrm{nm}$, $866\,\mathrm{nm}$ and $729\,\mathrm{nm}$ laser light.

The target motional state is prepared by cooling and appropriate optical pumping of the ion, and the goal for this part of the state preparation is a reduction of the phonon number close to the Doppler limit or even below for two reasons. First, as I will describe in this chapter, a badly cooled ion exhibits a broad thermal distribution of phononic excitation, which can be observed as a collapse of the Rabi oscillations [18]. This dephasing of the different vibrational states presents a problem for several quantum gates, for example, for the composite qubit flip described in Ch. 7. Another important example where this dephasing is cumbersome is the $\pi/2$ pulse that is necessary for the coherence-time measurement from Sec. 3.5.2. For an amount of phononic excitation significantly larger than the Doppler limit, it will be impossible to coherently transfer population from the state $|S\rangle$ to the superposition $|S+D\rangle$ with a probability of 99% or higher.

The second reason for cooling the ion is the spread of the ion's wave packet for an amount of phonons in the system larger than the Doppler limit. This effect is important as the coupling strength of the ion to the cavity mode depends on the wave packet spread [36]. Therefore, it is necessary to check the effectiveness of the cooling before running any network protocol or quantum gate. This chapter summarizes a method for reconstructing the effective phonon number of a trapped ion. The presented summary reproduces the results of Chapter A.1 of Ref. [18] and discusses them in the context of the work carried out during this master's thesis research. In order to quantify the ion temperature, the reconstruction is implemented as a tool for in-situ analysis of the cooling and is applied to Doppler- and sideband-cooled ions.

5.1 Procedure for quantifying the ion temperature

The thermal state of the ion can be described by a distribution of phonon numbers. In a 1D harmonic potential, the occupation probability

$$p_n = \frac{1}{\bar{n}+1}\left(\underbrace{\frac{\bar{n}}{\bar{n}+1}}_{:=x}\right)^n = \frac{1}{\bar{n}+1}\cdot x^n \tag{5.1}$$

of the motional state $|n\rangle$ depends on the mean phonon number $\bar{n}$ [53]. If the ion is now excited by a laser on the carrier transition, the population of the excited state undergoes Rabi oscillations as a function of the excitation time. As shown in Sec. 2.1.1, the probability to find the ion in the excited state evolves with the time t as

$$\rho_{DD}(t) = \frac{1}{2}\left(1 - \sum_{n=0}^{\infty} p_n \cos(\Omega_{n,n} t)\right) \tag{5.2}$$

with a Rabi frequency

$$\Omega_{n,n} = \Omega(1-\eta^2 n) \tag{5.3}$$

that depends on the Lamb-Dicke parameter η and the phonon number n. In contrast to Eq. 2.15, in which the motional state is a single Fock state, the motional state here is described by a phonon number distribution. Therefore, the excitation probability becomes [18]

$$\rho_{DD}(t) = \frac{1}{2}\left(1 - \frac{1}{\bar{n}+1}\sum_{n=0}^{\infty} x^n \cos(\Omega t(1-\eta^2 n))\right) \tag{5.4}$$

$$= \frac{1}{2}\left(1 - \mathrm{Re}\left(\frac{1}{\bar{n}+1}\sum_{n=0}^{\infty} x^n \exp(\Omega t(1-\eta^2 n))\right)\right) \tag{5.5}$$

$$= \frac{1}{2}\left(1 - \mathrm{Re}\left(\frac{1}{\bar{n}+1}\frac{\exp(i\Omega t)}{1-x\exp(-i\Omega\eta^2 t)}\right)\right) \tag{5.6}$$

$$= \frac{1}{2}\left(1 - \frac{1}{\bar{n}+1}\frac{\cos(\Omega t)(1-x\cos(\Omega t\eta^2)) + x\sin(\Omega t)\sin(\Omega t\eta^2)}{1+x^2-2x\cos(\Omega t\eta^2)}\right). \tag{5.7}$$

This result can be simplified by approximating

$$\exp(-i\Omega t\eta^2) \approx 1 - i\Omega t\eta^2 \tag{5.8}$$

and defining the effective phonon number [18]

$$n_{\mathrm{eff}} = \eta^2 \bar{n}. \tag{5.9}$$

Thus, Eq. 5.5 can be written as

$$\rho_{DD}(t) = \frac{1}{2}\left(1 - \frac{\cos(\Omega t) + (\Omega n_{\mathrm{eff}} t)\sin(\Omega t)}{1+(\Omega n_{\mathrm{eff}} t)^2}\right). \tag{5.10}$$

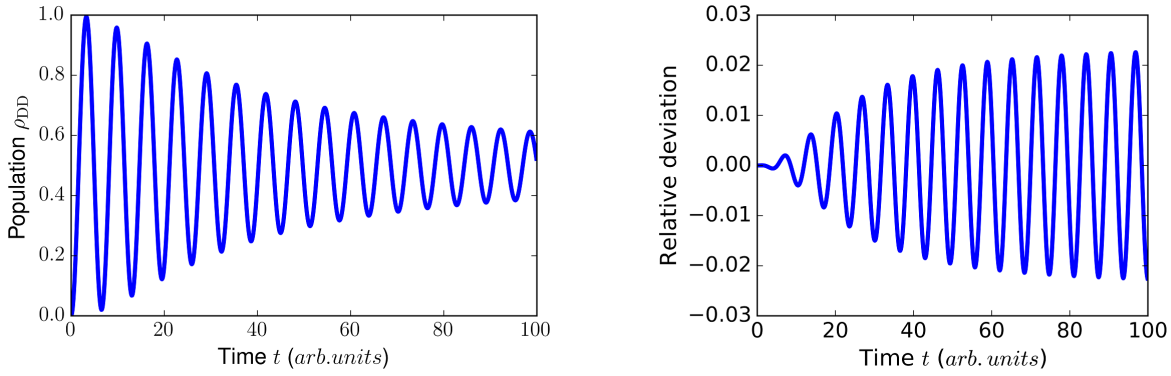

(a) **(b)**

Figure 5.1: a) Evolution of the excitation probability in time according to Eq. 5.5. The ion is trapped by a one dimensional harmonic trap, and the mean phonon number is assumed to be $\bar{n} = 10$. The cut-off phonon number for the sum in 5.5 is $n_{\max} = 50000$. The coupling constant Ω is set to $\Omega = 1$, and the Lamb-Dicke parameter is $\eta = 0.065$. b) Relative deviation of the excitation probability according to Eq. 5.10 from the excitation probability shown in a). The parameters are chosen to be the same as for figure a). A similar graph can be found in Ref. [18]

It is now possible to extend this result straightforwardly to the case of a three-dimensional trap because the effective phonon number in a three-dimensional harmonic potential characterized by three vibrational modes is [18]

$$n_{\text{eff}} = \sum_{i=0}^{2} \eta_i^2 \bar{n}_i. \tag{5.11}$$

Hence, a given measurement of the excitation probability can be associated with the effective phonon number. The advantage of the effective phonon number is that it is independent of the trap dimension; otherwise, it would be impossible to deduce the average phonon number $\bar{n}$ in more than one dimension from a fit of Eq. 5.10.

One should consider the deviation of Eq. 5.10 from the solution of Eq. 5.5, shown in Fig. 5.1a, due to the approximation carried out. Evidently, the relative deviations, pictured in Fig. 5.1b, are on the level of ± 0.02 after the tenth Rabi oscillation, and consequently the uncertainty of the effective phonon number that can be reconstructed via fitting of Eq. 5.10 increases. However, since we are not using a fit of Eq. 5.10 as a tool for phonon number reconstruction on a precision level of 1% but rather as a test of our cooling procedures with the effective phonon number as a feedback, the deviations are irrelevant for the purpose of this tool because a precision on the level of 5% is sufficient.

5.2 Application of the effective phonon number reconstruction

In order to use Eq. 5.10 to reconstruct both the effective phonon number and the Rabi frequency, one excites the ion on the $|\mathrm{S}_{1/2}, m_J = -1/2\rangle \rightarrow |\mathrm{D}_{5/2}, m_J = -1/2\rangle$ transition and measures

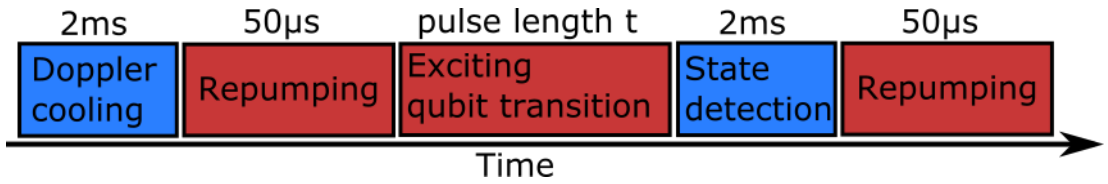

Figure 5.2: Schematic of the experimental sequence used for measuring Rabi oscillations. The experimental sequence starts with Doppler cooling for a typical interval of 2 ms. Next, a 50 µs period of repumping is used to repump the population from $|\mathrm{S}_{1/2}, m_J = 1/2\rangle$. Afterwards, the 729 nm laser is switched on for a pulse length t and excites the $|\mathrm{S}_{1/2}, m_J = -1/2\rangle \rightarrow |\mathrm{D}_{5/2}, m_J = -1/2\rangle$ transition. The state of the ion is detected for an interval of 2 ms, followed by repumping back into $|\mathrm{S}_{1/2}, m_J = -1/2\rangle$.

the excitation probability ρ_{DD}. A schematic of the experimental sequence is drawn in Fig. 5.2.

The experimental sequence starts with 2 ms of Doppler cooling as described in Sec. 2.1.2. As already mentioned in Sec. 3.5.2, some of the ion population gets stuck in the sub-level $|\mathrm{S}_{1/2}, m_J = 1/2\rangle$ due to spontaneous decay during the cooling procedure, and therefore, one needs to repump via optical pumping into $|\mathrm{S}_{1/2}, m_J = -1/2\rangle$. Afterwards, the $|\mathrm{S}_{1/2}, m_J = -1/2\rangle \rightarrow |\mathrm{D}_{5/2}, m_J = -1/2\rangle$ transition is excited for a variable pulse length t, followed by 2 ms of state detection via the PMT described in Sec. 3.4.1. As the last step, the 854 nm laser repumps the population from $|\mathrm{D}_{5/2}\rangle$ back to the ground state $|S_{1/2}\rangle$. This sequence is repeated typically 100 times, and the population is calculated according to the method from Sec. 3.4.1. The population measurement is performed for varying pulse lengths, and afterwards, a program fits Eq. 5.10 to the excitation probability.

An example python script that fits Eq. 5.10 to an population measurement can be found in App. B, and a measurement of Rabi oscillations with the corresponding fit is shown in Fig. 5.3. One can see the collapse of the Rabi oscillations due to the dephasing of the different motional states. The reconstructed Rabi frequency $\Omega = 0.1570(3)\,\mathrm{MHz}$ has a low relative error $\Delta\Omega = 0.2\%$. This precision makes this method very useful for the upcoming Ch. 6, in which a measurement of the Rabi frequency is presented as a function of the ion position.

The reconstructed effective phonon number, in this case, $n_{\mathrm{eff,dopp}} = 0.10(1)$, is used on a daily basis as feedback on how well the Doppler cooling procedure is working. Typically, one measures the effective phonon number and afterwards adjusts experimental parameters, such as the frequency of the 397 nm laser, iterating this process until the lowest effective phonon number is achieved. Since this optimizing procedure is independent of the cooling technique, it is also applicable to sideband cooling.

The population measurement was repeated with sideband cooling in addition to Doppler cooling in order to compare the different cooling techniques. The experimental sequence is shown in Fig. 5.4. The major difference with respect to the sequence used previously is the additional sideband cooling, described in Sec. 2.1.3, and an extra 50 µs of repumping into $|\mathrm{S}_{1/2}, m_J = -1/2\rangle$ after the sideband cooling. The sideband cooling here is performed on both the axial and the radial modes.

The result is shown with the corresponding fit in Fig. 5.5. First, one can see the damping due to heating decreased significantly. An excitation of $\rho_{\mathrm{DD}} = 0.96(2)$ is measured after the eleventh Rabi oscillation, which is significantly higher than the population of $0.59(4)$ of the Doppler-cooled ion after the same number of oscillations. This result is reflected in the ef-

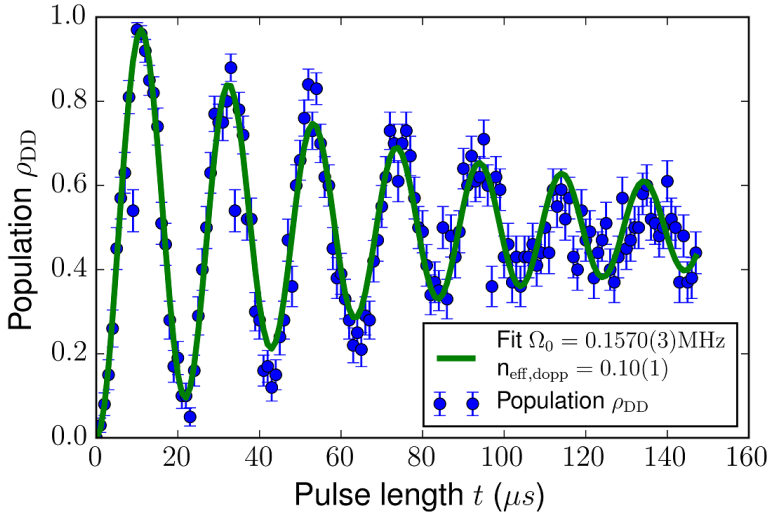

Figure 5.3: Measurement of the population ρ_{DD} as a function of the pulse length t. The error of the population is given by quantum projection noise, explained in Sec. 3.4. A fit according to Eq. 5.10 is applied and yields a Rabi frequency $\Omega = 0.1570(3)\,\mathrm{MHz}$ and an effective phonon number $n_{\mathrm{eff,dopp}} = 0.10(1)$.

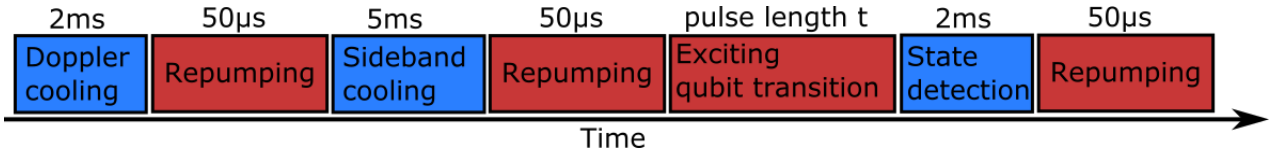

Figure 5.4: Schematic of the experimental sequence. The sequence is similiar to the one shown in Fig. 5.2 except for an additional $5\,\mathrm{ms}$ of sideband cooling and $50\,\mu\mathrm{s}$ of repumping.

fective phonon number $n_{\mathrm{eff,sb}} = 0.013(2)$, which is an order of magnitude smaller than the Doppler-cooled mean phonon number $n_{\mathrm{eff,dopp}} = 0.10(1)$.

The practical limit of the fitting procedure lies in the amount of data necessary for retrieving lower phonon numbers. For example, in the case of a measurement in which the damping of the Rabi oscillations is not visible, the fitting routine will have difficulty converging. Thus, it is necessary to take data for long enough pulse lengths such that the amplitude of the oscillations decreases. In the case of sideband cooling of the radial and the axial modes, the measurement time for one data point can take up to $10\,\mathrm{s}$. Practically speaking, the time required in the laboratory for a scan that is long enough to enable convergence of the fit, can be up to 30 to 60 minutes. Consequently, the fitting tool is more practical for improving the Doppler cooling than the sideband cooling because a measurement takes in this case only up to one to two minutes. At the moment, the model also does not include decoherence induced by intensity or magnetic field fluctuations, which play a significant role for longer scans.

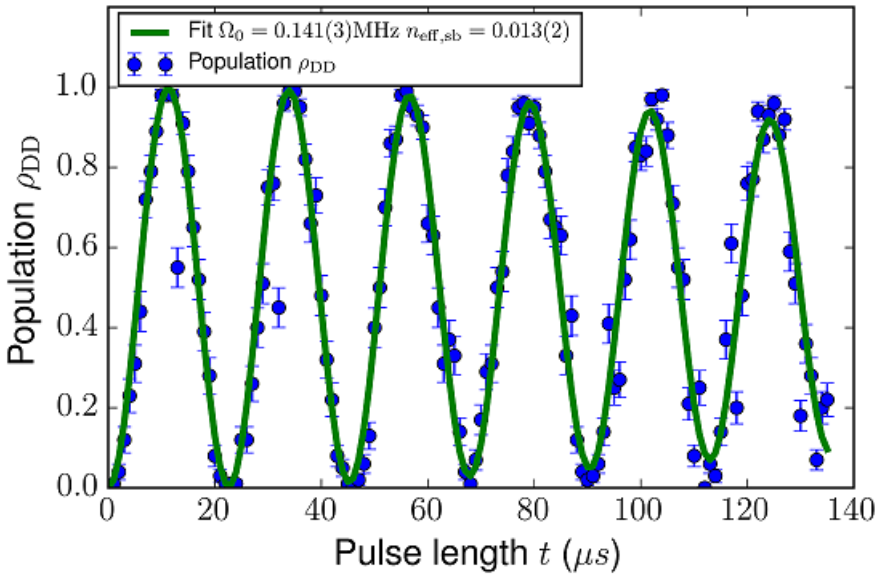

Figure 5.5: Measurement of the population ρ_{DD} of a sideband-cooled ion as a function of the pulse length t. Both the axial and the radial modes of the ion were cooled during the sideband cooling. A fit of Eq. 5.10 yields the Rabi frequency $\Omega = 0.141(3)\,\mathrm{MHz}$ and the effective phonon number $n_{\mathrm{eff,sb}} = 0.013(2)$. The measurement was performed with a different power of the $729\,\mathrm{nm}$ light.

5.3 Conclusion

In this chapter, a method was presented that enables reconstruction of the effective phonon number and the Rabi frequency via fitting Eq. 5.10 to a measurement of the ion's population when driven on the qubit transition. The effective phonon number can be used as feedback for optimizing the cooling procedures, which comprise one part of state preparation. Furthermore, the tool extracts the Rabi frequency with a low statistical uncertainty and thus is very practical for the measurements presented in the next chapter. The practical limit for the tool is the time required for measuring sufficient data points that the fitting procedure converges. The measurement time can take up to an hour for sub-Doppler cooling techniques like sideband cooling. Thus, the tool is more practical for optimizing Doppler cooling than for more time-intensive cooling techniques.

Chapter 6

Characterization of the single-ion addressing beam

The single-ion addressing beam is used for individual manipulation of ions in an ion crystal. The first requirement for an addressing beam that needs to be fulfilled is a beam size which is smaller than the distance between the ions [19]. For example, mapping the state of two ions from $\phi = |SS\rangle$ to $\phi = |SD\rangle$ is only possible with a high probability if the beam size fulfills this condition. Otherwise, the coherent manipulation of the addressed ion will also affect the unaddressed one. The result is then a superposition state $\phi = a|SS\rangle + b|SD\rangle + c|DS\rangle + d|DD\rangle$ with the complex amplitudes a, b, c and d.

This chapter examines the beam profile of the single-ion addressing beam which has been set up in the framework of this master's thesis. First, the beam size along the trapping axis is measured as a function of the telescope position. The intensity of the beam is retrieved by extracting the Rabi frequency with the tool presented in Sec. 5.1. Second, the population of the unaddressed ion is measured as a figure of merit for the cross-talk of the addressing beam.

6.1 Beam profile of the addressing beam

Before proceeding to the measurement of the cross-talk, the spatial profile of the addressing beam is examined. The beam waist of the single-ion addressing beam is measured by using the ion as a probe for the intensity of the beam. We use the tool presented in Sec. 5.1 to retrieve the Rabi frequency from a measurement of Rabi oscillations. The Rabi frequency Ω is related to the intensity of the beam according to [20]

$$I \propto \Omega^2. \tag{6.1}$$

It is not necessary to determine the intensity of the beam exactly, since the beam waist is independent of the absolute value of the intensity.

The ion position is varied by changing the endcap voltages of the trap. It is necessary to convert the voltage change into micrometers, and the conversion factor is retrieved by using the distance between two ions as measured on the CCD camera as a reference. The ion-ion distance of the image shown in Fig. 6.1a is calculated by summing the intensity along the x axis and then

performing a fit of the sum of two Gaussians according to

$$I(z) = I_0 + A_0 \mathrm{e}^{\frac{(z-z_0)^2}{2\sigma_0^2}} + A_1 \mathrm{e}^{\frac{(z-z_1)^2}{2\sigma_1^2}}. \tag{6.2}$$

The centers $z_0 = 17.20(3)\,\mathrm{px}$ and $z_1 = 22.35(3)\,\mathrm{px}$ of the Gaussians, shown in Fig. 6.1b, correspond to the ion positions along the z axis. Here A_1 and A_2 denote the amplitudes of the Gaussians, I_0 is an offset introduced by background, and σ_0 and σ_1 correspond to the widths of the Gaussians. The widths are not expected to be the same because of aberrations in the image. The implemented python code is included in App. C.1.

The ion-ion distance of $5.15(4)\,\mathrm{px}$ determined from Fig. 6.1b is now used to calculate the conversion factor. The real distance between the trapped ions is given by [27]

$$\delta z = 2 \cdot \left(\frac{e^2}{16\pi\epsilon_0 M \omega_z^2} \right)^{1/3} = 5.59(7)\,\mu\mathrm{m} \tag{6.3}$$

and depends on the axial frequency ω_z, which is $\omega_z/2\pi = 1.002\,70(10)\,\mathrm{MHz}$ for an endcap voltage of $770\,\mathrm{V}$. In the case of a $^{40}\mathrm{Ca}$ ion, the mass equals $M = 40\,\mathrm{u}$. Here e denotes the elementary charge and ϵ_0 the vacuum permittivity. The axial frequency is determined via the spectroscopic method described in Ch. 3.4 and Ch. 6.1 of Ref. [18]. Since a change of one volt of the voltage applied on the endcap electrodes moves the ion by one pixel in the image of the CCD camera, the relation

$$5.15(4)\,\mathrm{px} \mathrel{\widehat{=}} 5.59(7)\,\mu\mathrm{m} \rightarrow 1\,\mathrm{px} \mathrel{\widehat{=}} 1.08(8)\,\mu\mathrm{m} \tag{6.4}$$

connects a $1\,\mathrm{V}$ change on the endcap voltage to a movement of $1.08(8)\,\mu\mathrm{m}$.

After we determined a conversion for the change on the endcap voltage into a movement of the ion in micrometers, we perform a direct measurement of the beam size. The beam profile along the z axis is retrieved by moving the ion in steps of $1\,\mathrm{V}$ of the endcap voltage and measuring the Rabi frequency at each point using the the tool from Sec. 5.1. A schematic of the measurement is shown in Fig. 6.2. As described in Sec. 3.3.3, the position of the beam waist can be changed by adjusting the position of the second lens of the telescope in the addressing path because the length of the telescope sets the divergence of the beam. A change of the divergence moves the position of the beam waist w_0 along the y axis inside the vacuum chamber, and therefore enables us to measure the beam radius for different telescope lengths l. The beam radius at which the beam intensity reaches $1/e^2$ of its maximum value is described by [44]

$$w(l) = w_0 \sqrt{1 + \left(\frac{l - l_0}{l_R} \right)^2}, \tag{6.5}$$

whereas the telescope length l_0 corresponds to the length at which the beam waist w_0 is achieved [44]. The length at which the beam radius increased to $\sqrt{2} \times \omega_0$ is called the Rayleigh length, which is given by l_R and can also be extracted from our measurements. This quantity provides information about the necessary stability of the telescope length since for a small Rayleigh length, fluctuations of the length have a stronger influence on the beam size as compared to the case of a large Rayleigh length.

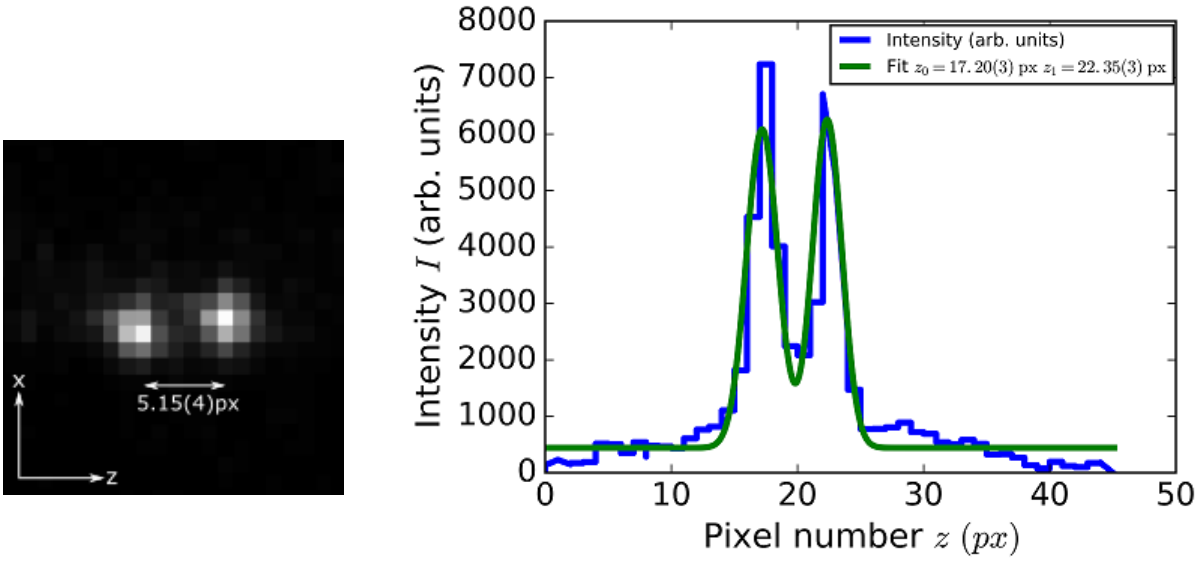

(a) **(b)**

Figure 6.1: a) Picture of the fluorescence of two ions taken with the CCD camera. b) Intensity of the image along the trapping axis. A fit of two Gaussians according to Eq. 6.2 yields the centers $z_0 = 17.20(3)$ and $z_1 = 22.35(3)$ of the two peaks, which correspond to the ion positions.

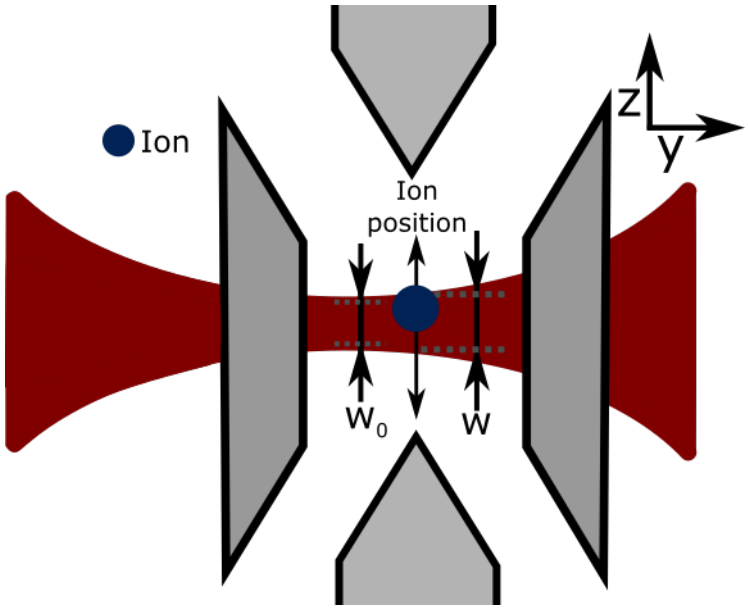

Figure 6.2: Schematic of the waist measurement. The trapped ion is moved along the z axis by changing the voltage on the endcaps of the linear Paul trap. By measuring Rabi oscillations for different ion positions, one reconstructs the intensity profile along the z axis. By fitting a Gaussian to this intensity profile, one extracts the radius $w(l)$, where l denotes the length of the telescope.

The results of the beam profile measurement for different telescope lengths are shown in Fig. 6.3. A curve fit of Eq. 6.5 yields the minimum achievable waist $w_{0,\mathrm{fit}} = 3.24(5)\,\mu\mathrm{m}$ at a telescope length of $l_0 = 132.75(1)\,\mathrm{mm}$ and the Rayleigh length $l_\mathrm{R} = 0.56(4)\,\mathrm{mm}$. As already mentioned in Sec. 3.3.2, the waist denotes to the $1/e^2$ intensity radius.

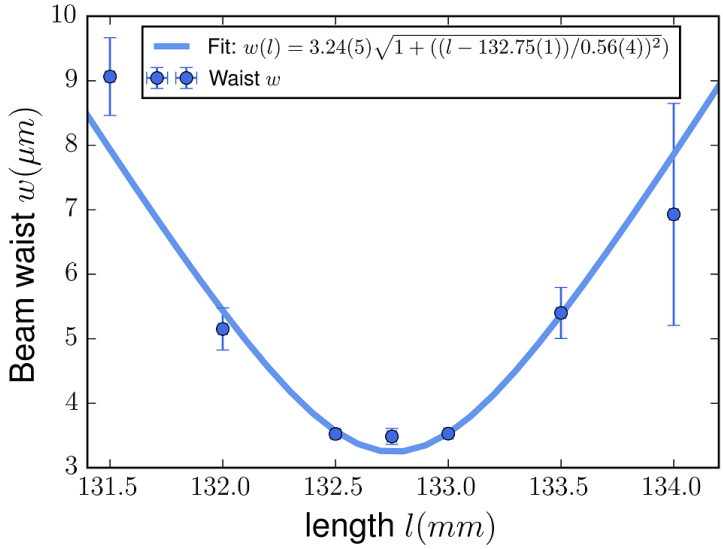

Figure 6.3: Beam profile along the propagation axis of the beam. The error of the beam waist correspond to the statistical error from the fit, and the error of the telescope length is the read-out error estimated to be $10\,\mu\mathrm{m}$.

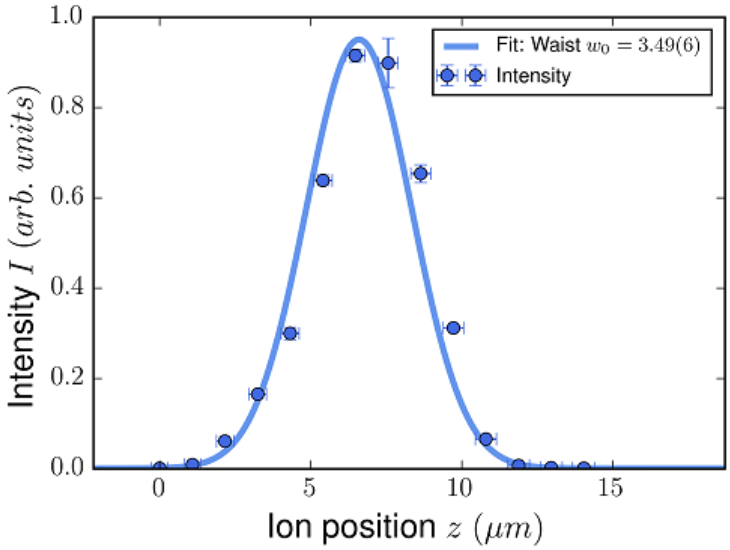

Figure 6.4: Intensity of the addressing beam along the trapping axis for a telescope length $l_0 = 132.75(1)\,\mathrm{mm}$. A fit of a Gaussian (Eq. 4.4) yields the beam waist $w_{0,\mathrm{exp}} = 3.49(6)\,\mu\mathrm{m}$.

However, it was impossible to achieve the smallest beam waist $w_{0,\mathrm{fit}} = 3.24(5)\,\mu\mathrm{m}$ extracted from the fit because as soon as the telescope length was set to $l_0 = 132.75(1)\,\mathrm{mm}$, the beam size decreased and an instability of the beam pointing was noticeable, since the Rabi oscillations became unstable as the value of the ion population fluctuated on the order of 20% over one minute for a given $729\,\mathrm{nm}$ excitation length. This instability is also visible in the beam profile of the addressing beam, shown in Fig. 6.4, as a shift of the fit with respect to the data points. Additionally, the waist $w_{0,\mathrm{exp}} = 3.49(6)\,\mu\mathrm{m}$ determined from the data in Fig. 6.4 does not correspond to the expected minimum waist $w_{0,\mathrm{fit}}$. Since the Rayleigh length $l_\mathrm{R} = 0.56(4)\,\mathrm{mm}$ is much longer than the amplitude of mechanical vibrations of the telescope, it is not possible that these fluctuations are caused by oscillations of the telescope length. Thus, we suspect that the instabilities of the Rabi oscillations are induced by intensity fluctuations resulting from mechanical vibrations of the objective.

We have observed that these oscillations do not occur for a shorter telescope length $l_1 = 132.50(1)\,\mathrm{mm}$, as there is no visible shift of the measured intensity profile, shown in Fig. 6.5, with respect to the fit. The waist $w_1 = 3.526(5)\,\mu\mathrm{m}$ at the slightly larger telescope length l_1 is indistinguishable within the error bars from the waist $w_{0,\mathrm{exp}} = 3.49(6)\,\mu\mathrm{m}$, and therefore, this telescope length is the one we have chosen for further measurements.

A simulation of the complete addressing path including the telescope and objective resulted that a telescope length of l_1 should lead to a beam waist of $w_z = 2.8\,\mu\mathrm{m}$ at the ion. However, already a change of $0.05\,\mathrm{mm}$ of the radius of the beam which is sent into the telescope leads to a change of $\Delta w = 0.5\,\mu\mathrm{m}$ of the beam waist inside the vacuum chamber. Since the simulation is assuming that the beam entering the telescope is perfectly collimated, I attribute the discrepancy between the results of the simulation and the experiment to an imperfect collimation of beam exiting the fiber.

The small errors of the retrieved waists are based on the assumptions that the beam is not aberrated and perfectly Gaussian, and thus, errors introduced by the deviations from this assumptions, which would increase the errors, are not taken into account in the error calculation. To conclude, this beam fulfills the important requirement of an addressing beam, namely, that the beam waist is smaller than the ion-ion distance $\delta z = 5.59(7)\,\mu\mathrm{m}$ [46].

6.2 Characterization of the cross-talk

While the first part this chapter focused on the characterization of the addressing beam with one ion, this section discusses the addressing properties using an ion crystal. For the purpose of characterizing these properties, we loaded two ions in the ion trap and addressed one of the ions with the new addressing beam. A sketch of this situation is shown in Fig. 6.6.

Due to the fact that the beam radius can be described by a Gaussian, as shown in Fig. 6.5, the electric field always has some amplitude even at large distances from the axis, so the beam not only affects the addressed ion, but also affects the unaddressed one. In this experimental situation, the addressed ion sits at $8.45(1)\,\mu\mathrm{m}$, which is the maximum of the intensity profile illustrated in Fig. 6.5, and the second ion is placed $5.59\,\mu\mathrm{m}$ away at $2.85(1)\,\mu\mathrm{m}$. The relative intensity $\Delta I = I_1/I_2$ between the intensity I_1 at ion 1 and the intensity I_2 at ion 2 is according to the Gaussian fit $\Delta I = 0.8\%$. A small intensity is sufficient to induce Rabi oscillations of the unaddressed ion. However, this cross-talk only maps the state of the unaddressed ion from

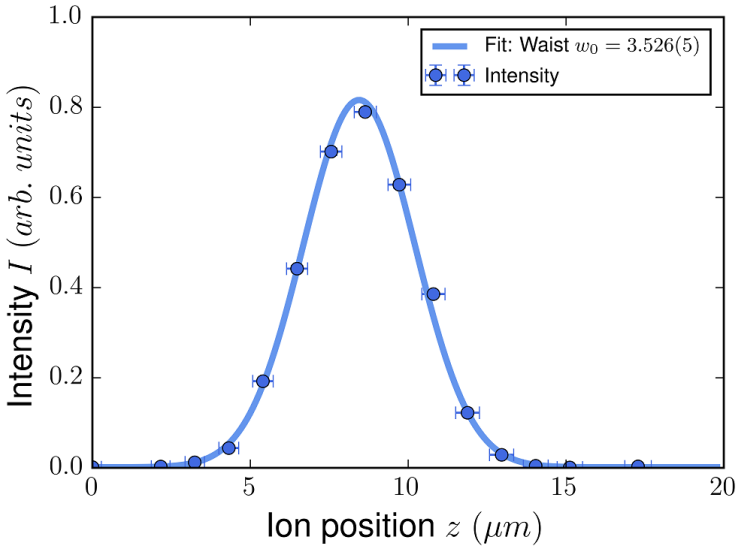

Figure 6.5: Intensity profile of the addressing beam for a telescope length $l = 132.50(1)\,\mathrm{mm}$. The position of the addressed ion is $43.56(5)\,\mu\mathrm{m}$ and the unaddressed ion sits at $37.96(5)\,\mu\mathrm{m}$.

$|4\mathrm{S}_{1/2}, m_J = -1/2\rangle$ into $|3\mathrm{D}_{5/2}, m_J = -1/2\rangle$ with a population close to one if the interaction time with the addressing beam is sufficiently long.

In order to measure the pulse length at which the metastable state population of the unaddressed ion reaches its maximum, the $|\mathrm{S}_{1/2}, m_J = -1/2\rangle \leftrightarrow |\mathrm{D}_{5/2}, m_J = -1/2\rangle$ transition is driven resonantly, and the experimental sequence is the one shown in Fig. 5.2. Detection is performed simultaneously with the PMT and the CCD camera, which allows us, as I will describe in Sec. 6.3, to compare both results with each other and ensures, if the measurements overlap well, that the detection is working properly.

The measurement result of populations of the metastable qubit state of the individual ions taken with camera detection is shown in Fig. 6.7. The population of the unaddressed ion reaches after a pulse length of $15.2\,\mu\mathrm{s}$ a population of $0.94(2)$. A fit of Eq. 5.10 yields the Rabi frequencies of the ions. The Rabi frequency of the addressed ion, $\Omega_2 = 1.766(8)\,\mathrm{MHz}$, and the Rabi frequency of the unaddressed ion, $\Omega_1 = 0.12(1)\,\mathrm{MHz}$, are used to calculate the addressing error

$$\epsilon_{\mathrm{res}} = \frac{\Omega_2}{\Omega_1} = 6.80(6)\% \tag{6.6}$$

as a figure of merit in the resonant driving condition.

For reducing the cross-talk, one can use the addressing beam in a composite pulse sequence, described in Ch. 7, in which the addressing beam excites the ion far detuned from the transition frequency. As a consequence, the cross-talk depends only on the relative intensity ΔI between the two ions rather than on $\sqrt{\Delta I}$. The addressing error for resonant driving yields a lower bound on the addressing error for the off-resonant drive and is estimated from 6.6 to be [54]

$$\epsilon_{\mathrm{off}} = \frac{\Omega_2^2}{\Omega_1^2} = 0.462(3)\%. \tag{6.7}$$

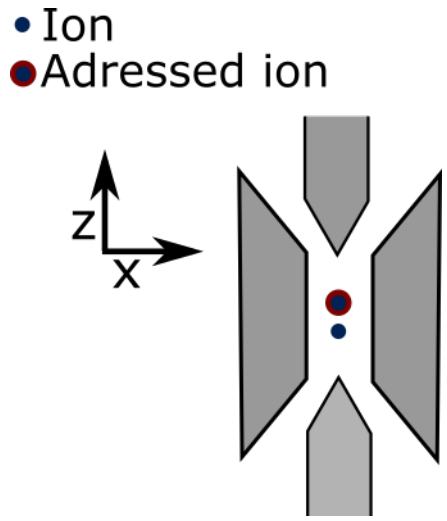

Figure 6.6: Schematic of the experimental situation. Two ions are trapped in the linear Paul trap, and one is addressed by the addressing beam. Ideally, the other ion should not be affected by the addressing beam.

In this case, the unaddressed ion ends up excited only after the addressed ion has undergone around 200 Rabi oscillations. This result could not measured directly because, even with ground state cooling, the coherence time of $1193(30)$ µs introduced in Sec. 3.5.2 would be too short to measure the off-resonant cross-talk.

One would expect that the relative intensity $\Delta I = 0.8\%$ calculated from the intensity profile depicted in Fig. 6.5 equals the off-resonant addressing error $\epsilon_{\text{off}} = 0.462(3)\%$. However, the measurements were performed on different days, and I attribute the discrepancy to the fact that the addressing beam was better optimized for the measurement of the cross-talk. This off-resonant driving is used in the following chapter (Ch. 7), when the addressing beam is used for a composite qubit flip [19].

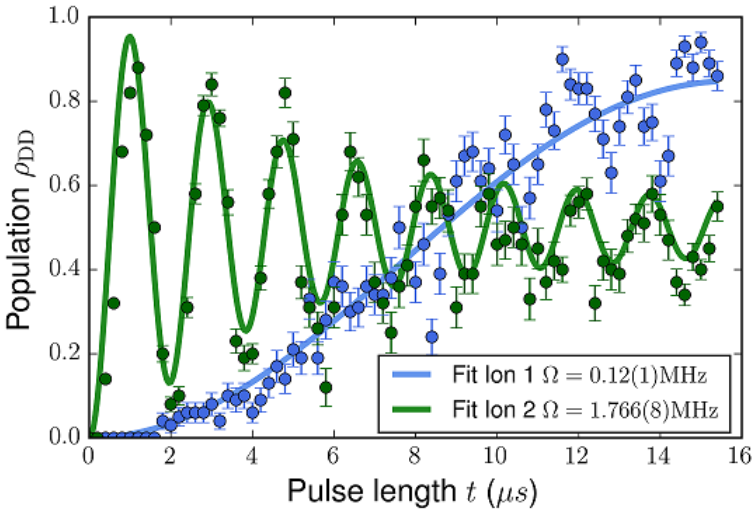

Figure 6.7: Population ρ_{DD} of each ion as a function of the pulse length t. The data is taken with the CCD camera, which allows us to measure the individual population of the excited qubit state of each ion. The error bars correspond to quantum projection noise [46]. A fit of Eq. 5.10 yields the Rabi frequency $\Omega_1 = 0.12(1)\,\mathrm{MHz}$ for the unaddressed and $\Omega_2 = 1.766\,\mathrm{MHz}$ for the addressed ion.

6.3 Comparison between the results of the PMT and CCD camera detection

As described in Sec. 3.4.2, the camera detection and the PMT detection routines measure the state of the ion independently of each other. In order to ensure that the detection methods were working properly for the measurement presented in Fig. 6.7, we use the measurements of the PMT as a reference for a comparison with the CCD camera measurements.

Such a comparison between the two detection methods is achieved by calculating the Pearson correlation coefficient according to [55]

$$r_{\mathrm{c,p}} = \frac{\sum_i (\rho_{i,\mathrm{c}} \cdot \rho_{i,\mathrm{p}})}{\sqrt{(\sum_i \rho_{i,\mathrm{c}}^2) \cdot (\sum_i \rho_{i,\mathrm{p}}^2)}}. \tag{6.8}$$

Here i is the index of the data points $\rho_{i,\mathrm{c}}$ and $\rho_{i,\mathrm{p}}$ taken with the CCD camera detection and the PMT detection. Additionally to the correlation coefficient, the overlap between the measurements is calculated according to [56]

$$\chi^2_{\mathrm{c,p}} = \frac{\sum_i (\rho_{i,\mathrm{c}} - \rho_{i,\mathrm{p}})^2}{\sigma_{\mathrm{p}}}, \tag{6.9}$$

with $\sigma_{\mathrm{p}} = \sqrt{\sum_i \rho_{i,\mathrm{p}}^2}$. These quantities are used as figures of merit to compare the measurements taken with the CCD camera to the measurements of the PMT. Optimally, the results should be identical, and therefore, $\chi^2_{\mathrm{c,p}}$ should be zero and $r_{\mathrm{c,p}}$ should be one.

States	Pearson correlation coefficient $r_{\mathrm{c,p}}$	$\chi^2_{\mathrm{c,p}}$
$\|SS\rangle$	0.999	0.002
$\|SD+DS\rangle$	0.9986	0.002
$\|DD\rangle$	0.9992	0.001

Table 6.1: Pearson correlation coefficient and $\chi^2_{\mathrm{c,p}}$ of the PMT and CCD camera detection for different states calculated according to Eq. 6.8 and 6.9.

Since the PMT cannot resolve the population of $|3\mathrm{D}_{5/2}\rangle$ of individual ions, the populations of the states $|S\rangle_1 \otimes |S\rangle_2 = |SS\rangle$, $|DD\rangle$ and $|SD+DS\rangle$ are calculated from the measurement presented in Fig. 6.7 as the first step for the comparison between the detection methods. The populations of $|SS\rangle$ and $|DD\rangle$ measured with both methods are pictured in Fig. 6.8, and a comparison between the populations of the superposition state $|SD+DS\rangle$ is shown in Fig. 6.9. The correlation coefficient and $\chi^2_{\mathrm{c,p}}$ are determined for these states and listed in Tab. 6.1. One can see that the correlation coefficient is on the order of 0.999, and the highest $\chi_{\mathrm{c,p}}$ is $\chi^2_{\mathrm{c,p}} = 0.002$ for all states, which leads us to conclude that the detection methods were self-consistent during the measurement of the resonant addressing error.

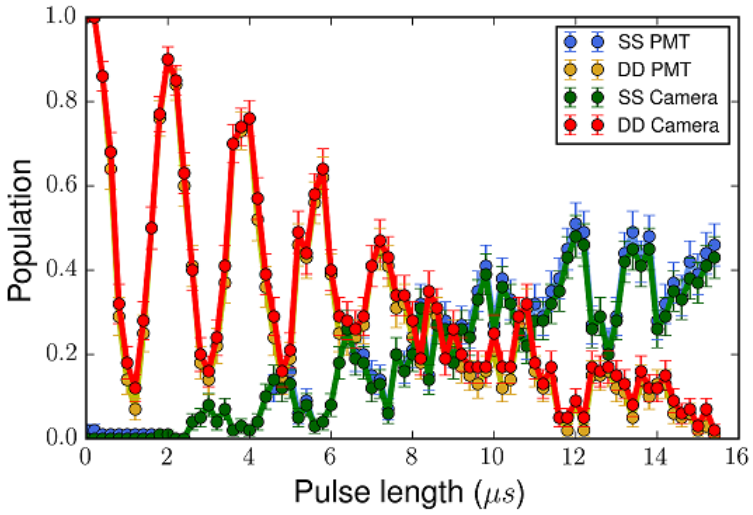

Figure 6.8: Comparison of the populations of the states $|SS\rangle$ and $|DD\rangle$ detected with the PMT and the CCD camera.

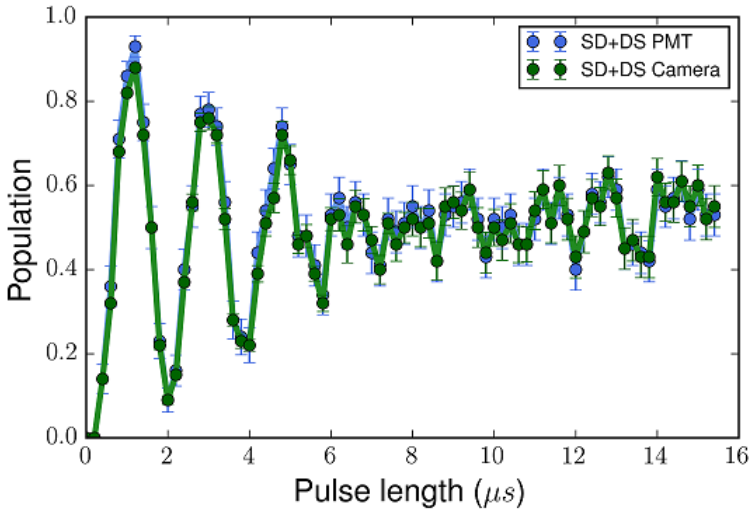

Figure 6.9: Comparison of the populations of the superposition state $|SD+DS\rangle$ detected with the PMT and the CCD camera.

6.4 Comparison of the new and the old addressing beams

The two-ion network protocols that were previously implemented using this experimental setup [19] already required an addressing beam. This addressing beam was set up before this master's thesis project in the framework of Diana Habicher's diploma thesis. In addition to the characterization of the addressing beam presented in the previous two sections, it is interesting to compare the beam's properties to those of the old addressing system.

A schematic of the old addressing setup is shown in Fig. 6.10. A fiber collimator expanded the beam to a waist diameter of $1.5\,\mathrm{cm}$ [19], and the beam was subsequently focused by an objective with a numerical aperture $NA \approx 0.11$ [16]. The collimator and the objective were mounted on the same motorized stage that is now used for the north-west global beam (Sec. 3.3.2). The whole addressing system was placed on a mount that is fixed to the vacuum chamber.

A similar measurement of the beam profile to the one described in Sec. 6.1 was performed in Ref. [19], and the result is shown in Fig. 6.11. The beam radius along the trapping direction is $w_{\mathrm{old}} = 10(1)\,\mu\mathrm{m}$, which is 2.9 times larger than the waist $w_1 = 3.526(5)\,\mu\mathrm{m}$ of the new addressing beam.

As a consequence of the large beam radius, the old addressing beam was used in a configuration where the addressed ion was positioned on the slope of the addressing beam. The disadvantage of this workaround is that it restricts us to network protocols which involve only two ions. In this configuration, it is not possible to perform experiments with three ions in which, for example, the central ion should be addressed. For such experiments, one needs to minimize the cross-talk on both neighboring ions, and thus, the central ion should be positioned at the maximum of the addressing beam. However, in this situation, the addressing error would be large for the old addressing beam because the relative intensity between the addressed and unaddressed ions is $\Delta I_{\mathrm{old}} \approx 63\%$. In contrast, the new addressing beam is designed to work

in this configuration, which is shown in Fig. 6.5, because the relative intensity of $\Delta I \approx 0.8\%$ is significantly lower with respect to ΔI_{old}. Thus, the new addressing beam enables individual ion addressing in a crystal that contains more than two ions.

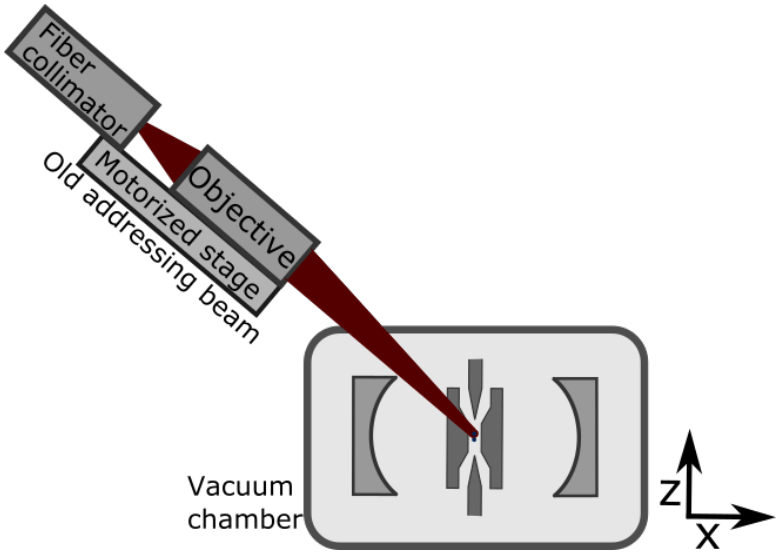

Figure 6.10: Setup of the old addressing beam. A fiber collimator expands a beam to a waist diameter of $1.5\,\mathrm{cm}$. Afterwards, the beam is focused by an objective with an numerical aperture of $NA \approx 0.11$. Both are placed on a motorized stage that allow movement in three directions.

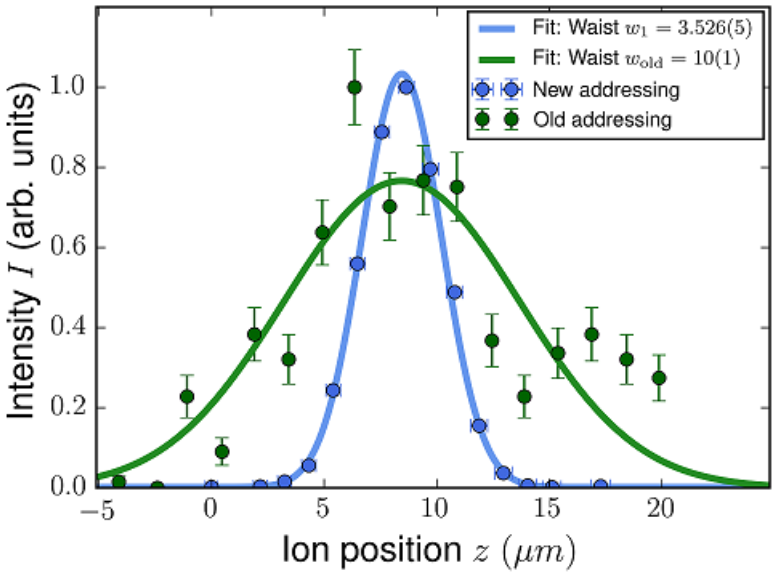

Figure 6.11: Measurement of the beam profile, performed by moving the old addressing beam with the motorized stage along the z axis indicated in Fig. 6.10. The Gaussian fit yields a $1/e^2$ beam radius $w_{\mathrm{old}} = 10(1)\,\mu\mathrm{m}$. In order to compare the old addressing system with the new one, the measurements from Fig. 6.5 are also shown. The green data points were measured by Bernardo Casabone, and more information on this measurement can be found in Ref. [19].

6.5 Conclusion

This chapter discussed the characterization of the single-ion addressing beam. The waist radius $w_1 = 3.526(5)\,\mu\mathrm{m}$ of the addressing beam along the axial direction was measured by moving the ions along the axial direction of the ion trap and using the tool developed in Sec. 5.1 to retrieve the Rabi frequency. Afterwards, the resonant addressing error $\epsilon_{\mathrm{res}} = 6.80(6)\%$ was measured and yielded an off-resonant addressing error of $\epsilon_{\mathrm{off}} = 0.462(3)\%$. A comparison with the beam radius of the old addressing beam $w_{\mathrm{old}} = 10(1)\,\mu\mathrm{m}$ shows that the waist of the new addressing beam is 2.9 times smaller. While the previous single-ion addressing beam could not be used to perform individual addressing in an ion crystal with more than two ions, the new addressing beam, in contrast, opens the gateway for quantum network experiments with individual ion-manipulation for more than two ions.

Furthermore, the addressing beam can be improved in the future by exchanging the mount of the objective for a more stable one. At the moment, the mechanical jitter of the objective prevents us from setting the telescope length to $l_0 = 132.75(1)\,\mathrm{mm}$, and consequently, it is impossible to locate the beam waist $w_{0,\mathrm{fit}} = 3.24(5)\,\mu\mathrm{m}$ at the ion position. If the beam were more mechanically stable, one could also increase the size of the beam which is sent into the objective, and thus, the resulting focused beam would be smaller, and consequently, the cross-talk would be reduced. However, one should keep in mind that aberrations of the addressing beam would play a stronger role if the size of the beam sent into the objective were to increase.

Chapter 7

Implementation of the z gate

The z gate is a quantum gate which is used to coherently rotate the state of an ion around the z axis. Together with the y rotation, the z gate enables us to reach any arbitrary state on the Bloch sphere [46]. This chapter starts with an explanation of the z gate and a description of a composite pulse sequence called the composite qubit flip. This pulse sequence uses the z gate and two rotations around the y axis to transfer the state of a particular ion in an two-ion crystal from $|S\rangle$ to $|D\rangle$. Afterwards, the experimental implementation of the composite qubit flip is presented, and its performance is analyzed. The measurement is then retaken with a new global beam, and the result is compared to previous results from Ref. [19].

7.1 Principle of the z gate

In the case of a two ion crystal where the ions are in the state

$$|\psi\rangle = |S\rangle_1 \otimes |S\rangle_2 = |SS\rangle,$$

one can, for example, generate the rotation

$$|SS\rangle \xrightarrow{\pi} |DS\rangle \tag{7.1}$$

of the state of one ion by applying a resonant π pulse with the addressing beam on the second ion. However, the disadvantage of this method is the cross-talk of the addressing beam in resonant configuration, which excites the unaddressed ion. Nevertheless, it is possible by using a composite pulse sequence to generate the same output state as Eq. 7.1 while reducing the addressing error and also preserving phase coherence with other laser beams. The essence of this so-called composite qubit flip is a phase shift induced by addressed off-resonant light.

First, a global $\pi/2$ rotation around the y axis of the Bloch sphere (Fig. 7.2a) is applied to the state of the ions and produces

$$|SS\rangle \xrightarrow{\frac{\pi}{2}} \frac{1}{\sqrt{2}}\big(|S+D\rangle \otimes |S+D\rangle\big). \tag{7.2}$$

Next, the addressing beam illuminates one ion with far off-resonant light as shown in Fig. 7.1. The detuning Δ of the laser frequency ω_{L} from the carrier transition frequencies has to fulfill the condition

$$\Delta \gg \Omega, \tag{7.3}$$

where Ω denotes the Rabi frequency when the transition is excited resonantly. Driving a transition far off resonance does not transfer population between the two states, but it induces shifts δ_{S} and δ_{D} of the energy levels due to the AC-Stark effect. This addressed AC-Stark effect leads to phase shifts of the state of the addressed ion, and consequently, rotates the state around the z axis. Therefore, this part of the composite pulse sequence is called the z gate or z rotation.
In the case of a superposition, off resonant driving for a time t of particular one ion transforms the state to [57]

$$\frac{1}{\sqrt{2}}\big(|S+D\rangle_1 \otimes |S+D\rangle_2\big) \xrightarrow{\text{AC-Stark pulse}} \frac{1}{2}\big(|S+D\rangle_1 \otimes \big(\mathrm{e}^{-it\delta_{\mathrm{S}}}|S\rangle_2 + \mathrm{e}^{-it\delta_{\mathrm{D}}}|D\rangle_2\big)\big). \quad (7.4)$$

As illustrated in Fig. 7.2b, the addressed ion acquires a phase

$$\Delta\phi = \delta_{\mathrm{D}}t - \delta_{\mathrm{S}}t \quad (7.5)$$

during the time t of the AC-Stark shift pulse. As shown in Fig. 7.2c, a second global $\pi/2$ pulse with the same phase as the first $\pi/2$ pulse is applied to both ions. Thus, the state can be expressed as [57]

$$|\psi\rangle = |D\rangle_1 \otimes \frac{1}{2}\mathrm{e}^{-i\delta_{\mathrm{S}}t}\left(\left(1-\mathrm{e}^{-i\Delta\phi}\right)|S\rangle_2 + \left(1+\mathrm{e}^{-it\Delta\phi}\right)|D\rangle_2\right) \quad (7.6)$$

Therefore, the probability

$$P_{\mathrm{DS}} = |\langle DS|\psi\rangle|^2 = \frac{1}{2}(1-\cos(\Delta\phi)) \quad (7.7)$$

to find the ions in the state $|DS\rangle$ is maximal for a phase shift of $\Delta\phi = \pi$. As a result (Fig. 7.2d), the state of only one ion is coherently transferred from $|S\rangle$ to $|D\rangle$ without affecting the other ion.

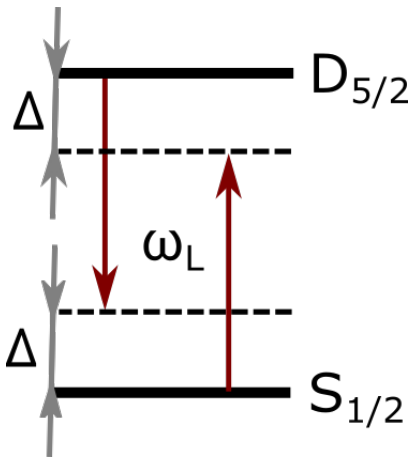

Figure 7.1: Simplified two-level system of the $^{40}\mathrm{Ca}^+$ ion in a superposition state. The qubit is driven off-resonantly with a laser of frequency ω_{L} that is detuned by Δ from the transition frequency.

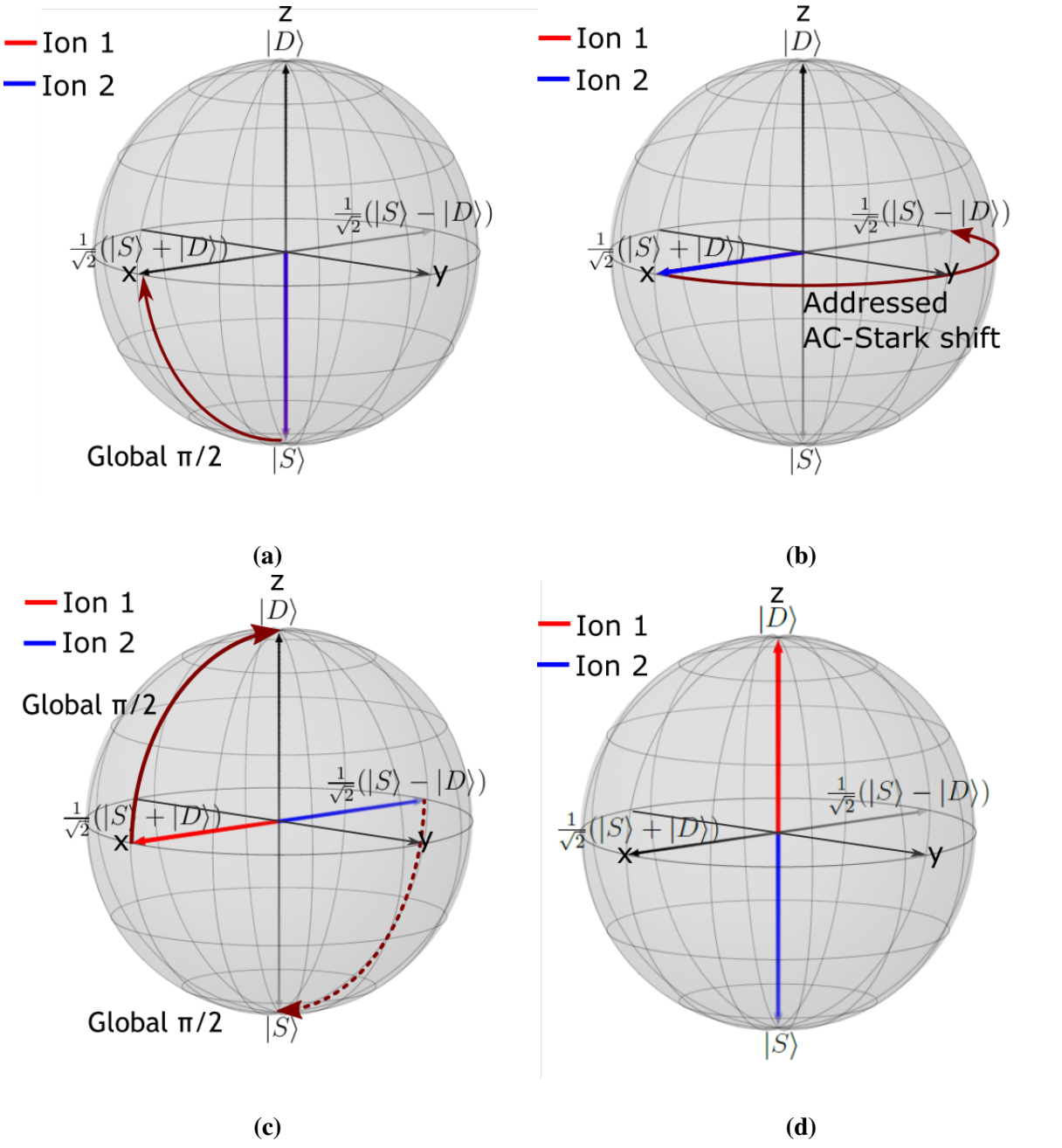

Figure 7.2: a) Illustration of the composite qubit flip. The states of the ions are represented by red and blue arrows. The state $|SS\rangle$ of the ions is rotated by $\pi/2$ around the y axis, as indicated by a dark red arrow. b) As a result of the first part of the composite qubit flip presented in a), both ions are in the superposition state $|S + D\rangle$. A z gate indicated by a dark red arrow is performed in which one ion is addressed by an off-resonant beam and the state is rotated around the z axis. c) The state vectors of two ions are opposing each other in the equatorial plane. A global rotation around the y axis rotates the states to $|D\rangle_1$ and $|S\rangle_2$. The dark red arrow indicates the rotation for the first ion, and the dashed arrow indicates the rotation for the second ion. d) Result of the composite qubit flip. One ion is prepared in $|S\rangle$ and the other one in $|D\rangle$.

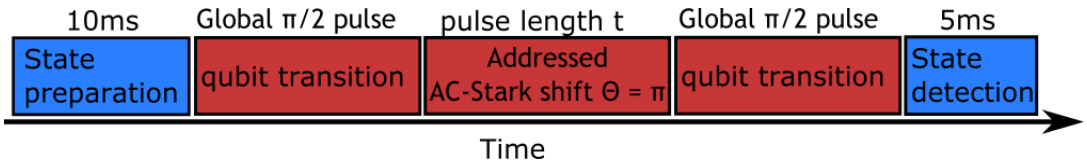

Figure 7.3: The experimental sequence of the composite qubit flip starts with $10\,\mathrm{ms}$ of state preparation, including Doppler cooling, sideband cooling and optical pumping, followed by a global $\pi/2$ pulse on the qubit transition. Afterwards, the single-ion addressing beam drives one ion off-resonantly for a pulse length t. Subsequently, another global $\pi/2$ pulse on the qubit transition with a phase equal to the phase of the previous $\pi/2$ pulse excites both ions. The last experimental step is state detection, performed with the CCD camera and the PMT.

7.2 Performance with the symmetric circular global beam

A first implementation of the composite qubit flip with the new addressing beam was performed using the north-east global beam, explained in Sec. 3.3.2. The experimental sequence is illustrated in Fig. 7.3 and starts with a $10\,\mathrm{ms}$ state preparation step that includes Doppler cooling and sideband cooling of the axial center-of-mass mode and the stretch mode of the two-ion crystal [18]. Next, a global $\pi/2$ pulse excites the $|\mathrm{S}_{1/2}, m_J = -1/2\rangle \rightarrow |\mathrm{D}_{5/2}, m_J = -1/2\rangle$ transition. Then, the single-ion addressing beam, which is detuned by $\Delta = 20\,\mathrm{MHz}$ from the $|\mathrm{S}_{1/2}, m_J = -1/2\rangle \rightarrow |\mathrm{D}_{5/2}, m_J = -1/2\rangle$ transition, is switched on for a pulse length t on the second ion. Another global $\pi/2$ pulse with the same phase with respect to the previous $\pi/2$ pulse completes the coherent state manipulation and is followed by state detection with the CCD camera and the PMT.

Before we start any measurement, we optimize the couplings of the laser beams to the ions by adjusting the beam pointings, using the metastable state population of both ions for a fixed pulse length shorter than the length of a π pulse as a reference. A measurement of the excited metastable state population of each ion is shown as a function of the AC-Stark pulse length t in Fig. 7.4. One can see that for length $t = 11\,\mu\mathrm{s}$ of the AC-Stark shift pulse, the population ρ_1 of the unaddressed ion is maximal and the population ρ_2 of the addressed ion is minimal. The probability p_{ne} of the ions being in the state $|DS\rangle$ after the composite pulse sequence is determined to be $p_{\mathrm{ne}} = 93(3)\%$. However, there is still a 7% probability for the ions to be in another state, which we attribute to the asymmetric coupling of the ions to the global beam [19]. The global beam used for this measurement has a circular beam profile, depicted in Fig. 7.5, which made it hard to couple both ions equally to the beam [19]. As soon as the intensity of the beam differs for one of the two ions, the Rabi frequencies are different and it is not possible to fully excite both ions simultaneously.

To test this hypothesis, a measurement of the total metastable state population of two ions was performed. The result is shown in Fig. 7.6. One can see that, as a consequence of the different Rabi frequencies, the Rabi oscillations collapse after $40\,\mu\mathrm{s}$. The possibility that this collapse is due to motional heating and decoherence can be excluded, since the Rabi oscillations revive after $70\,\mu\mathrm{s}$ [18]. Another indication for the unequal coupling of the two ions is that the total excited state population in Fig. 7.6 never reaches $\rho_{\mathrm{DD}} = 1$, since the maximum is $\rho_{\pi,\mathrm{ne}} = 0.96(2)$. Thus, the asymmetric coupling is the major limiting factor for the composite qubit flip because the metastable state population of the unaddressed ion after a composite qubit

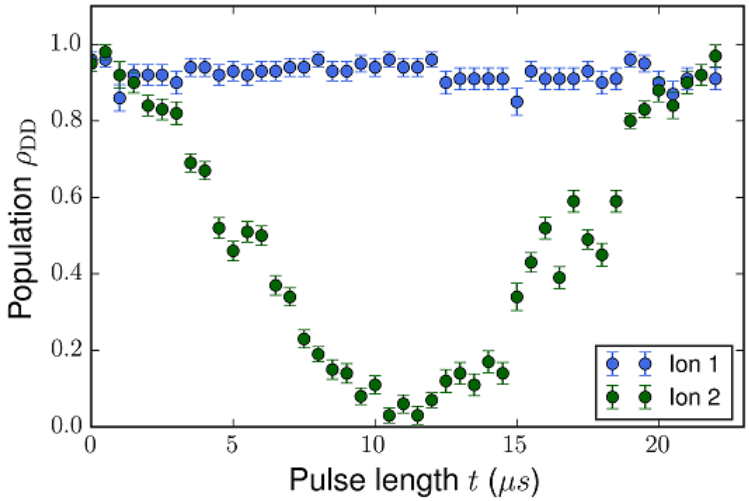

Figure 7.4: Metastable state population of each ion as a function of the pulse length of the AC-Stark pulse. One can see that the population of the addressed ion is minimal for a pulse length $t = 11\,\mu s$, while the population of the unaddressed ion is maximal.

flip cannot exceed the metastable state population after a single π pulse.

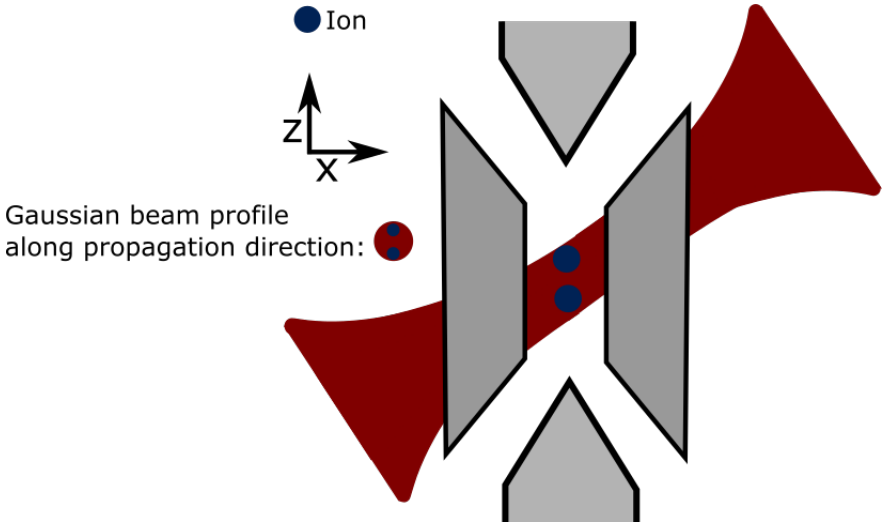

Figure 7.5: Illustration of the unequal coupling of the north-east global beam with two ions. The two ions are not equally coupled to the beam due to the circular beam profile along the propagation axis and the small beam size. The dimensions in this illustration are not to scale.

7.3 Performance with the new global beam

In the previous section, we have seen that the limiting factor for the composite qubit flip was the global $729\,\mathrm{nm}$ beam. Since the old addressing beam (Fig. 6.10) had become obsolete, we

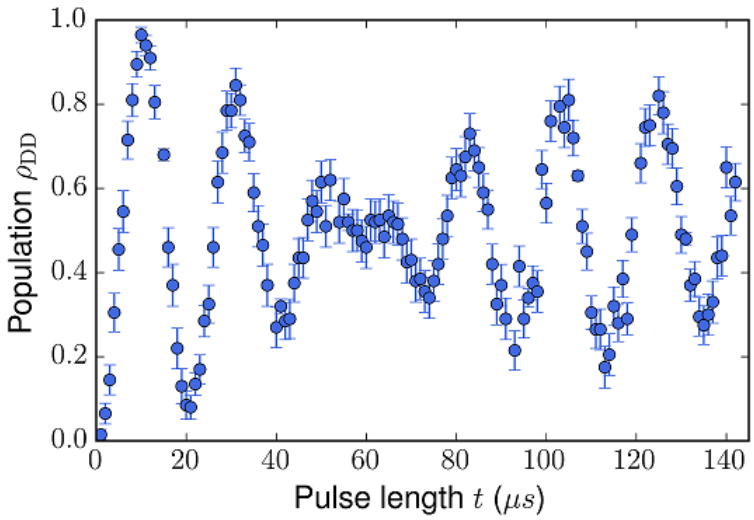

Figure 7.6: Total metastable state population of two ions as a function of the pulse length, measured with the PMT. One can see a collapse of the Rabi oscillations after $40\,\mu s$ and a revival after $70\,\mu s$.

decided to rebuild it as a new global beam. The first step was to take out the fiber collimator and replace it. The reason was that the fiber collimator in the old addressing path expanded the beam up to a $1.5\,\mathrm{cm}$ waist diameter [16]. Thus, the beam was tightly focused after the collimator by the objective, which would not be suitable for a new global beam. The replacement fiber collimator that we chose was used previously by the Linear Trap experiment and produces an elliptical beam shape due to a cylindrical lens. The beam has a waist diameter of approximately $1\,\mathrm{cm}$ along the vertical axis and $0.33\,\mathrm{cm}$ along the horizontal axis. Thus, the ratio of the vertical and horizontal beam diameters is 3:1.

The experimental setup is described in Sec. 3.3.2, and the experimental situation with the new global beam is illustrated in Fig. 7.7. Due to the elliptical beam shape and a larger beam diameter, the ions are coupled equally to the global beam. An additional advantage of the new global beam is the motorized stage that was previously used for the old addressing beam. The stage allows us to align the global beam precisely to the ion crystal. More details about the motorized stage and the old addressing beam can be found in Ref. [16].

With these new tools in the hand, a measurement of the metastable state population of each ion after coherent driving of a carrier transition was performed and is shown in Fig. 7.8. We conclude that both ions are equally coupled to the global beam due to the overlap of the individual metastable state populations, which is characterized by $\chi^2_{\mathrm{DD}} = 0.007$ according to Eq. 6.9. There is no visible dephasing between the two ions even at a pulse length of $50\,\mu s$. However, the maximum individual populations $\rho_{\pi,1} = 0.95(2)$ of the first ion and $\rho_{\pi,2} = 0.94(2)$ of the second ion are not optimal.

The fits of the populations according to the method described in Ch. 5 yield an effective phonon number of $n_{\mathrm{eff},1} = 0.106(7)$ of the first ion and $n_{\mathrm{eff},2} = 0.208(1)$ of the second ion. These phonon numbers are a factor of ten larger than the effective phonon number of $n_{\mathrm{eff,sb}} = 0.013(2)$ from the measurement of the effective phonon number of one sideband-cooled ion presented in Fig. 5.5. Although we do not expect to achieve the same cooling performance for

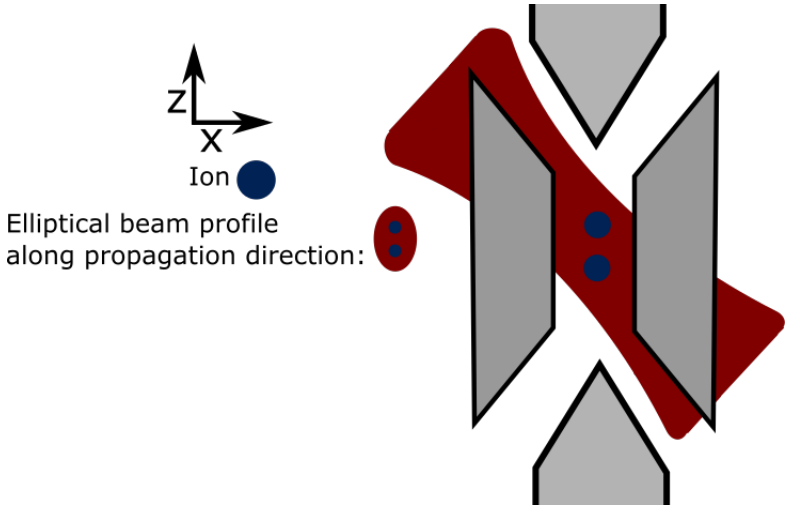

Figure 7.7: Schematic of the experimental situation with the improved global beam. The beam, which has an elliptical beam profile, couples equally to the ions.

a two-ion crystal as for one ion, the phonon numbers retrieved from the measurement shown in Fig. 7.8 are still higher than what we would expect. Therefore, I attribute the loss of population to the temperature of the ions which increased due to drifts of the beam pointings of the cooling beams.

The possibility that this missing population is due to detection problems can be excluded since the average $\chi^2_{\mathrm{c,p}}$ of the signals detected with the PMT and camera according to Eq. 6.9 is $\chi^2_{\mathrm{c,p}} = 0.003$.

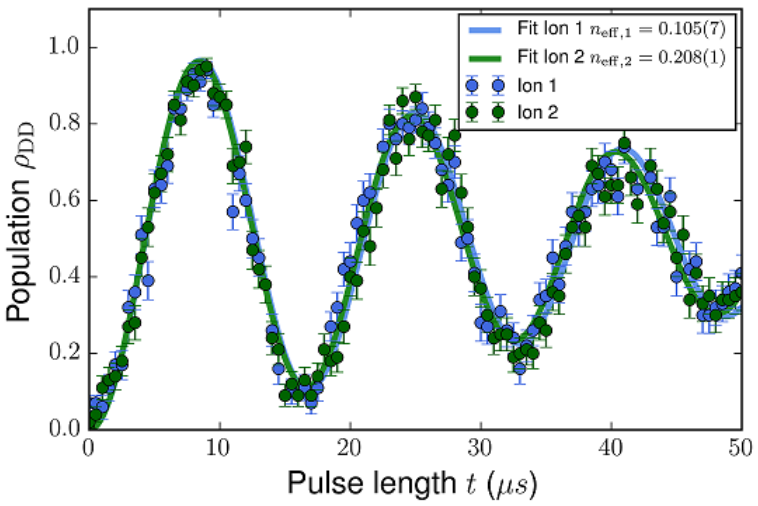

Figure 7.8: Populations of each ion of the metastable state as a function of the pulse length for coherent driving of the carrier transition. The populations overlap by $\chi_{\mathrm{DD}} = 0.004$, and there is no visible dephasing of the two ions.

Finally, after we optimized the sideband cooling and the coupling of the beams to the ions,

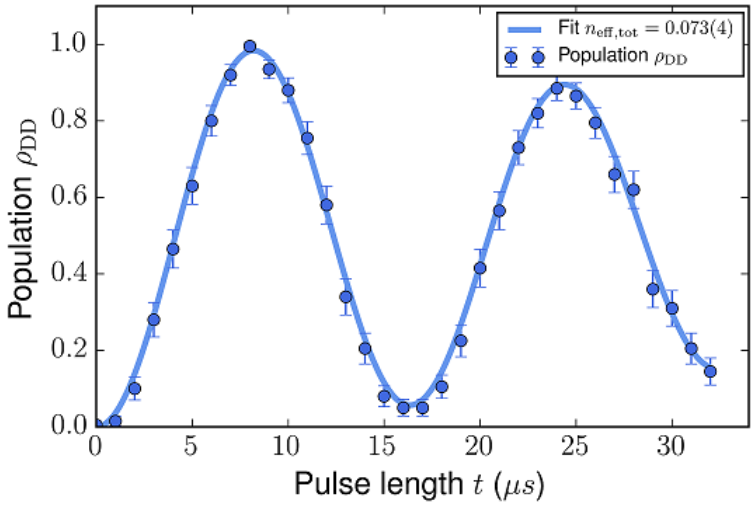

Figure 7.9: Rabi oscillations of a two-ion crystal measured with the PMT. In contrast to the measurement presented in Fig. 7.6, the population of the excited state reaches a maximum value of $\rho_{\mathrm{DD}} = 1.00(1)$ after $8\,\mu\mathrm{s}$. A fit according to Eq. 5.10 yields an effective phonon number $n_{\mathrm{eff,tot}} = 0.073(4)$.

we performed a measurement of Rabi oscillations (Fig. 7.9) which led to a total metastable state population of $\rho_{\pi,\mathrm{nw}} = 1.00(1)$ after a π pulse. This result is a significant improvement from the previous value $\rho_{\pi,\mathrm{ne}} = 0.96(2)$ presented in Sec. 7.2, for which the global beam with a circular beam profile was used. Moreover, a fit according to Eq. 5.10 yields an effective phonon number of $n_{\mathrm{eff,tot}} = 0.073(4)$ which is lower than the individual phonon numbers $n_{\mathrm{eff},1}$ and $n_{\mathrm{eff},2}$, retrieved from the measurements presented in Fig. 7.8.

After this significant improvement of the π pulse due to the new global beam was observed, the measurement of the composite qubit flip was repeated, and the metastable state population was measured as a function of the AC-Stark pulse length. The resulting individual populations of $|D\rangle$ of each ion are shown in Fig. 7.10, and the populations of $|SD\rangle + |DS\rangle$ measured using both the PMT detection and the CCD camera are compared in Fig. 7.11 according to the procedure presented in Sec. 6.3. After a time $t = 13.5\,\mu\mathrm{s}$, the probability of measuring the state $|DS\rangle$ is $p_{\mathrm{nw}} = 99(1)\%$, which represents an improvement on the previous measurement of $p_{\mathrm{ne}} = 93(3)\%$ presented in Sec. 7.2. The overlap of the populations of $|SD\rangle + |DS\rangle$ determined from the two measurement methods according to Eq. 6.9 is $\chi^2_{SDDS} = 0.002$.

7.4 Comparison with previous results

The probability of measuring the state $|SD\rangle$ after the composite qubit flip from $p_{\mathrm{ref}} = 91(4)\%$ from Ref. [19] is identical with $p_{\mathrm{ne}} = 93(3)\%$ (Fig. 7.4) that was measured with both improved cooling, which was optimized by using the strategy from Ch. 5, and the new addressing beam. By changing the old addressing beam to a new global beam with an elliptical beam shape, this probability increased to $p_{\mathrm{nw}} = 99(1)\%$, which is up to now the highest success probability of the composite qubit flip achieved in our experiments. Furthermore, not only was the composite qubit flip improved, but also the total metastable state population $\rho_\pi = 1.00(1)$ after a π pulse on

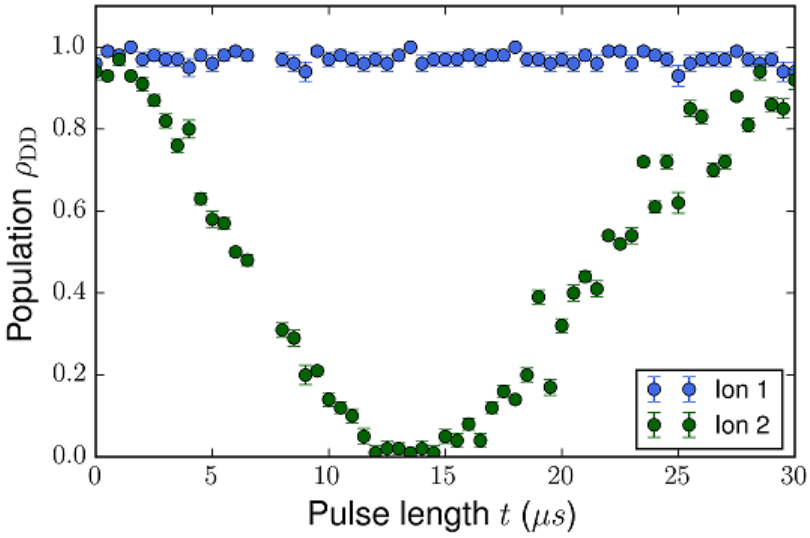

Figure 7.10: Measurement of the excitation probability as a function of the AC-Stark shift pulse length t. The experimental sequence, in which ion 2 is the addressed ion, is illustrated in Fig. 7.3. After a time $t = 13.5\,\mu s$, the probability $p_{nw} = 99(1)\%$ of measuring the state $|DS\rangle$ is maximal.

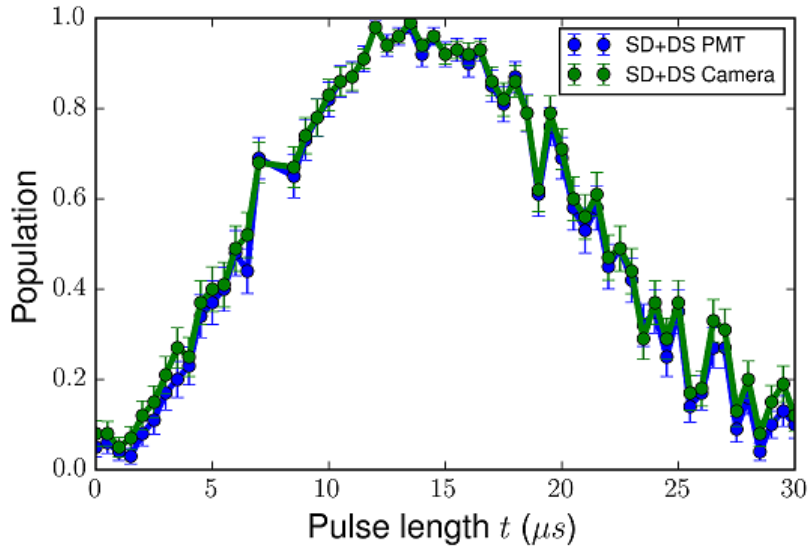

Figure 7.11: Comparison of the metastable state populations of the superposition $|SD\rangle + |DS\rangle$ detected with the PMT and the CCD camera. The value of χ^2_{SDDS} between these two curves is calculated according to Eq. 6.9 and is found to be $\chi^2_{SDDS} = 0.002$.

two ions is within the error bars indistinguishable from the previous result $\rho_{\pi,\mathrm{ref}} = 0.99(1)$ [19], obtained in our experiments. In order to increase the number of significant figures on such a measurement, one could increase the number of measurement cycles which would lead to a decrease of the error introduced by the quantum projection noise.

7.5 Conclusion

In this chapter, we have seen how the z gate was implemented by using the addressing beam, which was described in Sec. 3.3.3 and characterized in Ch. 6. The first implementation of the composite qubit flip, which involved the z gate, used the north-east global beam and yielded a probability of $p_{\mathrm{ne}} = 93(3)\%$ of measuring the state $|DS\rangle$ after a composite pulse sequence. After swapping to the new global beam that has replaced the old addressing beam [16], the total population of two ions after a π pulse improved significantly from $\rho_{\pi,\mathrm{ne}} = 0.96(2)$ to $\rho_{\pi,\mathrm{nw}} = 1.00(1)$. To summarize, the measurement probability of obtaining $|DS\rangle$ after the composite qubit flip improved by using the new global beam, and $p_{\mathrm{nw}} = 99(1)\%$ is by far the highest probability achieved in our experiments.

Due to the fact that the probability of $p_{\mathrm{nw}} = 99(1)\%$ is within the 1% error bar indistinguishable from 100%, an interesting next step in the future would be to analyze the z gate probability to more significant digits. One reason for the missing 1% could be the cross-talk $\epsilon_{\mathrm{off}} = 0.462(3)\%$ of the addressing beam in the off-resonant configuration. As recommended in Sec. 6.5, in the future, we could decrease the cross-talk by increasing the beam expansion of the telescope. Furthermore, intensity fluctuations as seen by the ion have not been characterized in this master's thesis research and should also be taken into account. Another major improvement that might lead to a higher probability could be a magnetic shield, which would minimize magnetic field fluctuations that lead to phase shifts of the superposition state after the first $\pi/2$ pulse.

Another important application of the rotation around the z axis is state tomography [46]. Since the addressing beam allows us to reach any point in the equatorial plane and the global beam rotates the qubit states around the y axis on the Bloch sphere, one can reach any point on the Bloch sphere via these operations. In conclusion, the state tomography would allow us to directly estimate the fidelity with which we can prepare a state with a quantum gate.

Chapter 8

Summary and outlook

The work presented in this master's thesis represents one major building block for future quantum network protocols which will be implemented in the first quantum network node at the University of Innsbruck. In the framework of my master's thesis research, a new addressing beam has been implemented at the existing quantum network node. The new addressing beam enables single-ion addressing with low cross-talk as well as high fidelity quantum gates based on composite pulses of a global beam and the addressed beam. Moreover, an additional global beam has been installed, which improved the performance of global qubit operations and composite pulse sequences.

The first step towards the new addressing beam and its applications was the characterization of the electro-optical deflector (EOD), which allows us to shift the addressing beam over a distance proportional to the applied voltage. An investigation of the polarization dependence found that as soon as the polarization was not fully horizontal, the beam was additionally deflected along the vertical direction. Furthermore, we investigated the linear dependence of the deflection angle on the applied voltage and found the maximal deflection angle to be $5.0(2)\,\mathrm{mrad}$ at a driving voltage of $2\,\mathrm{kV}$.

The next step towards the characterization of the new addressing beam was the development of a tool which enabled us to extract both the effective phonon number of the ion and the Rabi frequency from a measurement of Rabi oscillations. The procedure was applied to both a Doppler-cooled ion and a sideband-cooled ion, and the effective phonon number of $n_{\mathrm{eff,dopp}} = 0.10(1)$ of the Doppler-cooled ion was approximately a factor of ten larger than the effective phonon number of $n_{\mathrm{eff,sb}} = 0.013(2)$ of the sideband-cooled ion. Moreover, the extracted Rabi frequencies had a low statistical error of $\Delta\Omega = 0.2\%$, and therefore, the tool was useful for a precise characterization of the beam profile of the addressing beam.

The subsequent step in my master's thesis research was to set up the optical path of the new addressing beam. The key idea for the new addressing beam was to use the same objective which gathers the ion's fluorescence for focusing the addressing beam onto the ion. The most important requirement for the addressing beam was that the beam radius needed to be smaller than the ion-ion distance of $5.59\,\mu\mathrm{m}$. However, the path length from the objective to the CCD camera was too short, and as a consequence, the focus of the objective for $729\,\mathrm{nm}$ light was not at the position of the ions. The solution to this problem was to shorten the length of the telescope which expands the beam before it enters the objective, in order to adjust the position of the waist inside the vacuum chamber.

After we implemented the addressing beam, we characterized it by measuring the beam size for different telescope lengths. According to a fit of Eq. 6.5, the minimum theoretically achievable waist radius was found to be $w_{0,\mathrm{fit}} = 3.24(5)\,\mu\mathrm{m}$ at a telescope length of $l_0 = 132.75(1)\,\mathrm{mm}$. The measured waist of $w_{0,\mathrm{exp}} = 3.49(6)\,\mu\mathrm{m}$ was larger than $w_{0,\mathrm{fit}}$ due to mechanical instabilities of the objective, but even if this waist does not correspond to the smallest achievable waist, it still fulfills the requirement of being smaller than the ion-ion distance.

The next step in the characterization of the addressing beam was the measurement of the addressing error, which yielded an addressing error of $\epsilon_{\mathrm{res}} = 6.80(6)\%$ in the resonant configuration and a cross-talk $\epsilon_{\mathrm{off}} = 0.462(3)\%$ in the off-resonant configuration, which is the configuration in which the beam will mainly be used.

The final goal of this master's thesis research was the implementation of the composite qubit flip, including a z gate, in a two-ion crystal. The first implementation was carried out using the north-east global beam (Sec. 3.3.2) and yielded a probability of $p_{\mathrm{ne}} = 93(3)\%$ of measuring the state $|DS\rangle$ after the gate operation. Subsequently, a measurement of the total excitation of two ions was performed and showed that the Rabi oscillations of the total excitation were collapsing due to dephasing of the two ions after the fourth Rabi flop. In order to couple both ions equally to the drive field, a new global beam with an elliptical beam profile has been implemented, and the metastable state population of both ions after a π pulse increased from $\rho_{\pi,\mathrm{ne}} = 0.96(2)$ to $\rho_{\pi,\mathrm{nw}} = 1.00(1)$. Finally, the measurement of the composite qubit flip was repeated, and we found a probability of $p_{\mathrm{nw}} = 99(1)\%$ of measuring the state $|DS\rangle$ after the gate.

So far, this chapter summarized has concepts and results presented in this master's thesis. Now, I want to present as an outlook a quantum network protocol which directly takes advantage of the improvements made during my master's thesis research. This network protocol is interesting for our network node because in the future, as mentioned in Ch. 1, our network node will be the central node of a three-node quantum network, and this so-called entanglement routing via addressed Raman transitions would enable us to choose which ion of a two-ion crystal located at our node is entangled with which distant ion, trapped in one of the other nodes.

For implementing the entanglement routing, it is necessary to coupled two ions to the high-finesse cavity, and to entangle each ion sequentially with a photon [12]. The first step is exciting one ion into $|D\rangle$ by performing a composite qubit flip. Next, the ion which stayed in $|S\rangle$ will be entangled with the polarization of a photon by performing a bichromatic Raman transition [12]. Finally, the second ion will be brought into the ground state by a π pulse, and an additional bichromatic Raman transition will be performed with this ion.

It has been shown that the fidelity of performing the ion-photon entanglement twice is $F_{\mathrm{IP}}^2 \geqslant 94.9(3)\%$ [12]. This value highlights the importance of the implementation of the composite qubit flip with a high success probability, since an estimate of the fidelity $F_{\mathrm{ent,ne}} \geqslant F_{\mathrm{IP}}^2 \cdot \rho_{\pi,\mathrm{ne}} \cdot p_{\mathrm{ref}} = 83(4)\%$ for the entanglement routing based on our previous resources is limited by the past success probability of $p_{\mathrm{ref}} = 91(4)\%$ of the composite qubit flip. With the improvements made for the composite qubit flip and the π pulse, one can expect a fidelity of $F_{\mathrm{ent,nw}} = F_{\mathrm{IP}}^2 \cdot \rho_{\pi,\mathrm{nw}} \cdot p_{\mathrm{nw}} = 94(1)\%$ for the full experiment.

Since for more complex quantum network protocols, more quantum gates are necessary, it becomes increasingly important that each quantum gate has the highest fidelity possible. The improvements made with the implementation of the composite qubit flip are the first step towards more complicated quantum network protocols that require high-fidelity quantum gates as building blocks.

Appendix A

Python codes for the characterization of the EOD

A.1 Python code for the analysis of the polarization dependency

```
import glob
import os
import numpy as np
from pylab import imshow
from scipy.optimize import curve_fit
import matplotlib.pyplot as plt
#Definition of the two functions that are fitted (standard gaussian)
def func(x, a, x0, sigma,y0):
    return a*np.exp(-(x-x0)**2/(2*sigma**2))+y0

#generate list of all the files that should be read in
names = []
os.chdir("A:\Dokumente\Daten Masterarbeit\markus\Data\DatenEOD\EOD_deflection_Aktuell\Polarization")
for file in glob.glob("EOD_0.*csv"):
    names.append(file)


#create all the arrays
degree = np.zeros(len(names)/2)
xdistance = np.zeros(len(names)/2)
xdistanceerr = np.zeros(len(names)/2)
ydistance = np.zeros(len(names)/2)
ydistanceerr = np.zeros(len(names)/2)
ppmm = 0.0044 #pixel per mm on the beam profiler
i = 0
j=0

while i !=len(names):
    #read out the angle from the filename
    first_index = names[i].index('.')+1
    second_index = names[i][first_index:].index('_')+first_index
    degree[j] = float(names[i][first_index:second_index])

    #readout the shifed picture
    shifted = np.genfromtxt(names[i],delimiter=';',skip_header = 5, skip_footer = 1)
    shifted[0,0]=0 #replace NaN with 0
    #sum over x or y axis
    shiftedx = np.sum(shifted,axis = 0)
    shiftedy = np.sum(shifted,axis = 1)
    #open calibration picture
    cali = np.genfromtxt(names[i+1],delimiter=';',skip_header = 5, skip_footer = 1)
    cali[0,0] = 0

    calix = np.sum(cali,axis = 0)
    calix = calix/np.max(calix)
    caliy = np.sum(cali,axis = 1)
    xaxis = np.array(cali[0,:])
    yaxis = np.array(cali[:,0])
    #perform the fitsfor the center in x and y direction
    p0x = [np.amax(calix),np.shape(calix)[0]/2,np.shape(calix)[0]/5,0]
    p0y = [np.amax(caliy),np.shape(caliy)[0]/2,np.shape(caliy)[0]/5,0]
    poptcalix, pcovcalix = curve_fit(func, xaxis, calix,p0x)
```

```
    poptcaliy, pcovcaliy = curve_fit(func, yaxis, caliy,p0y)

    #
    poptshiftedx,pcovshiftedx = curve_fit(func, xaxis, shiftedx,p0x)
    poptshiftedy,pcovshiftedy = curve_fit(func, yaxis, shiftedy,p0y)
    xccali = poptcalix[1]
    xcalicerr = np.sqrt(pcovcalix[1,1])
    yccali = poptcaliy[1]
    yccalierr = np.sqrt(pcovcaliy[1,1])
    xcshifted = poptshiftedx[1]
    xcshiftederr = np.sqrt(pcovshiftedx[1,1])
    ycshifted = poptshiftedy[1]
    ycshiftederr = np.sqrt(pcovshiftedy[1,1])
    xdistance[j] = np.abs(xcshifted-xccali)*ppmm
    xdistanceerr[j] = np.sqrt(xcshiftederr**2 + xcalicerr**2)*ppmm
    ydistance[j] = np.abs(ycshifted-yccali)*ppmm
    ydistanceerr[j] = np.sqrt(ycshiftederr**2 + yccalierr**2)*ppmm

    i = i+2
    j = j+1
#plot the beam in 2D
fig3 = plt.figure()
imshow(cali)
plt.xlabel(r"Pixel␣number␣x-direction␣(px)",size = 16)
plt.ylabel(r"Pixel␣number␣y-direction␣(px)",size = 16)
plt.xticks(size = 15,weight = 'bold')
plt.yticks(size=15,weight='bold')
plt.savefig("picture_beam.png", dpi = 500)

#plot the gaussian fit in x-direction
fig = plt.figure()
plt.rc('font', weight='bold', size = 10.5)
ax = fig.add_subplot(111)
plt.rc('text', usetex=True)
plt.errorbar(xaxis, calix ,label= r'Brightness␣in␣x-direction')
plt.plot(xaxis,func(xaxis,poptcalix[0],poptcalix[1],poptcalix[2],poptcalix[3]),
label = r'Gaussian␣fit',linewidth=2)

plt.xlabel(r"Pixel␣number␣(px)",size = 16)
plt.ylabel(r"Normalized␣brightness",size = 16)
plt.legend(bbox_to_anchor=(0.57, 0.995))
#plt.xlim(-10, 340)
#plt.ylim(0,1)
plt.xticks(size = 15,weight = 'bold')
plt.yticks(size=15,weight='bold')
#plt.savefig("gaussian.png", dpi = 500)
#plt.plot(xaxis,func(xaxis,poptcalix[0],poptcal


#plot deflection vs angle of the wave-plate

fig2 = plt.figure()
plt.rc('font', weight='bold', size = 10.5)
ax = fig.add_subplot(111)
plt.rc('text', usetex=True)

plt.errorbar(degree, xdistance, xerr=2, yerr= xdistanceerr,fmt = 'o',
label = r'Deflection␣in␣x-direction')
plt.errorbar(degree, ydistance, xerr = 2, yerr = ydistanceerr, fmt = 'o',
 label= r'Deflection␣in␣y-direction')
plt.xlabel(r"Angle␣of␣half-wave␣plate␣($^\circ$)",size = 16)
plt.ylabel(r"Deflection␣(mm)",size = 16)
plt.legend(bbox_to_anchor=(0.57, 0.995))
plt.xlim(-10, 340)
plt.ylim(0,1)
plt.xticks(np.arange(0,400,50),size = 15,weight = 'bold')
plt.yticks(size=15,weight='bold')
#plt.savefig("polarization.png", dpi = 1000)
#plt.plot(xaxis,func(xaxis,poptcalix[0],poptcalix[1],poptcalix[2],poptcalix[3]))
```

A.2 Python code for the analysis of the deflection angle vs. voltage

```
import glob
import os
import numpy as np
import scipy
from pylab import imshow
from scipy.optimize import curve_fit
import matplotlib.pyplot as plt
#Definition of the two functions that are fitted (standard gaussian and linear fit)
def func(x, a, x0, sigma,y0):
    return a*np.exp(-(x-x0)**2/(2*sigma**2))+y0

def lin(x,a,y0):
    return a*x+y0
```

```
#reads all the CSV files with positive voltage and writes it in a list
os.chdir('A:\Dokumente\Daten Masterarbeit\markus\Data\DatenEOD\EOD_deflection_Aktuell')
liste = []
names = []
for file in glob.glob("EOD*.csv"):
    liste.append(np.genfromtxt(file,delimiter=';',skip_header = 5, skip_footer = 1))
    names.append(file)
numberoffiles = len(liste)

#Introduction of all necessary variables
cali = liste[0]
xaxis  = np.zeros(np.shape(cali)[1])
yaxis = np.zeros(np.shape(cali)[0])
calix  = np.zeros(np.shape(cali)[1])
caliy = np.zeros(np.shape(cali)[0])
voltage = np.zeros(np.shape(liste)[0]+numberoffiles)
voltageerr = np.zeros(np.shape(liste)[0]+numberoffiles)
xc = np.zeros(np.shape(liste)[0]) #xcoordinate of beam center
yc = np.zeros(np.shape(liste)[0]) #ycoordinate of beam center
xcerr = np.zeros(np.shape(liste)[0]) # error of xcoordinate of beam center
ycerr = np.zeros(np.shape(liste)[0]) #error of y coordinate of beam center
diffxerr= np.zeros(np.shape(liste)[0]) #error of difference between
#xcoordinate and xcoordinate of calibration beam
diffyerr= np.zeros(np.shape(liste)[0]) #error of difference between
#ycoordinate and ycoordinate of calibration beam
diffx= np.zeros(np.shape(liste)[0]) # difference between xcoordinate
 #of center of beam and x of center of calibration beam
diffy= np.zeros(np.shape(liste)[0]) # difference between ycoordinate of
# center of beam and y of center of calibration beam
distance= np.zeros(np.shape(liste)[0]+numberoffiles) # absolute distance in mm
distanceerr= np.zeros(np.shape(liste)[0]+numberoffiles) # error of absolute distance in mm
angle= np.zeros(np.shape(liste)[0]+numberoffiles) #angle in mrad
angleerr= np.zeros(np.shape(liste)[0]+numberoffiles) # error of angle in mrad
#Known parameters from the measurements,
realdistance = 560 #distance EOD to beam profiler in mm
voltagecali  = 98.29 #calibration of the voltage 1V of monitor output = 98.29V
#on high voltage amplifier
ppmm = 0.0044 #pixel per mm on the beam profiler
realdistanceerr = 10

#get 1D data out of 2D pictures, here it is just the calibration picture of the 0V beam
cali[0,0] = 0
xaxis = np.array(cali[0,:])
yaxis = np.array(cali[:,0])

calix = np.sum(cali,axis = 0)
caliy = np.sum(cali,axis = 1)

p0x = [np.amax(calix),np.shape(calix)[0]/2,np.shape(calix)[0]/5,0]
p0y = [np.amax(caliy),np.shape(caliy)[0]/2,np.shape(caliy)[0]/5,0]
#performs the fit of the x data
popt, pcov = curve_fit(func, xaxis, calix,p0x)
xccali = popt[1]
xc[0] = xccali
xccalierror =  xcerr[0] = np.sqrt(pcov[1,1])
#performs fit of y data
popt, pcov = curve_fit(func, yaxis, caliy,p0y)
yccali = popt[1]
yc[0]  = yccali
yccalierror = ycerr[0]=np.sqrt(pcov[1,1])

#performs all the fits of all the csv files and calculates the distance in mm and in angle (mrad)
for k in range(1,np.shape(liste)[0]):
    voltage[k] = np.fromstring(names[k][4:9],dtype = float, sep = '.')*voltagecali
    voltageerr[k] = voltage[k]*0.05
    cali = liste[k]
    cali[0,0] = 0
    calix = np.sum(cali,axis = 0)
    caliy = np.sum(cali,axis = 1)
    p0x = [np.amax(calix),np.shape(calix)[0]/2,np.shape(calix)[0]/5,0]
    p0y = [np.amax(caliy),np.shape(caliy)[0]/2,np.shape(caliy)[0]/5,0]
    popt, pcov = curve_fit(func, xaxis, calix,p0x)
    xc[k] = popt[1]
    xcerr[k] = np.sqrt(pcov[1,1])
    popt, pcov = curve_fit(func, yaxis, caliy,p0y)
    yc[k] = popt[1]
    ycerr[k] = np.sqrt(pcov[1,1])
    diffx[k] = xc[k]-xc[0]
    diffy[k] = yc[k]-yc[0]
    diffxerr[k] = np.sqrt(xcerr[k]**2 + xcerr[0]**2)
    diffyerr[k] = np.sqrt(ycerr[k]**2 + ycerr[0]**2)
    distance[k] = np.sqrt(diffx[k]**2 + diffy[k]**2)*ppmm
    distanceerr[k] = np.sqrt((diffy[k]*(diffx[k]**2+diffy[k]**2)**(-1/2))**2 \
    +(diffx[k]*(diffx[k]**2+diffy[k]**2)**(-1/2))**2)*ppmm
    angle[k] = np.arctan(distance[k]/realdistance)*10**3
    angleerr[k]=np.sqrt((distanceerr[k]/realdistance)**2+(distance[k]*realdistanceerr/realdistance**2)**2)*10**3

fig1 = plt.figure()
imshow(liste[0]) #shows the last picture

#same procedure for the negative values that are saved in a different folger
```

```
liste = []
names = []
os.chdir('A:\Dokumente\Daten␣Masterarbeit\markus\Data\DatenEOD\EOD_deflection_Aktuell/negative')
for file in glob.glob("*.csv"):
    liste.append(np.genfromtxt(file,delimiter=';',skip_header = 5, skip_footer = 1))
    names.append(file)
#adds the negative values of voltage to the already existing array of voltage
for k in range(0,np.shape(liste)[0]):
    voltage[k+numberoffiles] = np.fromstring(names[k][4:10],dtype = float, sep = '.')*voltagecali
    voltageerr[k+numberoffiles] = voltage[k+numberoffiles]*0.05
    cali = liste[k]
    cali[0,0] = 0
    calix = np.sum(cali,axis = 0)
    caliy = np.sum(cali,axis = 1)
    p0x = [np.amax(calix),np.shape(calix)[0]/2,np.shape(calix)[0]/5,0]
    p0y = [np.amax(caliy),np.shape(caliy)[0]/2,np.shape(caliy)[0]/5,0]
    popt, pcov = curve_fit(func, xaxis, calix,p0x)
    xc[k] = popt[1]
    xcerr[k] = np.sqrt(pcov[1,1])
    popt, pcov = curve_fit(func, yaxis, caliy,p0y)
    yc[k] = popt[1]
    ycerr[k] = np.sqrt(pcov[1,1])
    diffx[k] = xc[k]-xc[0]
    diffy[k] = yc[k]-yc[0]
    diffxerr[k] = np.sqrt(xcerr[k]**2 + xcerr[0]**2)
    diffyerr[k] = np.sqrt(ycerr[k]**2 + ycerr[0]**2)
    distance[k+numberoffiles] = np.sqrt(diffx[k]**2 + diffy[k]**2)*ppmm
    distanceerr[k+numberoffiles] = np.sqrt((diffy[k]*(diffx[k]**2 + diffy[k]**2)**(-1/2))**2 + \
    (diffx[k]*(diffx[k]**2 + diffy[k]**2)**(-1/2))**2)*ppmm
    angle[k+numberoffiles] = -np.arctan(distance[k+numberoffiles]/realdistance)*10**3
    angleerr[k+numberoffiles]=np.sqrt((distanceerr[k+numberoffiles]/realdistance)**2+\
    (distance[k+numberoffiles]*realdistanceerr/realdistance**2)**2)*10**3


#performs linear fit  and plots it
fig = plt.figure()
popt, pcov = curve_fit(lin, voltage, angle)
ym = lin(voltage, popt[0], popt[1])
plt.rc('font', weight='bold', size = 10.5)
ax = fig.add_subplot(111)
plt.rc('text', usetex=True)
ax.plot(voltage, ym, c='r', label= r'Linear␣Fit␣␣$\Theta=0.0025(1)\cdot␣U␣-␣0.3(2)$',linewidth=2)
plt.errorbar(voltage, angle, xerr=voltageerr, yerr=angleerr,fmt='o',
label = r'Deflection␣angle␣$\Theta$␣of␣the␣EOD')
plt.xlabel(r"Deflector␣voltage␣U␣(V)",size = 16)
plt.ylabel(r"Deflection␣angle␣$\Theta$␣(mrad)",size = 16)
plt.legend(bbox_to_anchor=(0.75, 0.99))
plt.xlim(-230, 230)
plt.ylim(-0.7,0.9)
plt.xticks(np.arange(-200,250,50),size = 15,weight = 'bold')
plt.yticks(size=15,weight='bold')
plt.savefig("deflectionpervolt", dpi = 500)
```

Appendix B

State preparation of the ion

B.1 Python code for the analysis of the effective phonon number

```
#Tool for fitting a rabiflop measured with 729 spectroscopy
import glob
import os
import numpy as np
from scipy.fftpack import fft, fftfreq
from pylab import imshow
from scipy.optimize import curve_fit
import matplotlib.pyplot as plt
from matplotlib import rc
rc('text', usetex=True)
def func(t, omega, n):
    eta = 0.0685
    a = np.cos(2*omega*t)+2*omega*t*eta**2*(n+1)*np.sin(2*omega*t)
    b = 1+(2*omega*t*eta**2*(n+1))**2
    c = 0.5*(1-a/b)
    return c   #function used from the Data analysis tool

data = np.loadtxt("2338.03.dat", skiprows = 1) #loads the .dat file

exc = np.zeros(np.shape(data)[0] + 1) #excitation
exc2 = np.zeros(np.shape(data)[0] + 1)
xaxis = np.zeros(np.shape(data)[0] + 1) #pulse length
qpn = np.zeros(np.shape(data)[0] + 1)#error = quantum projection noise
for i in range(np.shape(data)[0]): #calculates all this from the data
    xaxis[i+1] = data[i,0]
    exc[i+1] = data[i,1]
    qpn[i+1] = np.sqrt(exc[i+1]*(1-exc[i+1])/100) #formula taken from thomas monz thesis
#initial assumptions
p0 = (0.2,10)
#plot initial assumptions
fig3 = plt.figure()
plt.plot(xaxis,func(xaxis,*p0))
#perform fit
popt, pcov = curve_fit(func, xaxis, exc,p0)
dat = func(xaxis,popt[0],popt[1])

#settings for plotting
fig2 = plt.figure()
plt.rc('font', weight='bold', size = 10.5)
plt1 = plt.errorbar(xaxis,exc,yerr = qpn, fmt = 'o', label = r'Excitation')
plt4 = plt.plot(xaxis,dat, label = 'Fit:␣$\Omega_0␣=␣0.1570(3)\;\mathrm{MHz}\␣$␣\n␣␣$
␣␣␣n_{eff}␣=␣0.10(1)$␣␣', linewidth = 3)
plt.legend(bbox_to_anchor=(1, 0.3))
plt.xticks(np.arange(0,160,20),size = 15,weight = 'bold')
plt.yticks(np.arange(0,1.1,0.2),size = 15,weight = 'bold')
plt.ylabel('Excitation',size = 16)
plt.xlabel(r'Pulse␣length␣($␣\mu␣$s)',size = 16)
plt.savefig('Res:Doppler_cooling.png', dpi=1000)
```

Appendix C

Characterization of the single ion addressing beam

C.1 Python code for the calibration of the camera

```
import numpy as np
import scipy as sc
from PIL import Image
from matplotlib import pyplot as plt
from scipy.optimize import curve_fit
#open image as greyscale
im = Image.open("Abfree.png").convert('LA')
#plt.imshow(im)
#definiton of the multigaussian
def func(x, a1, x0, sigma,y0,a2, x02, sigma2,y02):
    return a1*np.exp(-(x-x0)**2/(2*sigma**2))+y0 + a2*np.exp(-(x-x02)**2/(2*sigma2**2))+y02

data = np.sum(im,axis = 1)[0:,0] #sum over the x axis
data[61] = data[60] #delete the cross that is just background at one pixel
xaxis = np.arange(0,np.shape(data)[0]) #generate xaxis for fit
xaxis = xaxis/10 #rescale the x axis
xaxis2 = np.arange(0,np.shape(data)[0],0.1) #generate xaxis for plot
xaxis2 = xaxis2/10

#fit the double gaussian
p0 = (7000,16,3,10,7000,25,3,10)
popt, pcov = curve_fit(func, xaxis, data,p0)


#settings for the plot
fig2 = plt.figure()
plt1 = plt.plot(xaxis,data, label= "Intensity (arb. units)",linewidth = 3)
plt4 = plt.plot(xaxis2,func(xaxis2,*popt), label =
'Fit $x_0 = 17.20(3) \ x_1 = 22.35(3) $', linewidth = 3)
plt.legend(bbox_to_anchor=(1.01, 1.01),prop={'size':9.5})
plt.ylabel('Intensity (arb. units)',size = 16,weight = 'bold')
plt.xlabel('Pixel',size = 16, weight = 'bold')
plt.xticks(size = 15,weight = 'bold')
plt.yticks(size=15,weight='bold')
plt.gcf().subplots_adjust(bottom=0.15)
plt.gcf().subplots_adjust(left=0.2)
plt.savefig('Camera_Calibration.png', dpi=1000)

#just print some things
print popt[1]-popt[5]
print np.sqrt(pcov[5,5]+pcov[1,1])
print popt[5]
print (np.sqrt(pcov[5,5]))
print popt[1]
print np.sqrt(pcov[1,1])

#calculation of the calibration of the ion ion distance in reality

M =6.6359437673083*10**(-26)
omega = 1.0027*10**6*2*np.pi
e = 1.6*10**(-19)
epsilon = 8.854*10**(-12)

a = 2.0
b = (e**2/(16*np.pi*epsilon*M*omega**2))**(0.333333)
dz = a * b
```

```
a = e**2/(4*np.pi*epsilon)
b = (2/(M*omega**2))
dz = (a * b)**(0.333333333333333333)
#print um/px
print dz/(popt[5]-popt[1])
```

C.2 Python code for the cross-talk measurement and the PMT-Camera comparison

```
#Tool for fitting a rabiflop measured with 729 spectroscopy
import glob
import os
import numpy as np
from scipy.fftpack import fft, fftfreq
from pylab import imshow
from scipy.optimize import curve_fit
import matplotlib.pyplot as plt
from matplotlib import rc
rc('text', usetex=True)
def func(t, omega, n):
    eta = 0.0685
    a = np.cos(2*omega*t)+2*omega*t*eta**2*(n+1)*np.sin(2*omega*t)
    b = 1+(2*omega*t*eta**2*(n+1))**2
    c = 0.5*(1-a/b)
    return c   #function used from the Data analysis tool


#function for calculating the overlap
def overlap( a, b):
    norm_a = np.sqrt(np.sum(a**2))
    norm_b = np.sqrt(np.sum(b**2))
    overlap_value =  np.sum(a*b) /(norm_b * norm_a)
    return overlap_value



data = np.loadtxt(r"C:\Users\troll\Desktop\Ordner␣SSD\␣\
Dokumente\Masterarbeit\Daten\1716_Crosstalk.dat", skiprows = 1)
print data
exc = np.zeros(np.shape(data)[0] + 1) #excitation
exc2 = np.zeros(np.shape(data)[0] + 1)
xaxis = np.zeros(np.shape(data)[0] + 1) #pulse length
qpn1 = np.zeros(np.shape(data)[0] + 1)
qpn2 = np.zeros(np.shape(data)[0] + 1)#error = quantum projection noise
for i in range(np.shape(data)[0]): #calculates all this from the data
    xaxis[i+1] = data[i,0]
    exc[i+1] = data[i,-2]
    exc2[i+1] = data[i,-1]
    qpn1[i+1] = np.sqrt(exc[i+1]*(1-exc[i+1])/100)
    qpn2[i+1] = np.sqrt(exc[i+1]*(1-exc[i+1])/100)#formula taken from thomas monz thesis
#exc = np.delete(exc,[15,16])
#exc2 = np.delete(exc2,[15,16])
xaxis2 = np.arange(0,np.max(xaxis),0.05)
#fitting and plotting
p0 = (1,20)
p02=(0.2,20)
popt, pcov = curve_fit(func, xaxis, exc2,p0)
popt2, pcov2 = curve_fit(func, xaxis, exc,p02)
dat = func(xaxis2,popt[0],popt[1])
dat2 = func(xaxis2,popt2[0],popt2[1])
fig2 = plt.figure()
plt1 = plt.errorbar(xaxis,exc, yerr = qpn1,fmt = 'o')
plt2 = plt.errorbar(xaxis,exc2,yerr = qpn2,fmt = 'o')
plt3 = plt.plot(xaxis2,dat2, label = r'Fit␣Ion␣1␣$\Omega␣=␣0.12(1)␣\mathrm{MHz}$
␣',linewidth = 3,color = 'b')
plt4 = plt.plot(xaxis2,dat, label = r'Fit␣Ion␣2␣$\Omega␣=␣1.766(8)␣\mathrm{MHz}$
␣',linewidth = 3,color = 'g')
plt.legend(bbox_to_anchor=(1, 0.22))
plt.ylabel('Excitation',size = 16)
plt.xlabel(r'Pulse␣length␣($␣\mu␣s␣$)',size = 16)
plt.xticks(size = 13)
plt.yticks(size=13)
plt.gcf().subplots_adjust(bottom=0.15)
plt.savefig('CrosstalkFinal.png', dpi=1000)



#PMT Camera comparison
data = np.loadtxt(r"C:\Users\troll\Desktop\Ordner␣SSD\Dokumente\Masterarbeit\Daten␣\
\1716_Crosstalk.dat", skiprows = 1)
camexc = np.loadtxt(r"C:\Users\troll\Desktop\Ordner␣SSD\Dokumente\Masterarbeit␣\
\Daten\camera_Crosstalk.dat")
xaxis = data[0:,0]
prob_individual_ion1 = data[0:,-2]
prob_individual_ion2 = data[0:,-1]
prob_individual_ion1_camera = np.zeros(np.shape(data)[0])
```

```
prob_individual_ion2_camera = np.zeros(np.shape(data)[0])

cycles = 100 #number of cycles
ss_cam = np.zeros(np.shape(camexc)[0])
sd_cam = np.zeros(np.shape(camexc)[0])
ds_cam = np.zeros(np.shape(camexc)[0])
dd_cam = np.zeros(np.shape(camexc)[0])

#count number of events of when ions are dark or bright from Camera
for j in range(np.shape(camexc)[0]):
    k = 0
    while k != np.shape(camexc)[1]:
        if camexc[j,k] == 1 and camexc[j,k+1] == 1:
            ss_cam[j] +=1
        if camexc[j,k] == 0 and camexc[j,k+1] == 0:
            dd_cam[j] +=1
        if camexc[j,k] == 0 and camexc[j,k+1] == 1:
            sd_cam[j] +=1
        if camexc[j,k] == 1 and camexc[j,k+1] == 0:
            ds_cam[j] +=1

        k = k+2

        #calculate excitation
ss_cam = ss_cam/float(cycles)
sd_cam = sd_cam/float(cycles)
ds_cam = ds_cam/float(cycles)
dd_cam = dd_cam/float(cycles)
prob_individual_SS = np.zeros(np.shape(data)[0])
prob_individual_SD = np.zeros(np.shape(data)[0])
prob_individual_DD =  np.zeros(np.shape(data)[0])
for i in range(np.shape(data)[0]):
    prob_individual_DD[i] = (np.count_nonzero(data[i,206:]==2))/float(cycles)
    prob_individual_SD[i] = (np.count_nonzero(data[i,206:]==1))/float(cycles)
    prob_individual_SS[i] = (np.count_nonzero(data[i,206:]==0))/float(cycles)

#calculate Quantum projection noise
qpn_ss_cam = np.sqrt(ss_cam*(1-ss_cam)/100)
qpn_sd_cam = np.sqrt((sd_cam+ds_cam)*(1-(sd_cam+ds_cam))/100)
qpn_dd_cam = np.sqrt(dd_cam*(1-dd_cam)/100)
qpn_ss_PMT = np.sqrt(prob_individual_SS*(1-prob_individual_SS)/100)
qpn_sd_PMT = np.sqrt((prob_individual_SD)*(1-(prob_individual_SD))/100)
qpn_dd_PMT = np.sqrt(prob_individual_DD*(1-prob_individual_DD)/100)

a= 2
#Plotting
figure = plt.figure()
plt1 = plt.plot(xaxis,prob_individual_SS,label  = 'SS␣PMT',linewidth = a)
plt2 = plt.plot(xaxis,prob_individual_SD, label  = 'SD+DS␣PMT',linewidth = a)
plt3 = plt.plot(xaxis,prob_individual_DD ,label  = 'DD␣PMT',linewidth =a)
plt4 = plt.plot(xaxis,ss_cam, label  = 'SS␣Camera',linewidth = a)
plt5 = plt.plot(xaxis,ds_cam + sd_cam , label = 'SD+DS␣Camera',linewidth =a)
plt6 = plt.plot(xaxis,dd_cam, label = 'DD␣Camera',linewidth = a )
plt.legend(bbox_to_anchor=(1, 1),prop={'size':8.3})
plt.ylabel('Excitation',size = 16)
plt.xlabel(r'Pulse␣length␣($␣\mu␣s␣$)',size = 16)
plt.xticks(size = 13)
plt.yticks(size=13)
plt.gcf().subplots_adjust(bottom=0.15)
plt.savefig('Camera_PMT_Comparison_Crosstalk.png', dpi=1000)

#calculate the overlap
print 'Overlap␣SS'
print overlap(ss_cam,prob_individual_SS)
print 'Overlap␣DD'
print overlap(dd_cam,prob_individual_DD)
print 'Overlap␣SDDS'
print overlap(sd_cam+ds_cam,prob_individual_SD)
```

Bibliography

[1] P. Markus. Quantum cryptography to protect swiss election. *https://www.newscientist.com/article/dn12786-quantum-cryptography-to-protect-swiss-election/*, 2007.

[2] P. W. Shor. Polynomial-time algorithms for prime factorization and discrete logarithms on a quantum computer. *SIAM J. Comput.*, 26(5):1484–1509, October 1997.

[3] D. P. DiVincenzo. The physical implementation of quantum computation. *Fortschritte der Physik*, 48(9-11):771–783, 2000.

[4] H. Häffner, C. F. Roos, and R. Blatt. Quantum computing with trapped ions. *Physics Reports*, 469(4):155 – 203, 2008.

[5] S. Barz. Quantum computing with photons: introduction to the circuit model, the one-way quantum computer, and the fundamental principles of photonic experiments. *Journal of Physics B: Atomic, Molecular and Optical Physics*, 48(8):083001, 2015.

[6] M. H. Devoret and R. J. Schoelkopf. Superconducting circuits for quantum information: An outlook. *Science*, 339(6124):1169–1174, 2013.

[7] L.-M. Duan and C. Monroe. Colloquium. *Rev. Mod. Phys.*, 82:1209–1224, Apr 2010.

[8] H.-J. Briegel, W. Dür, J. I. Cirac, and P. Zoller. Quantum repeaters: The role of imperfect local operations in quantum communication. *Phys. Rev. Lett.*, 81:5932–5935, Dec 1998.

[9] M. Zwerger, B. P. Lanyon, T. E. Northup, C. A. Muschik, W. Dür, and N. Sanguard. Quantum repeaters based on trapped ions with decoherence free subspace encoding. *arXiv:1611.07779*.

[10] T. E. Northup and R. Blatt. Quantum information transfer using photons. *Nat. Photon.*, 8(5):356–363, May 2014.

[11] A. Stute, B. Casabone, B. Brandstatter, K. Friebe, T. E. Northup, and R. Blatt. Quantum-state transfer from an ion to a photon. *Nat. Photon.*, 7(3):219–222, Mar 2013.

[12] A. Stute, B. Casabone, P. Schindler, T. Monz, P. O. Schmidt, B. Brandstatter, T. E. Northup, and R. Blatt. Tunable ion-photon entanglement in an optical cavity. *Nature*, 485(7399):482–485, May 2012.

[13] B. Casabone, A. Stute, K. Friebe, B. Brandstätter, K. Schüppert, R. Blatt, and T. E. Northup. Heralded entanglement of two ions in an optical cavity. *Phys. Rev. Lett.*, 111:100505, Sep 2013.

[14] Sebastian Zaske, Andreas Lenhard, Christian A. Keßler, Jan Kettler, Christian Hepp, Carsten Arend, Roland Albrecht, Wolfgang-Michael Schulz, Michael Jetter, Peter Michler, and Christoph Becher. Visible-to-telecom quantum frequency conversion of light from a single quantum emitter. *Phys. Rev. Lett.*, 109:147404, Oct 2012.

[15] L. Aolita, L. Davidovich, K. Kim, and H. Häffner. Universal quantum computation in decoherence-free subspaces with hot trapped ions. *Phys. Rev. A*, 75:052337, May 2007.

[16] D. Habicher. Abbildung, Adressierung und Zustandsdetektion zweier Ionen in einem optischen resonator. Master's thesis, University of Innsbruck, 2011.

[17] H. C. Nägerl, D. Leibfried, H. Rohde, G. Thalhammer, J. Eschner, F. Schmidt-Kaler, and R. Blatt. Laser addressing of individual ions in a linear ion trap. *Phys. Rev. A*, 60:145–148, Jul 1999.

[18] C. F. Roos. *Controlling the quantum state of trapped ions*. PhD thesis, University of Innsbruck, 2000.

[19] B. Casabone. *Two ions coupled to an optical cavity: from an enhanced quantum computer interface towards distributed quantum computing*. PhD thesis, University of Innsbruck, 2015.

[20] C. J. Foot. *Atomic physics*. Oxford master series in physics, New York, third edition, 02 2005. Pg. 123-154.

[21] Jürgen Eschner, G. Morigi, F. Schmidt-Kaler, and R. Blatt. Laser cooling of trapped ions. *J. Opt. Soc. Am. B*, 20(5):1003–1015, May 2003.

[22] J. I. Cirac and P. Zoller. Quantum computations with cold trapped ions. *Phys. Rev. Lett.*, 74:4091–4094, May 1995.

[23] A. Sørensen and K. Mølmer. Entanglement and quantum computation with ions in thermal motion. *Phys. Rev. A*, 62:022311, Jul 2000.

[24] C. Monroe, D. M. Meekhof, B. E. King, S. R. Jefferts, W. M. Itano, D. J. Wineland, and P. Gould. Resolved-sideband raman cooling of a bound atom to the 3d zero-point energy. *Phys. Rev. Lett.*, 75:4011–4014, Nov 1995.

[25] G. Morigi, J. I. Cirac, M. Lewenstein, and P. Zoller. Ground-state laser cooling beyond the Lamb-Dicke limit. *EPL (Europhysics Letters)*, 39(1):13, 1997.

[26] C. Lechner, R.and Maier, C. Hempel, P. Jurcevic, B.P. Lanyon, T. Monz, M. Brownnutt, R. Blatt, and C. F. Roos. Electromagnetically-induced-transparency ground-state cooling of long ion strings. *Phys. Rev. A*, 93:053401, May 2016.

[27] D. F. V. James. Quantum dynamics of cold trapped ions with application to quantum computation. *Applied Physics B*, 66(2):181–190, 1998.

[28] H.C. Nägerl, W. Bechter, J. Eschner, F. Schmidt-Kaler, and R. Blatt. Ion strings for quantum gates. *Applied Physics B*, 66(5):603–608, 1998.

[29] T. Ramm, M.and Pruttivarasin, M. Kokish, I. Talukdar, and H. Häffner. Precision measurement method for branching fractions of excited $P_{1/2}$ states applied to $^{40}\mathrm{Ca}^{+}$. *Phys. Rev. Lett.*, 111:023004, Jul 2013.

[30] R. Gerritsma, G. Kirchmair, F. Zähringer, J. Benhelm, R. Blatt, and C. F. Roos. Precision measurement of the branching fractions of the 4p3/2 decay of ca ii. *The European Physical Journal D*, 50(1):13–19, 2008.

[31] A. Galindo and P. Pascual. *Quantum Mechanics*. Springer-Verlag, Heidelberg, second edition, 1991. Pg. 189-217.

[32] D. J. Wineland, C. Monroe, W. M. Itano, D. Leibfried, B. E. King, and D. M. Meekhof. Experimental issues in coherent quantum-state manipulation of trapped atomic ions. *J Res Natl Inst Stand Technol*, 103(3):259–328, Jun 1998.

[33] Wolfgang Paul. Electromagnetic traps for charged and neutral particles. *Rev. Mod. Phys.*, 62:531–540, Jul 1990.

[34] L.S. Brown and G. Gabrielse. Geonium theory: Physics of a single electron or ion in a penning trap. *Reviews of Modern Physics*, Vol. 58(1):233–310, 1986.

[35] C. Russo. *Photon statistics of a single ion coupled to a high-finesse cavity*. PhD thesis, University of Innsbruck, 2008.

[36] A.Stute. *A light-matter quantum interface: ion-photon entanglement and state mapping*. PhD thesis, University of Innsbruck, 2012.

[37] H. Barros. *Raman spectroscopy and single-photon source in an ion-cavity system*. PhD thesis, University of Innsbruck, 2010.

[38] D. Rotter. Photoionisation von Kalzium. Master's thesis, Unversity of Innsbruck, 2003.

[39] M. Chwalla. *Precision spectroscopy with $^{40}Ca^{+}$ ions in a Paul trap*. PhD thesis, University of Innsbruck, 2009.

[40] E. D. Black. An introduction to pound-drever-hall laser frequency stabilization. *American Journal of Physics*, 69(1):79–87, 2001.

[41] R. Lerchner. *Multi-mode cooling techniques for trapped ions*. PhD thesis, University of Innsbruck, 2016.

[42] R. Stricker. Gatteroperationen hoher Güte in einem optischen Quantenbit. Master's thesis, University of Innsbruck, 2017.

[43] Y. Pang, J. J. Hamilton, and J.-P. Richard. Frequency noise induced by fiber perturbations in a fiber-linked stabilized laser. *Appl. Opt.*, 31(36):7532–7534, Dec 1992.

[44] B. E. A. Saleh and M. C. Teich. *Electro-Optics*. John Wiley & Sons, Inc., New York, first edition, 2001. Pg. 696-736.

[45] J. Benhelm. *Precision spectroscopy and quantum information processing with trapped calcium ions*. PhD thesis, University of Innsbruck, 2008.

[46] T. Monz. *Quantum information processing beyond ten ion-qubits*. PhD thesis, University of Innsbruck, 2011.

[47] P. Schindler. Frequency synthesis and pulse shaping for quantum information processing with trapped ions. Master's thesis, University of Innsbruck, 2008.

[48] C. Cohen-Tannoudji, J. Dupont-Roc, and G. Grynberg. *Quantum Electrodynamics in the Coulomb Gauge*, volume 1. Wiley-VCH Verlag GmbH, New York, first edition, 2007. Pg. 187-210.

[49] H. P. Specht, C. Nolleke, A. Reiserer, M. Uphoff, E. Figueroa, S. Ritter, and G. Rempe. A single-atom quantum memory. *Nature*, 473(7346):190–193, May 2011.

[50] F. Schmidt-Kaler, S. Gulde, M. Riebe, T. Deuschle, A. Kreuter, G. Lancaster, C. Becher, J. Eschner, H. Häffner, and R. Blatt. The coherence of qubits based on single Ca^+ ions. *Journal of Physics B: Atomic, Molecular and Optical Physics*, 36(3):623, 2003.

[51] N. F. Ramsey. Experiments with separated oscillatory fields and hydrogen masers. *Rev. Mod. Phys.*, 62:541–552, Jul 1990.

[52] Daniel Nigg. *Towards fault tolerant quantum computation*. PhD thesis, University of Innsbruck, 2017.

[53] R. Loudon. *The quantum theory of light*. Oxford University Press, New York, first edition, 1983. Pg. 14.

[54] C. Hempel. *Digital quantum simulation, Schrödinger cat state spectroscopy and setting up a linear ion trap*. PhD thesis, University of Innsbruck, 2014.

[55] W. Köhler, G. Schachtel, and P.Voleske. *Biostatistik*. Springer, Berlin, fourth edition, 04 2007. Pg. 47-53.

[56] Horst Rinne. *Taschenbuch der Statistik*. Harri Deutsch, Haan, third edition, 2003. Pg.560-564.

[57] H. Häffner, S. Gulde, M. Riebe, G. Lancaster, C. Becher, J. Eschner, F. Schmidt-Kaler, and R. Blatt. Precision measurement and compensation of optical stark shifts for an ion-trap quantum processor. *Phys. Rev. Lett.*, 90:143602, Apr 2003.